

Intracellular delivery and voltage sensitivity of nanomaterials
for the optical imaging of neuronal activity

by

Mengke Han



THE UNIVERSITY
of ADELAIDE

A thesis submitted for the degree of Doctor of Philosophy

in the

Faculty of Sciences

School of Physical Sciences

The University of Adelaide

February 2022

“The law of contradiction in things, that is, the law of the unity of opposites, is the fundamental law of nature and of society and therefore also the fundamental law of thought. It stands opposed to the metaphysical world outlook. It represents a great revolution in the history of human knowledge. According to dialectical materialism, contradiction is present in all processes of objectively existing things and of subjective thought and permeates all these processes from beginning to end; this is the universality and absoluteness of contradiction. Each contradiction and each of its aspects have their respective characteristics; this is the particularity and relativity of contradiction. In given conditions, opposites possess identity, and consequently can coexist in a single entity and can transform themselves into each other; this again is the particularity and relativity of contradiction. But the struggle of opposites is ceaseless, it goes on both when the opposites are coexisting and when they are transforming themselves into each other, and becomes especially conspicuous when they are transforming themselves into one another; this again is the universality and absoluteness of contradiction.”

– **Mao Zedong**

Abstract

Monitoring the electrical signals generated by neurons to transmit information, is central to understanding how the brain and nervous systems work. The photoluminescence (PL) of some nanomaterials, such as semiconductor quantum dots (QDs) and fluorescent nanodiamonds (NDs), has shown higher sensitivity to electrical fields than that of any previously reported probes, which may address the persistent challenge of robust optical voltage imaging. The fundamental issue for implementing voltage-sensitive nanomaterials (VSM) in live neurons is their delivery into the plasma membrane bilayer. Currently, the delivery has been demonstrated on QDs via their spontaneous insertion directly into the plasma membrane bilayer, or indirectly into the bilayer of liposomes that later fuse with the plasma membrane. In both methods, QDs are introduced from the extracellular space and implemented to image the activity of neuronal assemblies.

The first part of this thesis explores the implementation of VSM in another scenario, i.e., the voltage imaging from multiple sites on single neurons. After direct intracellular delivery, amphiphilic nanomaterials are expected to spread into distal processes and insert into the plasma membrane bilayer, being able to monitor the electrical activity in the smallest neuronal structures, such as dendritic spines. Here, the intracellular delivery of nontargeted QDs as an example, has been demonstrated by microelectrophoresis technique, where electrical currents were applied to eject charged QDs through fine-tipped glass micropipettes into living cells. The amount of delivered QDs was finely controlled by tuning the ejection duration, which had a substantial impact on preserving short-term and long-term cell health. Delivered QDs were homogeneously distributed throughout the cytoplasm and presented pure Brownian diffusion without endosomal entrapment. These original and promising results lay the foundation to apply the microelectrophoresis technique to other VSM, including the protocol for preparing nanomaterials suspension and the required tip sizes of micropipettes, which are key to their successful intracellular loading.

Another fundamental issue is ascertaining the PL responses of these nanomaterials to applied voltage modulations. The second part of this thesis describes the fabrication of a multilayer device that can apply a homogeneous electric field to the embedded nanomaterials (NDs as an example). By using ultrasonication, NDs were well dispersed as single particles within the device, where the PL responses of individual NDs can be examined. Other fabrication details, such as film thickness and electrode deposition, were also described. These results provide a high-throughput screening platform to characterize the voltage sensitivities of different nanomaterials, which helps to iteratively improve their design and synthesis, including composition, size, shape, and band alignment.

Collectively, the findings in this thesis provide a significant contribution to the unique interface of neuroscience and nanomaterials regarding the optical visualization of neuronal activity. The pioneering work here facilitates the future use of microelectrophoresis technique to deliver various VSM for multisite voltage imaging of single neurons. The deployment of the multilayer device promotes the development and optimization of new nanomaterials with enhanced voltage sensitivity. With these fundamental challenges to be addressed in the near future, real-time in vivo voltage imaging may be attainable in relevant animal models to elucidate the complex function of brain and nervous systems.

Declaration

I certify that this work contains no material which has been accepted for the award of any other degree or diploma in my name, in any university or other tertiary institution and, to the best of my knowledge and belief, contains no material previously published or written by another person, except where due reference has been made in the text. In addition, I certify that no part of this work will, in the future, be used in a submission in my name, for any other degree or diploma in any university or other tertiary institution without the prior approval of the University of Adelaide and where applicable, any partner institution responsible for the joint award of this degree.

I acknowledge that copyright of published works contained within this thesis resides with the copyright holder(s) of those works.

I also give permission for the digital version of my thesis to be made available on the web, via the University's digital research repository, the Library Search and also through web search engines, unless permission has been granted by the University to restrict access for a period of time.

Mengke Han

18 February 2022

Acknowledgements

I wish to thank my supervisors, Heike Ebendorff-Heidepriem, Steven Wiederman, and Sanam Mustafa, for their guidance and contributions in the past four years. They have been helping me in all aspects of my candidature, as friends and as role models.

In addition, I would like to thank the members and collaborators in IPAS, Adelaide Medical School, Adelaide Microscopy, ANFF-SA and RMIT, for their help throughout this project: Xuanzhao Pan, Yunle Wei, Lu Peng, Lijesh Thomas, Alson Ng, Joseph Fabian, Samuel Evans, Josh Woenig, Jane Sibbons, Ken Neubauer, Jing-Hong Pai, Philipp Reineck and Roy Styles. Thank you together for making this journey enjoyable and exciting.

Finally, I would like to thank my family for their love and support over these years. Mum, dad, Hongwei and many others.

Author's comments

This thesis is presented in the format of thesis by combination. This means that the results presented include a combination of published articles and traditional results chapters. Publications within this thesis are in the exact form of the original articles as published and in text references to figures are as they were in the published manuscript.

Publications

Thesis related publications

P1. **Mengke Han**, Jiangbo Zhao, Joseph Mahandas Fabian, Samuel Evans, Sanam Mustafa, Yinlan Ruan, Steven Wiederman, and Heike Ebendorff-Heidepriem. *Cytoplasmic delivery of quantum dots via microelectrophoresis technique*. Electrophoresis, 2021.

P2. **Mengke Han**, Samuel Evans, Sanam Mustafa, Steven Wiederman, and Heike Ebendorff-Heidepriem. *Controlled delivery of quantum dots using microelectrophoresis technique: Intracellular behavior and preservation of cell viability*. Bioelectrochemistry, 2022.

P3. **Mengke Han**, Sanam Mustafa, Yinlan Ruan, Steven Wiederman, Jiangbo Zhao, Heike Ebendorff-Heidepriem, and Joseph Fabian. *Intracellular delivery of nanoparticles via microelectrophoresis technique*. Proceedings SPIE, 2019. (Conference presentation)

Publication not within scope of thesis

P4. Lu Peng, Nicolas Riesen, Jiawen Li, **Mengke Han**, Linh Viet Nguyen, Heike Ebendorff-Heidepriem, and Stephen C. Warren-Smith. *Whispering gallery mode excitation using exposed-core fiber*. Optics Express, 2021.

Acronyms

(In alphabetical order)

2-DHG	Two-dimensional hole gas
AFM	Atomic force microscope
BSTMD	Binocular small target motion detector
DIC	Differential interference contrast
DLS	Dynamic light scattering
DMEM	Dulbecco's modified Eagle's media
DNA	Deoxyribonucleic acid
DND	Detonation nanodiamond
FBS	Fetal bovine serum
HEK	Human embryonic kidney
HPHT	High-pressure high-temperature
ID	Inner diameter
ITO	Indium tin oxide
MSD	Mean square displacement
ND	Nanodiamond
NEAA	Non-essential amino acid
NP	Nanoparticle
NR	Nanorod
NV	Nitrogen vacancy

OD	Outer diameter
PBS	Phosphate-buffered saline
PEG	Polyethylene glycol
PL	Photoluminescence
PMMA	Poly (methyl methacrylate)
PVP	Polyvinylpyrrolidone
PVP	Poly (vinylpyrrolidone)
QCSE	Quantum-confined Stark effect
QD	Quantum Dot
SD	Standard deviation
SEM	Scanning electron microscope
SHG	Second harmonic generation
TEM	Transmission electron microscope
VSD	Voltage-sensitive dye
VSM	Voltage-sensitive nanomaterials
WANDA	Automated nanomaterials discovery and analysis
ZPL	Zero-phonon line

Thesis layout

Since Galvani discovered and proclaimed that electricity is the true agent of nervous action in the late 18th century,¹ immense effort has been invested into measuring this electrical activity to understand how the brain and the nervous system work.² By using metal or glass electrodes to directly record these signals, electrophysiology offers high fidelity but requires direct physical contact with the nervous tissue.³ Therefore, it is difficult to approach subcellular structures, and tissue damage caused by electrode arrays is inevitable in the studies of neuronal assemblies.⁴ Optical reporters, such as voltage-sensitive dyes (VSDs),⁵⁻¹⁰ calcium indicators,^{11, 12} and genetically encoded voltage-sensitive proteins,¹³⁻¹⁵ that convert electrical activity or consequent effects into optical signals, have been used extensively as complementary to electrophysiology to avoid physical contact, where electrical activity in the smallest neuronal structures or in large-scale neuronal assemblies can be monitored simultaneously.^{16, 17} Yet these reporters suffer from low brightness, high photobleaching, and phototoxicity, which strongly constrain the excitation intensity and experiment duration.³ VSM, such as QDs and NDs, with excellent brightness, photostability, and biocompatibility rendered from surface modification, could potentially overcome the most challenging problem at the core of neuroscience, namely the robust optical visualization of neuronal activity.^{18, 19}

In the first part of this thesis, the advantages of using VSM for the optical imaging of neuronal activity will be described. The fundamental issues of the delivery, targeting, and positioning of VSM will be discussed. Together, the background information introduces the central focus of Part I, that is, the intracellular delivery of nanomaterials using microelectrophoresis technique.

In addition to the intracellular delivery and membrane insertion challenges, improving the voltage sensitivity of nanomaterials, i.e., the fractional fluorescence change in response to a unit change in membrane potential, represents another frontier that would otherwise require elaborate signal corrections and substantial temporal averaging to achieve high signal-to-noise ratio (S/N). A high throughput screening platform to apply neuronal-like voltage modulation can effectively serve to search for the best candidate within large libraries of engineered nanomaterials having

various compositions and structures. More importantly, the screening platform helps to determine and understand the source of their voltage sensitivity, contributing to the accurate translation of optical signals into potential changes and the rational design of voltage nanosensors in future. The screening needs to be addressed in vitro before the attempt to implement these nanosensors in the complex cellular environment. The applied voltage modulation should be scaled on the order of membrane potential changes, i.e., an enormous electric field of $10^7 - 10^8$ V/m at kHz frequencies, and nanomaterials should be embedded within a very narrow section of dielectric material that mimics the plasma membrane.²⁰

In the second part of this thesis, the physical origin of the voltage sensitivity of QDs and NDs will be introduced. Several in vitro devices designed for characterizing the fluorescence responses of QDs and NDs to an externally applied electrical fields will be described. Their pros and cons together point towards the research focus of Part II, that is, to study the voltage sensitivity of single ND in solid state using a high throughput screening platform.

References

1. Galvani, L., De Viribus Electricitatis in Motu Musculari. Commentarius. *De Bonoiensium Scientiarum et Artium Intituo atque Academie Commentarii* **1791**, 7, 363-418.
2. Verkhratsky, A.; Krishtal, O. A.; Petersen, O. H., From Galvani to Patch Clamp: The Development of Electrophysiology. *Pflügers Archiv* **2006**, 453 (3), 233-247.
3. Scanziani, M.; Häusser, M., Electrophysiology in the Age of Light. *Nature* **2009**, 461 (7266), 930-939.
4. Buzsáki, G., Large-Scale Recording of Neuronal Ensembles. *Nature Neuroscience* **2004**, 7 (5), 446-451.
5. Loew, L. M., Design and Use of Organic Voltage Sensitive Dyes. In *Membrane Potential Imaging in the Nervous System and Heart*, Canepari, M.; Zecevic, D.; Bernus, O., Eds. Springer International Publishing: Cham, **2015**; pp 27-53.

6. Tsytsarev, V.; Liao, L. D.; Kong, K. V.; Liu, Y. H.; Erzurumlu, R. S.; Olivo, M.; Thakor, N. V., Recent Progress in Voltage-Sensitive Dye Imaging for Neuroscience. *J Nanosci Nanotechnol* **2014**, *14* (7), 4733-44.
7. Grinvald, A.; Hildesheim, R., VSDI: A New Era in Functional Imaging of Cortical Dynamics. *Nature Reviews Neuroscience* **2004**, *5* (11), 874-885.
8. Jin, W.; Zhang, R.-J.; Wu, J.-y., Voltage-Sensitive Dye Imaging of Population Neuronal Activity in Cortical Tissue. *Journal of Neuroscience Methods* **2002**, *115* (1), 13-27.
9. Bullen, A.; Saggau, P., High-Speed, Random-Access Fluorescence Microscopy: II. Fast Quantitative Measurements with Voltage-Sensitive Dyes. *Biophysical Journal* **1999**, *76* (4), 2272-2287.
10. Miller, E. W., Small Molecule Fluorescent Voltage Indicators for Studying Membrane Potential. *Current opinion in chemical biology* **2016**, *33*, 74-80.
11. Tian, L.; Hires, S. A.; Mao, T.; Huber, D.; Chiappe, M. E.; Chalasani, S. H.; Petreanu, L.; Akerboom, J.; McKinney, S. A.; Schreier, E. R.; Bargmann, C. I.; Jayaraman, V.; Svoboda, K.; Looger, L. L., Imaging Neural Activity in Worms, Flies and Mice with Improved Gcamp Calcium Indicators. *Nature Methods* **2009**, *6* (12), 875-881.
12. Dombek, D. A.; Khabbaz, A. N.; Collman, F.; Adelman, T. L.; Tank, D. W., Imaging Large-Scale Neural Activity with Cellular Resolution in Awake, Mobile Mice. *Neuron* **2007**, *56* (1), 43-57.
13. Siegel, M. S.; Isacoff, E. Y., A Genetically Encoded Optical Probe of Membrane Voltage. *Neuron* **1997**, *19* (4), 735-741.
14. Blunck, R.; Chanda, B.; Bezanilla, F., Nano to Micro — Fluorescence Measurements of Electric Fields in Molecules and Genetically Specified Neurons. *The Journal of Membrane Biology* **2005**, *208* (2), 91-102.

15. Baker, B. J.; Mutoh, H.; Dimitrov, D.; Akemann, W.; Perron, A.; Iwamoto, Y.; Jin, L.; Cohen, L. B.; Isacoff, E. Y.; Pieribone, V. A.; Hughes, T.; Knöpfel, T., Genetically Encoded Fluorescent Sensors of Membrane Potential. *Brain Cell Biology* **2008**, *36* (1), 53.
16. Wilt, B. A.; Burns, L. D.; Wei Ho, E. T.; Ghosh, K. K.; Mukamel, E. A.; Schnitzer, M. J., Advances in Light Microscopy for Neuroscience. *Annual review of neuroscience* **2009**, *32*, 435-506.
17. Grewe, B. F.; Helmchen, F., Optical Probing of Neuronal Ensemble Activity. *Current Opinion in Neurobiology* **2009**, *19* (5), 520-529.
18. Efros, A. L.; Delehanty, J. B.; Huston, A. L.; Medintz, I. L.; Barbic, M.; Harris, T. D., Evaluating the Potential of Using Quantum Dots for Monitoring Electrical Signals in Neurons. *Nature nanotechnology* **2018**, *13* (4), 278-288.
19. Karaveli, S.; Gaathon, O.; Wolcott, A.; Sakakibara, R.; Shemesh, O. A.; Peterka, D. S.; Boyden, E. S.; Owen, J. S.; Yuste, R.; Englund, D., Modulation of Nitrogen Vacancy Charge State and Fluorescence in Nanodiamonds Using Electrochemical Potential. *Proc Natl Acad Sci U S A* **2016**, *113* (15), 3938-43.
20. Peterka, D. S.; Takahashi, H.; Yuste, R., Imaging Voltage in Neurons. *Neuron* **2011**, *69* (1), 9-21.

Part I Intracellular delivery of nanomaterials via microelectrophoresis technique

CONTENTS

Chapter 1	Introduction.....	18
Chapter 2	Intracellular delivery of quantum dots via microelectrophoresis technique.....	51
Chapter 3	Intracellular fate of microelectrophoretic delivered quantum dots.....	67
Chapter 4	Conclusions.....	89

CHAPTER 1 INTRODUCTION

CONTENTS

1.1	Measuring electrical signals in neurons	19
1.1.1	Membrane potential changes.....	19
1.1.2	Electrophysiology techniques	19
1.2	Optical imaging of neuronal activity.....	23
1.2.1	Optical reporters.....	23
1.2.2	Imaging neuronal activity with voltage-sensitive dyes.....	25
1.3	Voltage-sensitive nanomaterials	29
1.3.1	Quantum dots	30
1.3.2	Extracellular delivery of quantum dots for voltage imaging	32
1.4	Microelectrophoretic delivery of nanomaterials	34
1.4.1	Summary of methods for monitoring neuronal activity.....	34
1.4.2	Advantages of microelectrophoresis technique	35
1.5	Part I aims and scope.....	36
1.6	References	38

1.1 Measuring electrical signals in neurons

As the basic structural and functional unit of nervous systems, neurons perform the especially complex functions of the brain, i.e., acquiring, coordinating, and disseminating information about the body and its environment, by generating sophisticated electrical signals. This section briefly describes these signals and how they are produced. Then this section discusses the strengths and weaknesses of electrophysiology techniques. Finally, these fundamentals point towards the need for developing optical imaging techniques to monitor neuronal activity.

1.1.1 Membrane potential changes

Neurons have evolved elaborate mechanisms for generating electrical signals based on the flow of ions across their plasma membranes.¹ In the unstimulated state, neurons maintain a resting membrane potential, ranging from about -65 mV to -90 mV, which is caused by a net efflux of potassium ions down their concentration gradient.² When the dendrites receive suprathreshold stimuli (e.g., synaptic inputs), a transient rise in sodium ions permeability allows a net influx of sodium ions against their concentration gradient across the membrane and changes the negative resting membrane potential to positive, namely the overshoot phase (Figure 1).³ The brief rise in membrane sodium permeability is followed by a secondary, transient rise in membrane potassium permeability that repolarizes the membrane potential and produces a brief undershoot phase. When these permeabilities changes subside, the membrane potential returns to its resting level because of the high resting membrane permeability to potassium.¹ The process is repeated, generating action potentials that propagate along the axon and convey information over substantial distances from one place to another in the nervous systems. The ends of an axon are swollen terminals that form the presynaptic components of synaptic contacts to transmit signals to other cells.

1.1.2 Electrophysiology techniques

Being able to accurately record the electrical signals generated by neurons is fundamental for our understanding of the brain and nervous systems. Electrophysiology has long been the dominant

method in the field. By using metal, glass or silicon electrodes to directly record these electrical signals, electrophysiological tools allow us to study the properties of single ion channels (patch-clamp recording), the activity of single neurons (intracellular recording), and more complex activity of neuronal assemblies (extracellular recording), with superior sensitivity and temporal resolution.⁴ However, electrophysiology requires direct physical contact with the nervous tissue to be investigated. This main weakness largely limits its application in two aspects: (1) multisite recordings of a single neuron; (2) simultaneous recordings of neuronal assemblies.

- Multisite recordings of a single neuron

Different types of electrical signals, usually from multiple sources, are integrated by single neurons during the processing of information.^{5,6} Regional electrical events in branching dendrites and thin axons, which determine the input-output function of individual neurons, are extraordinarily complex and dynamic. To understand the signal integration performed in a single neuron, multisite recordings are required to monitor these electrical events when they travel from the sites of origin and summate to influence the initiation of action potentials.^{7,8} The experimental advance in multiple electrode recordings have made simultaneous monitoring of voltage transients

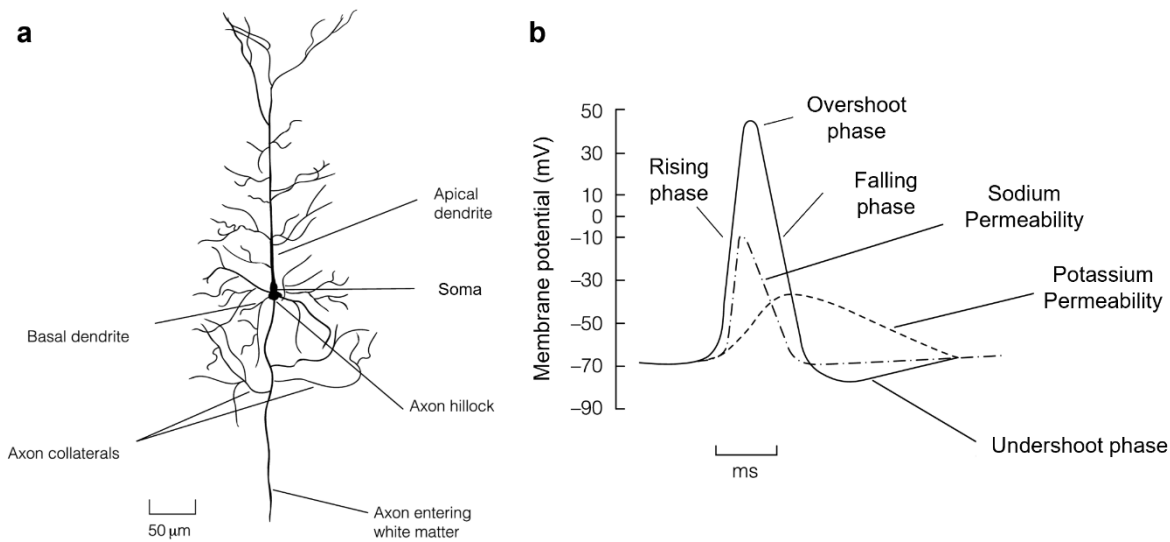


Figure 1 (a) Schematic illustration of the key structural features of a pyramidal neuron showing the distribution of dendrites and axon. The axon runs on much farther than shown. (b) The phases and changes in ion permeability during the action potential. Reproduced from reference 3.

from two or more locations on a single neuron possible, underscoring the importance of such measurements.

For example, the dendrites of some central neurons are highly elaborate and covered with hundreds of tiny projections termed dendritic spines, where synaptic contacts, the sites of neuron-to-neuron communication, are located. It has been asserted that dendrites simply act like electrical filters, where the amplitude of synaptic potentials reduces as they travel from their sites of origin to the soma.⁹ This means that synapses close to the soma and axon will powerfully influence the generation of action potentials, whereas synapses located on remote dendrites will have a tapering impact.⁹ However, simultaneous electrical recordings from the dendrites and soma of central neurons revealed that dendrites are electrically excitable as important sites for synaptic integration (Figure 2a).¹⁰ Synaptic inputs with specific temporal features are integrated locally in the apical dendrites, leading to the generation of dendritic spikes that actively propagate from their site of generation to the soma and powerfully drive the action potential output on the axon (Figure 2b).¹⁰ In this view of synaptic integration, the neuronal output is not only determined by the synaptic input that directly reaches the axonal site of action potential generation but is also powerfully influenced by the forward propagation of dendritic spikes.¹⁰⁻¹³ These findings uncover the enormous computational flexibility of neurons to integrate thousands of synaptic inputs that they receive.

However, limited by the invasive character of electrodes, direct electrical recordings are prevented from monitoring more complex spatiotemporal patterns of signal initiation and propagation in single neurons, where subcellular structures, including small diameter dendritic branches and spines, and most axon collaterals and terminals, are not accessible to electrodes.

- Simultaneous recordings of neuronal assemblies

The complex cognitive and behavioral capabilities of brain are produced by fluctuating patterns of electrical and chemical activities that coherently occur within neuronal assemblies.^{7, 14} The ability to simultaneously monitor the activity and interaction of large numbers of neurons in multiple brain regions, is important to the comprehensive understanding of brain function.^{1, 15}

During an action potential, the voltage transients across the membrane generate local, temporary differences in potential on the outer surface of the neuron.^{4, 16} Therefore, action potentials can be detected in the extracellular space by placing the recording electrode near the membrane of active neurons.^{4, 17} By using an electrode array, the activity of multiple neurons can be recorded at the same time (Figure 2c).¹⁸ Generally, the number of electrodes in an array can vary from four (tetrode) to over 100.¹⁹⁻²²

However, electrical recordings of large numbers of neurons by highly invasive electrode arrays inevitably increase tissue damage, which raises the concern how trustworthy the measured signals are.²³ The neurons may be damaged by the blunt end of the closely placed electrodes, resulting in a weak or no signal.²⁴ Thus, there is a large gap between the numbers of practically recorded and theoretically recordable neurons.²³ Moreover, if there are many active neurons in the vicinity of the electrode, it listens to all of them (Figure 2d).¹⁸ The enormous amount of data lead to the challenge of identifying individual neurons from their superimposed activities and extracting the spikes corresponding to different neurons, i.e., the spike sorting problem.²⁵⁻²⁷ In practice, only a small fraction of the neurons can be reliably separated with currently available arrays and spike sorting algorithms.^{26, 28} Thus, electrode array recordings have limited performance when dense

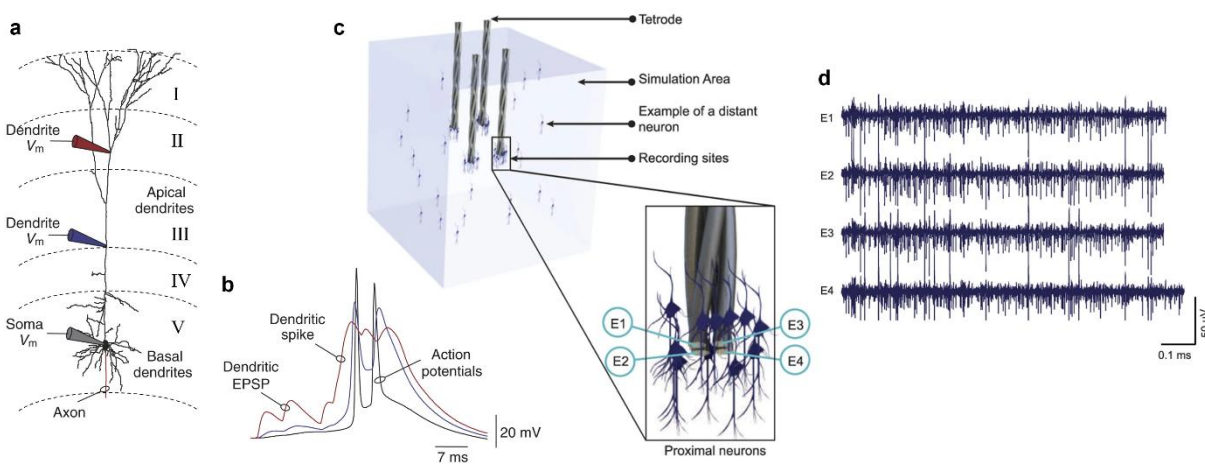


Figure 2 (a) The morphology of a layer 5 neocortical pyramidal neuron. The placement of dendritic and somatic whole-cell recording pipettes is indicated. (b) Dendritic spikes are evoked when dendritic excitatory synaptic inputs are clustered in time. The robust forward propagation of the dendritic spike through the apical dendrites to the soma results in the initiation of action potentials. Trace colours are designated according to pipette placement shown in (a). (c) Schematic illustration of extracellular recordings made by several tetrodes in hippocampal neuronal populations. (d) Typical signals attained from the four electrodes in one tetrode. Reproduced from references 10 and 18.

local neuronal assemblies need to be analyzed or when signals from specific types of near-by neurons need to be distinguished.

As discussed above, different parts of a neuron perform different functions and thus it is essential to make multisite observations over the whole structure of a single neuron; Numbers of neurons are active in the assembly during a complex behavior, it is obviously important to be able to monitor their activities simultaneously.⁷ To overcome the invasiveness of electrophysiology in these two applications, it has been highly desirable to develop new strategies that probe neuronal activity without the need for direct physical contact and provide adequate spatiotemporal resolution.^{8, 29}

1.2 Optical imaging of neuronal activity

A solution to the problem of physical contact required by electrophysiology, is the use of a transducer to transform electrical activity into a different signal that can travel through biological membranes.^{29, 30} In the last decades, optical imaging technique with requisite spatiotemporal resolution has become a valid complement to electrophysiology.^{31, 32} This section introduces some optical reporters, especially VSDs, that are extensively used in multisite optical imaging of neuronal activity in single neurons, even in the smallest neuronal structures, as well as in simultaneous imaging of the activity of neuronal populations.

1.2.1 Optical reporters

So far, there have been three main types of optical reporters that convert membrane potential changes or consequent effects into optical signals (Figure 3)²⁹: VSDs, voltage-sensitive fluorescent proteins, and calcium indicators (synthetic dyes or genetically encoded).

- Calcium indicators

There is a large calcium gradient across the plasma membrane of neurons, where the intracellular calcium concentration is far lower than the extracellular calcium concentration.³³ During the overshoot phase of action potentials, external calcium ions enter the neuron through calcium ion channels, increasing the internal calcium concentration by more than 10 times.³⁴ On binding calcium ions, synthetic or genetically encoded calcium indicators strongly fluoresce to report the changes in intracellular calcium concentration.³⁵⁻³⁸ The oscillations of intracellular calcium concentration are correlated to neuronal activity but not utterly faithful. Monitoring calcium signals has the problems of slow kinetics, signal saturation, and interference with intracellular calcium signaling machinery.³⁹ Therefore, calcium imaging cannot substitute for robust membrane potential sensors.

- Genetically encoded voltage sensors

The structure of a genetically encoded voltage sensor normally includes the voltage-sensitive domain of an ion channel to experience the potential changes across the plasma membrane, and one or two additional fluorescent proteins that alter their optical properties via conformational changes (e.g., Förster resonance energy transfer, or collisional quenching via the Dexter energy transfer).⁴⁰⁻⁴⁵ By linking the expression of genetically encoded voltage sensors to specific promoters, they have the major advantage of targeting specific cell types in the population.⁴⁶ However, their targeted expression is undermined by their delayed kinetics caused by slow conformational changes, making the detection of single action potential difficult.²⁹ In addition, they suffer from low brightness and high photobleaching, which largely constrain the illumination intensity and maximum possible imaging time.

- Voltage-sensitive dyes

VSDs are normally derivatives of hemicyanine or styryl chromophores.^{47,48} They usually have an electron rich π -system on one end and an electron deficient π -system on the other end, where the electrons switch from one end to the other upon excitation.⁴⁹ The membrane potential changes modulate the electron distribution and shift their emission spectra, namely the electrochromic

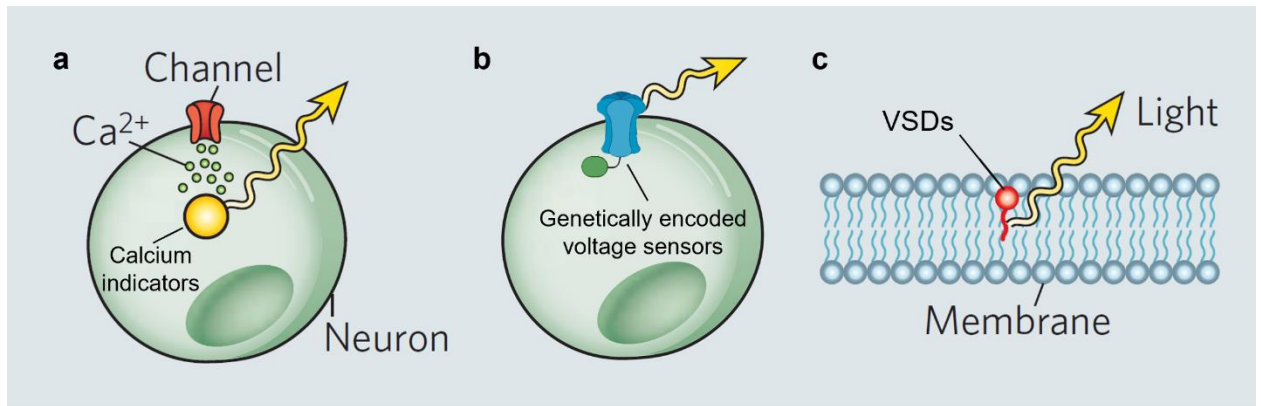


Figure 3 Schematic illustration of three main types of optical reporters. (a) VSDs embed within the plasma membrane of neurons and change their charge distribution and hence emission spectra depending on the membrane potential. (b) Genetically encoded voltage sensors that consist of a voltage-sensitive domain embedded within the plasma membrane and a fluorescent protein. Membrane potential changes induce the conformational change of the voltage sensors, thereby altering their fluorescence emission. (c) Calcium indicators (dyes or proteins) have a calcium binding domain and change their fluorescence emission to report intracellular calcium concentration. Reproduced from reference 29.

mechanism, also known as Stark effect.⁴⁹ This makes VSDs fast enough to track action potentials since only intramolecular charge redistribution is involved, without chromophore movement.⁴⁸

The plasma membrane is surrounded by charged substances that result in dielectric screening and thus the membrane potential rapidly dissipates with distance from the membrane.³¹ A voltage sensor must be located inside the membrane bilayer to actually experience the potential difference.³¹ The intrinsic amphiphilicity of VSDs facilitates to embed them perpendicularly into the membrane bilayer. The voltage-sensing mechanism of VSM is similar to VSDs, i.e., the quantum-confined Stark effect (QCSE) of QDs and charge state variation of NDs,⁵⁰⁻⁵³ which will be introduced later in Part II. Both of them are exogenous voltage sensors that require effective delivery and insertion into the plasma membrane bilayer for the optical imaging of neuronal activity. Therefore, the implementation of VSDs in multisite imaging of single neurons and simultaneous imaging of neuronal assemblies will be introduced in the next subsection, which may help to inspire the delivery strategies of VSM.

1.2.2 Imaging neuronal activity with voltage-sensitive dyes

- Multisite imaging of a single neuron

As introduced above (subsection 1.1.2), a major leap forward in studying the exceedingly complex functions of single neurons was made by multisite electrode recordings. However, the invasive character of electrodes makes it difficult to record the rapidly changing patterns of signal initiation and propagation in many subcellular structures.^{8, 54-57} Such measurements have been achieved using optical imaging by intracellular delivery of VSDs in brain slices or in vivo. Water-soluble VSDs can be delivered into individual neurons of interest through recording pipettes via free diffusion,^{58, 59} pressure (microinjection),⁶⁰ or electrical currents (microelectrophoresis, also known as iontophoresis).^{61, 62} Delivered VSDs spread into different remote regions of a single neuron and insert into the inner leaflet of the plasma membrane bilayer (Figure 4a).⁶³ Dyes that are bound to the membrane of intracellular organelles, do not change their fluorescence emission. These inactive dyes only contribute to the resting fluorescence.⁶⁴ For example, internally loaded VSDs were able to track the action potential propagation from many sites on small diameter axons and detect subthreshold signals in dendritic spines.

The precise location within the axon of neurons, where the action potential initiation occurs, is fundamental to the understanding of how neurons integrate synaptic inputs and convert them into an output signal. The small diameter of axons (less than 1 μm) makes it difficult to study their electrical properties using electrodes. In addition, multiple axonal sites need to be recorded simultaneously to localize the site of action potential initiation based on small differences in action potential latency. Optical imaging with internally loaded Di-2-ANEPEQ dyes (via free diffusion) successfully monitored action potential signals from multiple sites on the axon of pyramidal neurons in rat brain slices (Figure 4b).⁶⁵ It was revealed that action potentials are generated in the distal region of the initial segment of axons, $\sim 35 \mu\text{m}$ from the axon hillock.⁶⁶ The initial 40 μm of the axon is essential for action potential generation. These important findings indicate that the functions of axons are more complex than traditionally thought, which facilitated the rapid expanding of the field of axonal physiology.

Spines are membrane protrusions from dendrites, receiving most of the excitatory synaptic inputs.⁶⁷ They are of critical importance in learning and memory, where they process the electrical input signals and mediate synaptic plasticity.⁶⁸ However, due to their small sizes ($\sim 1 \mu\text{m}$) that are

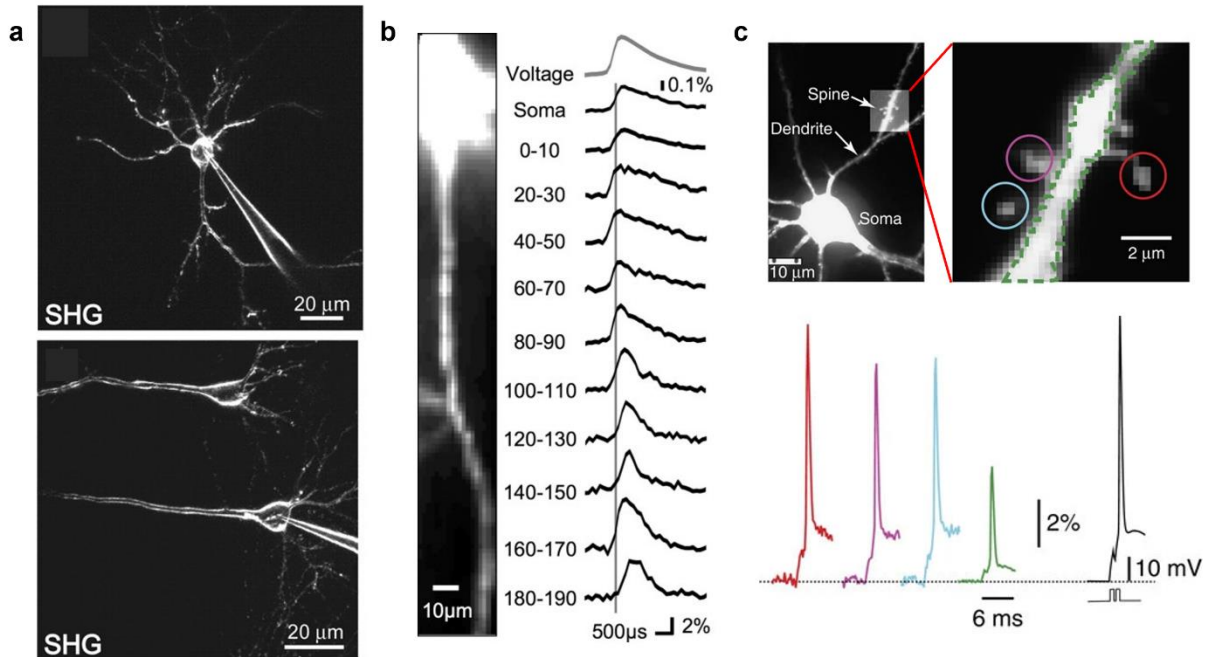


Figure 4 (a) Second harmonic generation (SHG) images showing the neurons in hippocampal brain slice intracellularly filled with FM4-64 dyes. (b) The axon of a layer 5 pyramidal neuron filled with Di-2-ANEPEQ dyes. Average fluorescence change ($\Delta F/F$) of 130 individually aligned action potentials measured at the indicated axonal locations. (c) Image of a neuron filled with Di-1-ANEPEQ dyes in optical voltage imaging. Subthreshold signals measured from multiple spines and dendrites (temporal average of 16 trails). Trace colours are designated according to indicated circles. Black traces are somatic patch electrode recording (upper) and current pulses for stimulation (lower). Reproduced from references 63, 65 and 70.

not accessible to electrodes, monitoring the generation and spread of subthreshold input signals from individual spines to the dendrite has been a major challenge.⁶⁹ Optical imaging with internally loaded Di-1-ANEPEQ dyes (via free diffusion) successfully monitored the subthreshold signals from individual spines and quantified the electrical resistance of the spine neck (Figure 4c).⁷⁰ The results demonstrated that spines on the basal dendrites are not electrically isolated by the spine neck. Spines with different morphological features behave the same in electrical signaling. These new findings disproved the previous theory positing that the electrical resistance of the spine neck largely determines the electrical properties of the spines.

- Simultaneous imaging of neuronal assemblies

The ability to monitor the electrical activity of numerous neurons in assemblies simultaneously is a prerequisite for understanding how the brain generates complex behavior and cognition.⁷¹ As

introduced above (subsection 1.1.2), the number of recordable and distinguishable neurons at a time using electrophysiological methods is highly restricted (Figure 5a).⁷² Optical imaging with extracellular delivery of VSDs offers a way past this limitation to visualize the large-scale activity of neuronal assemblies with high spatiotemporal resolution. VSDs can be loaded into brain slices or brain areas in vivo via bathing,⁷³⁻⁷⁵ or extracellular microinjection,⁶³ and then spontaneously label the plasma membrane. For example, the feasibility has been demonstrated on invertebrate ganglia, e.g., *Aplysia* and *Tritonia* pedal ganglia during the execution of motor programs.^{72, 76} VSDs RH155 were used to stain the pedal ganglia via bathing and track the action potentials of neuronal populations during the stimulation and execution of locomotion (*Aplysia*) and swim motor program (*Tritonia*). Optical signals were read out by a photodiode array that converted light to voltage (Figure 5b and c).⁷² Independent component analysis was used for sorting raw optical data into single neuron traces (Figure 5d).⁷⁶ Neurons with spiking similarity were grouped into clusters and mapped onto physical discrete regions of the ganglion (Figure 5e).⁷⁶ These results revealed that motor programs employ complex modular organizations of neuronal assemblies as dynamical building blocks in separated physical space, even in simple invertebrates.

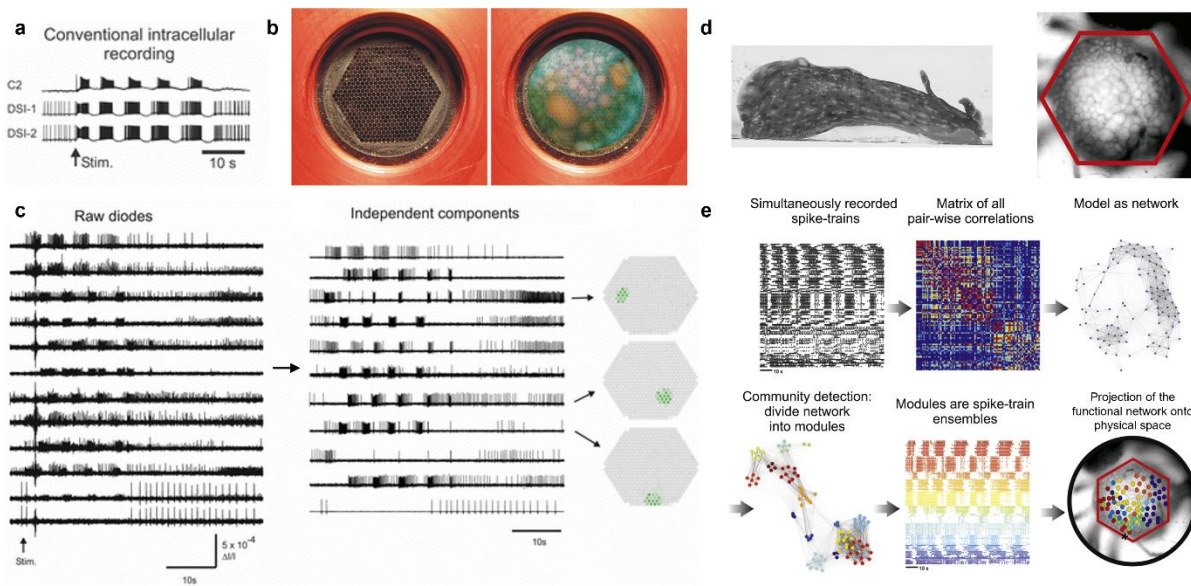


Figure 5 (a) Intracellular recordings of the *Tritonia* swim motor program using sharp electrode. The number of simultaneously recordable neurons is typically limited to 3 or 4. (b) The end of a fiber bundle (464 units) for the optical voltage imaging of an RH155-stained *Tritonia* pedal ganglion. The other end of these fibers was individually glued to photodiode array. (c) Sorting the raw data into a set of single-neuron traces using independent component analysis. Three traces were indicated on the fiber bundle maps with XY position and approximate neuron size. (d) Left: head reaches and muscular contraction of *Aplysia*'s rhythmic escape locomotion. Right: imaged area of the dorsal pedal ganglion of *Aplysia* on the fiber bundle with 464 units (red outline). (e) Schematic illustration of the steps for decoding neuronal assemblies using community detection with consensus clustering. Reproduced from references 72 and 76.

These studies clearly demonstrate the advantages of selective staining of single neurons by intracellular delivery of VSDs. This type of delivery strategy allows us to monitor the initiation and propagation of electrical signals in small neuronal processes from multiple locations in single neurons. VSDs imaging significantly advances our understanding of the remarkable functions of single neurons far beyond than that attained by multiple electrode recordings. Optical imaging with extracellular delivery of VSDs shows its superiority in the study of large-scale brain activity. This type of delivery strategy not only provides the location and propagation of activities, but also the synchrony, i.e., the fraction of neurons that are simultaneously activated in assemblies, which is hard to achieve with electrode arrays.⁷⁷

In spite of these substantial successes, currently available VSDs are burdened with several drawbacks, including low brightness, high photobleaching, and phototoxicity.⁷⁸ Therefore, they cannot monitor electrical events at the nanoscale with single molecules. In addition, to achieve improvements in the signal-to-noise ratio, a number of 4 - 9 trials will be necessary for signal averaging.^{8, 79} The photobleaching and phototoxicity effects become evident over time and thus they are particularly problematic for long-term imaging.^{66, 80} Moreover, they present a short retention time in the membrane and can perturb membrane capacitance at high concentrations. Overall, performing optical voltage imaging at the level of detection, where every electrical event in every location, deep in intact tissues or the brain of a live animal, can be monitored without averaging of multiple trials, is still being constrained.^{29, 81}

The poor optical stability and phototoxicity of currently available reporters raise the need for developing VSM with better performance. The superior optical and biocompatible properties of nanomaterials may provide far better performance than current reporters in robust optical imaging of neuronal activity. Nevertheless, the effective delivery strategies, i.e., the intracellular and extracellular delivery of VSDs, used in different scenarios, can serve as valuable references for the implementation of VSM in live neurons.

1.3 Voltage-sensitive nanomaterials

While further improvements in current optical reporters are expected, it has been shown that nanomaterials, such as QDs and NDs, are promising alternatives for sensing membrane potential changes in active neurons.^{82, 83} Their higher voltage sensitivity than that of VSDs will be discussed in Part II, where a multilayer device is used to examine their performance under external electrical fields in high throughput. Since the implementation of NDs for sensing membrane potential changes is still at nascent stage, this section will mainly introduce QDs and discuss their superior optical and biocompatible properties that surpass VSDs. Then this section will introduce two methods that are currently available for the extracellular delivery of QDs to image the activity of neuronal assemblies. These backgrounds point towards the objective of this thesis, that is to explore the intracellular delivery of QDs via microelectrophoresis technique, potentially for multisite voltage imaging of single neurons in brain slices or in vivo.

1.3.1 Quantum dots

QDs are semiconductor nanocrystals having sufficiently small sizes (2 - 10 nm) to exhibit quantum confinement effect. They are typically core/shell structured and made of cadmium, selenide, zinc and sulfide, having a variety of additional components and dopants. Recent advances in reproducible and high-throughput colloidal synthesis, such as the workstation for automated nanomaterials discovery and analysis (WANDA),^{84, 85} have enabled nanoscale construction of functional QDs with ever-increasing control over size, shape, composition, and sophisticated heterostructures (Figure 6a).⁸⁶ The automated synthesis approach allows efficient and multidimensional optimization of the unique photophysical properties of QDs that make them advantageous for optical voltage imaging.

First, the peak wavelength of the narrow and symmetrical Gaussian PL of QDs is tunable as a function of constituent core materials and size (quantum confinement effect), ranging from the ultraviolet to the near-infrared (Figure 6b).⁸⁶ Their broad and continuous absorption spectra enable the simultaneous excitation of QDs having different emission peaks using a single light source.⁸⁷ Second, the core/shell architecture of QDs can effectively improve their quantum yields and resistance to photobleaching in comparison with VSDs (Figure 6c).⁸⁸ Their exceptional brightness

and photostability not only offer a possibility of single-particle voltage measurements, but also improves the robustness in practical applications, obtaining a better signal-to-noise ratio.^{89,90} Third, QDs possess two-photon absorption cross sections ($\sigma \approx 10^3$ - 10^4 Goeppert Mayer units) that are orders of magnitude higher than VSDs and genetically encoded voltage sensors,^{91,92} where the use of near-IR excitation wavelengths is ideal for tissue-penetrating and thus beneficial for thick brain tissue or in vivo imaging.⁹³

Regarding biocompatibility, the outer shell of QDs not only prevents the leakage of heavy metal ions from core materials, but also enables versatile functionalization on the surface of QDs to decrease their toxicity (Figure 6d).⁹⁴ The cytotoxicity of QDs is determined by a number of factors, including size, surface modification, dose and delivery method, which should be optimized for particular applications.⁹⁵ While further efforts are required to improve their biocompatibility, it has been reported that QDs with properly modified surface showed less impact on cell viability than organic dyes in several instances.⁹⁶

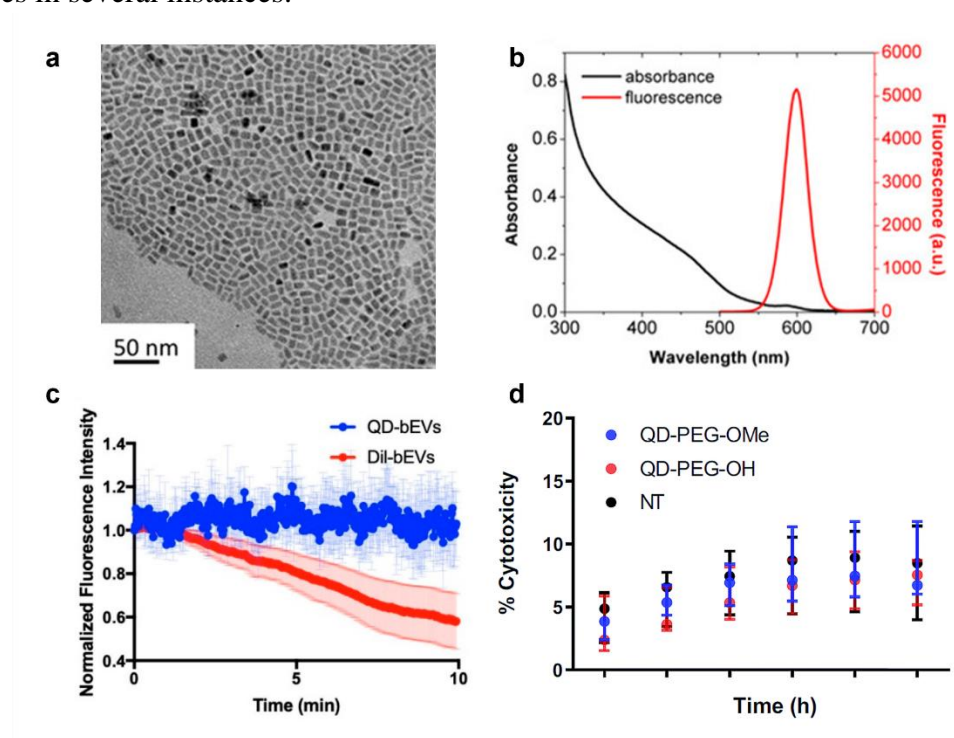


Figure 6 (a) Transmission electron microscopy (TEM) image of type-II ZnSe/CdS heterostructured QDs synthesized on WANDA. (b) The absorption and emission spectra of the QDs in (a). (c) Normalized fluorescence intensity of QDs and DiI (a common organic dyes) within the bilayer of brain extracellular vesicles as a function of time under 10 min same power laser exposure. (d) Cytotoxicity of poly (ethylene glycol)-5000k-methoxy modified QDs (QD-PEG-OMe), poly (ethylene glycol)-5000k-hydroxyl modified QDs (QD-PEG-OH) and non-treated (NT) group on *ex vivo* cultured organotypic whole hemisphere slices. Reproduced from references 86, 88 and 94.

1.3.2 Extracellular delivery of quantum dots for voltage imaging

To directly measure the membrane potential changes, QDs must be located inside the plasma membrane bilayer, which is the same for VSDs, as the membrane potential rapidly dissipates with distance (Figure 7a).^{31, 97} However, the thickness of plasma membrane is only ~ 4 nm, which is comparable with the size of QDs. Thus, even a minor displacement of QDs by a nanometer, can change their relative orientation to the membrane potential and easily undermine the sensitivity of the measurement.³¹ This leads to the significant challenges in the delivery, targeting, and membrane insertion of QDs.

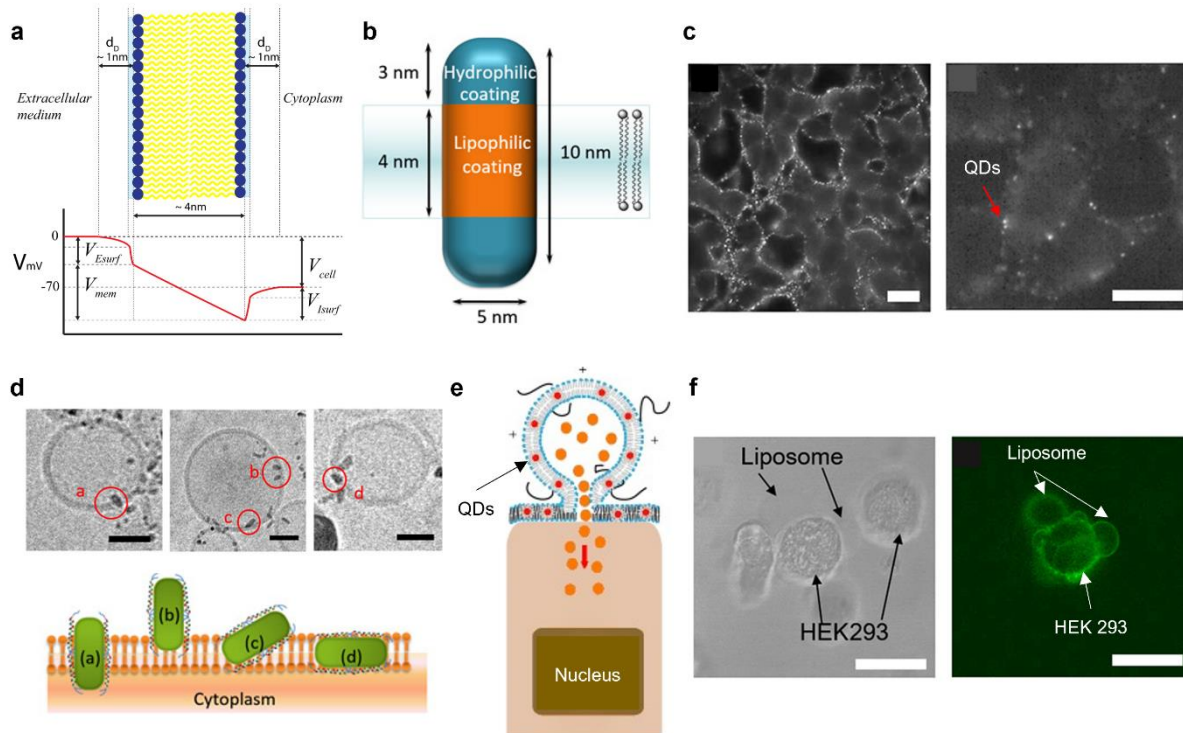


Figure 7 (a) Schematic illustration of the plasma membrane showing a simplified model of the relevant structures, potentials, and distances involved in membrane voltage sensing. (b) Design principles for the surface functionalization of NRs to facilitate their spontaneous insertion into the membrane with the correct orientation. (c) Peptide-coated NRs stained the plasma membrane via spontaneous insertion at high (left) and low (right) concentrations. Scale bars, 10 μ m. (d) Top: cryo-electron microscope images of peptide-coated NRs inserted into liposomes. Scale bars, 30 nm. Bottom: schematic illustration of possible NRs orientation relative to lipid bilayer, a: properly inserted, b: partially inserted, c: attached in an angle, d: horizontally embedded. (e) Schematic illustration of the interaction between liposomes with living cells. Orange dots in the interior of the liposome represent any deliverable water-soluble molecules. (f) Bright-field and fluorescence images of NR-loaded liposomes fused with the cell membrane. Scale bars, 10 μ m. Reproduced from references 31, 97, 98, and 101.

A recent novel attempt was made on rod-shaped asymmetric type-II QDs (CdSe/CdS), having length larger than the thickness of plasma membrane (Figure 7b).⁹⁸ This type of QDs present the largest sensitivity under electrical fields that orient along their long axis. Thus, to detect membrane potential changes, they need to be perpendicularly inserted into the membrane bilayer. The main component of plasma membrane is phospholipid, which contains a hydrophilic head facing the aqueous environment and two hydrophobic tails of fatty acids pointing inwards.⁹⁸ A unique peptide was rationally designed to have a hydrophilic flexible domain and a hydrophobic rigid helical domain that can selectively bind to the top and side of nanorods (NRs).⁹⁹ This provided NRs with a significant difference in the lipophilicity of different facets for perpendicular insertion into the lipid membrane. The performance of peptide-coated NRs was tested via spontaneous insertion and liposome fusion-mediated insertion in a transgenic line of the rapidly growing and easily cultured human embryonic kidney (HEK) 293 cells.⁹⁸ With stably expressed voltage-gated sodium and potassium ion channels, Na_v 1.3 and K_{IR} 2.1, this cell line exhibited self-spiking (~ 3 to 4 Hz) in membrane potential once they reached 80 – 95% confluency.¹⁰⁰ This would facilitate the ultimate applications of voltage-sensitive QDs/NRs in neuronal cells.

- Spontaneous insertion

Peptide-coated NRs were added directly to the culture medium of self-spiking HEK293 cells and self-inserted into the plasma membrane.⁹⁸ By controlling the concentration of NRs, the density of NRs in the plasma membrane was adjusted to either low or high, where individual or small aggregates of NRs were observed (Figure 7c).⁹⁸ Within one hour after the staining, the loss of the diffraction-limited fluorescence from membrane inserted NRs indicated that they were taken up by the cells via endocytosis. These inserted NRs were able to track the membrane potential changes of HEK293 cells, but they exhibited a quite poor sensitivity ($\Delta F/F$ of $\sim 0.6\%$) that was much lower than a commonly used VSDs (di-8-ANEPPS, $\Delta F/F$ of $\sim 10\%$). This was caused by the imperfect orientation of NRs during spontaneous insertion, where only 16% of them were oriented symmetrically and perpendicularly, while the others were either partially, tilted or horizontally inserted (Figure 7d).⁹⁸

- Liposome fusion-mediated insertion

Peptide-coated NRs were also loaded into the plasma membrane via liposome fusion process, based on previously reported methods.¹⁰¹⁻¹⁰⁶ NRs were incorporated into the bilayer membrane of liposomes, which were then fused with the plasma membrane of HEK293 cells while transferring any water-soluble cargo into the cytoplasm (Figure 7e).¹⁰¹ When NR-loaded liposomes were added to HEK293 cell culture, their instantaneous fusion with cell membrane was observed under bright-field and fluorescence microscopy (Figure 7f).⁹⁸ The orientation of NRs loaded in liposomes was still not ideal to guarantee maximal QCSE charge separation for achieving the highest voltage sensitivity. The surface modification of NRs is still being improved to minimize the dynamic movement and orientation fluctuation of NRs within the membrane.^{107, 108}

Both methods are staining the plasma membrane via extracellular delivery of QDs or QD-loaded liposomes that are directly added into the cell culture medium. Similarly applied to VSDs, this strategy is intended for simultaneous voltage imaging of neuronal assemblies. For multisite voltage imaging of single neurons, the strategy of choice is to deliver QDs into individual neurons of interest. Like VSDs, amphiphilic QDs are expected to spread into distal processes and then insert into the plasma membrane bilayer, being able to monitor the electrical activity in small neuronal structures, such as thin axons and dendritic spines.

1.4 Microelectrophoretic delivery of nanomaterials

As introduced above (subsection 1.2.2), voltage imaging of multiple subcellular structures can only be achieved if individual neurons are stained by the intracellular delivery of VSDs in brain slices or *in vivo*.⁸ VSDs can be internally loaded through recording pipettes via free diffusion, microinjection or microelectrophoresis. This section will compare these three methods and point out the research gap in the intracellular delivery of nanomaterials using microelectrophoresis technique, which is the core work of Part I in this thesis.

1.4.1 Summary of methods for monitoring neuronal activity

Figure 8a summarizes the strategies for monitoring neuronal activity that have been discussed in the sections above. Depending on the needs of the experiment, electrophysiology employs multiple electrodes for the multisite recordings of a single neuron, or electrode array for the simultaneous recordings of neuronal assemblies. Optical voltage imaging with extracellular delivery of VSDs or VSM enables the visualization of large-scale activity of neuronal assemblies, while the intracellular delivery of VSDs enables the imaging of the rapidly changing patterns of signal initiation and propagation in many subcellular structures of single neurons. Figure 8b shows the different methods that have been used on VSDs or VSM for their intracellular and extracellular delivery. For simultaneous imaging of neuronal assemblies, both VSDs, nanomaterials, and nanomaterial-loaded liposomes are able to spontaneously insert into/fuse with the plasma membrane via bathing with cell cultures or brain slices. VSDs can also be loaded into brain tissues *in vivo* via extracellular microinjection. For multisite imaging of single neurons, free diffusion, microinjection and microelectrophoresis techniques, have been demonstrated on the delivery of VSDs into individual neurons, but not yet been tested on VSM.

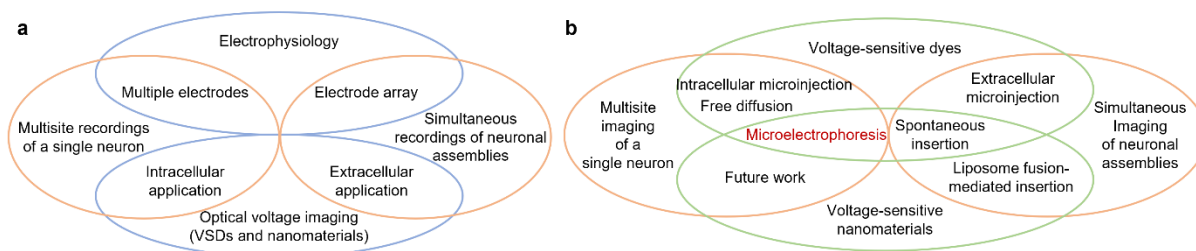


Figure 8 Summary of different methods employed by electrophysiology and optical voltage imaging for monitoring neuronal activity at different spatiotemporal scales. Microelectrophoresis is highlighted in red and is the core work of this thesis for the intracellular application of VSM used in the multisite voltage imaging of single neurons.

1.4.2 Advantages of microelectrophoresis technique

Whether the injected voltage sensors can spread from the injection site (soma) into distal dendrites and axon, is the most critical question to consider for their successful intracellular delivery. This is determined by the solubility of voltage sensors as well as the delivery method. Early attempts in the intracellular delivery of VSDs (e.g., di-4-ANEPPS) were failed since these

VSDs were too lipophilic to dissolve in aqueous solution and thus were difficult to be ejected out of the recording pipettes. Even if they were injected into the soma, they would not spread into the distal regions. With the development of water-soluble VSDs (e.g., di-8-ANEPPQ and di-12-ANEPEQ) having higher intracellular diffusion rate, it was possible to image the membrane potential changes from distal regions of single neurons, such as dendritic spine.^{67, 109}

The delivery method also has an impact on the intracellular spread of voltage sensors. The time needed for filling the entire neuron with VSDs, including distal regions, is typically from 15 to 60 mins via free diffusion,^{58, 59, 65, 66, 110, 111} roughly 30 mins via microinjection (5 - 60 psi pressure),¹¹² and from 1 to 20 mins via microelectrophoresis (0.25 - 0.5 nA),^{56, 61, 62} all depending on the length of neuronal processes. Both microinjection and microelectrophoresis techniques facilitate the diffusion of VSDs and reduce the injection duration to minimize the damage to the neurons. However, the major problem of microinjection is the leakage of VSDs from the pipettes into the extracellular medium before piercing the neurons, which may cause signal contamination. In addition, the relatively large volume of solvent that is ejected along with VSDs, may cause mechanical deformation of, and possible damage to the cells and tissues. In comparison, for microelectrophoresis technique, a retaining current can be used before intracellular delivery to control the leakage of VSDs from recording pipettes.^{113, 114} The fine electrophoretic propulsion only drives charged substances into the neurons rather than high pressure pulses, which preserves higher cell viability post injection. The advantages of microelectrophoresis technique will be discussed in detail in the introduction of Publication 1 and 2.

Overall, microelectrophoresis technique shows several critical advantages for the intracellular delivery of VSDs and could be potentially used for VSM.

1.5 Part I aims and scope

This project aims to perform intracellular delivery of nanomaterials (QDs as an example) into live cells using microelectrophoresis technique. In a broader perspective, the research is aimed at

providing an effective approach for the intracellular delivery of VSM for the multisite voltage imaging of single neurons in brain slices or in vivo. The study focuses on three key objectives:

1. To explore the feasibility of using microelectrophoresis technique for the intracellular delivery of nanomaterials into live cells.
2. To investigate the intracellular fate of delivered nanomaterials inside live cells.
3. To investigate the impact of microelectrophoretic delivery of nanomaterials on the cell viability.

The following chapters will describe the work on addressing these objectives.

1.6 References

1. Purves, D.; Williams, S. M.; White, L. E.; Mace, A. C., *Neuroscience*. 3rd ed. ed.; Sinauer Associates: Sunderland, Mass, **2004**.
2. Bean, B. P., The Action Potential in Mammalian Central Neurons. *Nat Rev Neurosci* **2007**, 8 (6), 451-65.
3. Longstaff, A., *Instant Notes in Neuroscience*. CRC Press LLC: Oxford, GBR, UNITED KINGDOM, **2000**.
4. Carter, M.; Shieh, J. C., Chapter 4 - Electrophysiology. In *Guide to Research Techniques in Neuroscience*, Carter, M.; Shieh, J. C., Eds. Academic Press: New York, **2010**; pp 91-118.
5. Sidiropoulou, K.; Pissadaki, E. K.; Poirazi, P., Inside the Brain of a Neuron. *EMBO reports* **2006**, 7 (9), 886-892.
6. Spruston, N., Pyramidal Neurons: Dendritic Structure and Synaptic Integration. *Nature reviews. Neuroscience* **2008**, 9 (3), 206-221.
7. Braubach, O.; Cohen, L. B.; Choi, Y., Historical Overview and General Methods of Membrane Potential Imaging. In *Membrane Potential Imaging in the Nervous System and Heart*, Canepari, M.; Zecevic, D.; Bernus, O., Eds. Springer International Publishing: Cham, **2015**; pp 3-26.
8. Popovic, M.; Vogt, K.; Holthoff, K.; Konnerth, A.; Salzberg, B. M.; Grinvald, A.; Antic, S. D.; Canepari, M.; Zecevic, D., Imaging Submillisecond Membrane Potential Changes from Individual Regions of Single Axons, Dendrites and Spines. In *Membrane Potential Imaging in the Nervous System and Heart*, Canepari, M.; Zecevic, D.; Bernus, O., Eds. Springer International Publishing: Cham, **2015**; pp 57-101.
9. Rall, W.; Segev, I.; Rinzel, J.; Shepherd, G. M., *The Theoretical Foundation of Dendritic Function : Selected Papers of Wilfrid Rall with Commentaries*. MIT Press: Cambridge, Mass, **1995**.

10. Williams, S. R.; Atkinson, S. E., Dendritic Synaptic Integration in Central Neurons. *Current Biology* **2008**, *18* (22), R1045-R1047.
11. Williams, S. R.; Stuart, G. J., Dependence of Epsp Efficacy on Synapse Location in Neocortical Pyramidal Neurons. *Science* **2002**, *295* (5561), 1907-10.
12. Williams, S. R., Spatial Compartmentalization and Functional Impact of Conductance in Pyramidal Neurons. *Nature Neuroscience* **2004**, *7* (9), 961-967.
13. Losonczy, A.; Makara, J. K.; Magee, J. C., Compartmentalized Dendritic Plasticity and Input Feature Storage in Neurons. *Nature (London)* **2008**, *452* (7186), 436-441.
14. Morris, R. G., D.O. Hebb: The Organization of Behavior, Wiley: New York; 1949. *Brain Res Bull* **1999**, *50* (5-6), 437.
15. Grinvald, A.; Omer, D.; Naaman, S.; Sharon, D., Imaging the Dynamics of Mammalian Neocortical Population Activity in-Vivo. *Adv Exp Med Biol* **2015**, *859*, 243-71.
16. Gold, C.; Henze, D. A.; Koch, C.; Buzsaki, G., On the Origin of the Extracellular Action Potential Waveform: A Modeling Study. *Journal of Neurophysiology* **2006**, *95* (5), 3113-3128.
17. Lindén, H.; Hagen, E.; Leški, S.; Norheim, E. S.; Pettersen, K. H.; Einevoll, G. T., Lfpy: A Tool for Biophysical Simulation of Extracellular Potentials Generated by Detailed Model Neurons. *Frontiers in neuroinformatics* **2013**, *7* (Jan), 41-41.
18. Mondragón-González, S. L.; Burguière, E., Bio-Inspired Benchmark Generator for Extracellular Multi-Unit Recordings. *Scientific Reports* **2017**, *7* (1), 43253.
19. Gao, H.; Solages, C. d.; Lena, C., Tetrode Recordings in the Cerebellar Cortex. *Journal of Physiology-Paris* **2012**, *106* (3), 128-136.
20. Kapoor, V.; Krampe, E.; Klug, A.; Logothetis, N. K.; Panagiotaropoulos, T. I., Development of Tube Tetrodes and a Multi-Tetrode Drive for Deep Structure Electrophysiological Recordings in the Macaque Brain. *Journal of Neuroscience Methods* **2013**, *216* (1), 43-48.
21. Rangel Guerrero, D. K.; Donnett, J. G.; Csicsvari, J.; Kovács, K. A., Tetrode Recording from the Hippocampus of Behaving Mice Coupled with Four-Point-Irradiation Closed-Loop

Optogenetics: A Technique to Study the Contribution of Hippocampal Swr Events to Learning. *eneuro* **2018**, 5 (4), ENEURO.0087-18.2018.

22. Mou, X.; Ji, D., Large-Scale Tetrode Recording in the Rodent Hippocampus. Springer New York: New York, NY, **2017**; pp 87-107.

23. Buzsáki, G., Large-Scale Recording of Neuronal Ensembles. *Nature Neuroscience* **2004**, 7 (5), 446-451.

24. Chen, R.; Canales, A.; Anikeeva, P., Neural Recording and Modulation Technologies. *Nat Rev Mater* **2017**, 2 (2).

25. Gibson, S.; Judy, J. W.; Marković, D., Spike Sorting: The First Step in Decoding the Brain: The First Step in Decoding the Brain. *IEEE Signal processing magazine* **2011**, 29 (1), 124-143.

26. Rey, H. G.; Pedreira, C.; Quian Quiroga, R., Past, Present and Future of Spike Sorting Techniques. *Brain Research Bulletin* **2015**, 119, 106-117.

27. Lewicki, M. S., A Review of Methods for Spike Sorting: The Detection and Classification of Neural Action Potentials. *Network: Computation in Neural Systems* **1998**, 9 (4), R53-R78.

28. Barthó, P.; Hirase, H.; Monconduit, L.; Zugaro, M.; Harris, K. D.; Buzsáki, G., Characterization of Neocortical Principal Cells and Interneurons by Network Interactions and Extracellular Features. *Journal of Neurophysiology* **2004**, 92 (1), 600-608.

29. Scanziani, M.; Häusser, M., Electrophysiology in the Age of Light. *Nature* **2009**, 461 (7266), 930-939.

30. Knöpfel, T.; Song, C., Optical Voltage Imaging in Neurons: Moving from Technology Development to Practical Tool. *Nature Reviews Neuroscience* **2019**, 20 (12), 719-727.

31. Peterka, D. S.; Takahashi, H.; Yuste, R., Imaging Voltage in Neurons. *Neuron* **2011**, 69 (1), 9-21.

32. Ji, N.; Shroff, H.; Zhong, H.; Betzig, E., Advances in the Speed and Resolution of Light Microscopy. *Current opinion in neurobiology* **2008**, 18 (6), 605-616.

33. Bagur, R.; Hajnóczky, G., Intracellular Ca²⁺ Sensing: Its Role in Calcium Homeostasis and Signaling. *Mol Cell* **2017**, *66* (6), 780-788.
34. Kaiser, K. M. M.; Lubke, J.; Zilberter, Y.; Sakmann, B., Postsynaptic Calcium Influx at Single Synaptic Contacts between Pyramidal Neurons and Bitufted Interneurons in Layer 2/3 of Rat Neocortex Is Enhanced by Backpropagating Action Potentials. *The Journal of neuroscience* **2004**, *24* (6), 1319-1329.
35. Tian, L.; Hires, S. A.; Mao, T.; Huber, D.; Chiappe, M. E.; Chalasani, S. H.; Petreanu, L.; Akerboom, J.; McKinney, S. A.; Schreiter, E. R.; Bargmann, C. I.; Jayaraman, V.; Svoboda, K.; Looger, L. L., Imaging Neural Activity in Worms, Flies and Mice with Improved Gcamp Calcium Indicators. *Nature Methods* **2009**, *6* (12), 875-881.
36. Sabatini, B. L.; Oertner, T. G.; Svoboda, K., The Life Cycle of Ca²⁺ Ions in Dendritic Spines. *Neuron* **2002**, *33* (3), 439-452.
37. Wallace, D. J.; zum Alten Borgloh, S. M.; Astori, S.; Yang, Y.; Bausen, M.; Kügler, S.; Palmer, A. E.; Tsien, R. Y.; Sprengel, R.; Kerr, J. N. D.; Denk, W.; Hasan, M. T., Single-Spike Detection in Vitro and in Vivo with a Genetic Ca²⁺ Sensor. *Nature Methods* **2008**, *5* (9), 797-804.
38. Dombeck, D. A.; Khabbaz, A. N.; Collman, F.; Adelman, T. L.; Tank, D. W., Imaging Large-Scale Neural Activity with Cellular Resolution in Awake, Mobile Mice. *Neuron* **2007**, *56* (1), 43-57.
39. Efros, A. L.; Delehanty, J. B.; Huston, A. L.; Medintz, I. L.; Barbic, M.; Harris, T. D., Evaluating the Potential of Using Quantum Dots for Monitoring Electrical Signals in Neurons. *Nature nanotechnology* **2018**, *13* (4), 278-288.
40. Siegel, M. S.; Isacoff, E. Y., A Genetically Encoded Optical Probe of Membrane Voltage. *Neuron* **1997**, *19* (4), 735-741.
41. Baker, B. J.; Mutoh, H.; Dimitrov, D.; Akemann, W.; Perron, A.; Iwamoto, Y.; Jin, L.; Cohen, L. B.; Isacoff, E. Y.; Pieribone, V. A.; Hughes, T.; Knöpfel, T., Genetically Encoded Fluorescent Sensors of Membrane Potential. *Brain Cell Biology* **2008**, *36* (1), 53.

42. Shroff, S. N.; Das, S. L.; Tseng, H.-a.; Noueihed, J.; Fernandez, F.; White, J. A.; Chen, C. S.; Han, X., Voltage Imaging of Cardiac Cells and Tissue Using the Genetically Encoded Voltage Sensor Archon1. *iScience* **2020**, *23* (4), 100974.
43. Chen, T.-W.; Wardill, T. J.; Looger, L. L.; Svoboda, K.; Kim, D. S.; Yi, S. U. N.; Pulver, S. R.; Renninger, S. L.; Baohan, A.; Schreiter, E. R.; Kerr, R. A.; Orger, M. B.; Jayaraman, V., Ultrasensitive Fluorescent Proteins for Imaging Neuronal Activity. *Nature (London)* **2013**, *499* (7458), 295-300.
44. Beck, C.; Gong, Y., A High-Speed, Bright, Red Fluorescent Voltage Sensor to Detect Neural Activity. *Scientific Reports* **2019**, *9* (1), 15878.
45. Haider, T. A.; Knöpfel, T., Voltage-Sensitive Fluorescent Proteins for Optical Electrophysiology. In *Neural Interface Engineering: Linking the Physical World and the Nervous System*, Guo, L., Ed. Springer International Publishing: Cham, **2020**; pp 383-407.
46. Blunck, R.; Chanda, B.; Bezanilla, F., Nano to Micro — Fluorescence Measurements of Electric Fields in Molecules and Genetically Specified Neurons. *The Journal of Membrane Biology* **2005**, *208* (2), 91-102.
47. Loew, L. M., Chapter Fourteen - Potentiometric Membrane Dyes and Imaging Membrane Potential in Single Cells. Second Edition ed.; Elsevier Ltd: **1999**; pp 210-221.
48. Yan, P.; Acker, C. D.; Zhou, W.-L.; Lee, P.; Bollensdorff, C.; Negrean, A.; Lotti, J.; Sacconi, L.; Antic, S. D.; Kohl, P.; Mansvelder, H. D.; Pavone, F. S.; Loew, L. M., Palette of Fluorinated Voltage-Sensitive Hemicyanine Dyes. *Proceedings of the National Academy of Sciences* **2012**, *109* (50), 20443.
49. Loew, L. M., Design and Use of Organic Voltage Sensitive Dyes. In *Membrane Potential Imaging in the Nervous System and Heart*, Canepari, M.; Zecevic, D.; Bernus, O., Eds. Springer International Publishing: Cham, **2015**; pp 27-53.
50. Miller, D. A. B.; Chemla, D. S.; Damen, T. C.; Gossard, A. C.; Wiegmann, W.; Wood, T. H.; Burrus, C. A., Band-Edge Electroabsorption in Quantum Well Structures: The Quantum-Confinement Stark Effect. *Physical review letters* **1984**, *53* (22), 2173-2176.

51. Park, K.; Deutsch, Z.; Li, J. J.; Oron, D.; Weiss, S., Single Molecule Quantum-Confined Stark Effect Measurements of Semiconductor Nanoparticles at Room Temperature. *ACS Nano* **2012**, *6* (11), 10013-10023.
52. Karaveli, S.; Gaathon, O.; Wolcott, A.; Sakakibara, R.; Shemesh, O. A.; Peterka, D. S.; Boyden, E. S.; Owen, J. S.; Yuste, R.; Englund, D., Modulation of Nitrogen Vacancy Charge State and Fluorescence in Nanodiamonds Using Electrochemical Potential. *Proc Natl Acad Sci U S A* **2016**, *113* (15), 3938-43.
53. Rowland, C. E.; Susumu, K.; Stewart, M. H.; Oh, E.; Mäkinen, A. J.; O'Shaughnessy, T. J.; Kushto, G.; Wolak, M. A.; Erickson, J. S.; L. Efros, A.; Huston, A. L.; Delehanty, J. B., Electric Field Modulation of Semiconductor Quantum Dot Photoluminescence: Insights into the Design of Robust Voltage-Sensitive Cellular Imaging Probes. *Nano Letters* **2015**, *15* (10), 6848-6854.
54. Baker, B. J.; Kosmidis, E. K.; Vucinic, D.; Falk, C. X.; Cohen, L. B.; Djurisic, M.; Zecevic, D., Imaging Brain Activity with Voltage- and Calcium-Sensitive Dyes. *Cellular and Molecular Neurobiology* **2005**, *25* (2), 245-282.
55. Kuhn, B.; Roome, C. J., Primer to Voltage Imaging with Anionic Dyes and Two-Photon Microscopy. *Frontiers in Cellular Neuroscience* **2019**, *13* (321).
56. Roome, C. J.; Kuhn, B., Simultaneous Dendritic Voltage and Calcium Imaging and Somatic Recording from Purkinje Neurons in Awake Mice. *Nature Communications* **2018**, *9* (1), 3388.
57. Andrásfalvy, B. K.; Galiñanes, G. L.; Huber, D.; Barbic, M.; Macklin, J. J.; Susumu, K.; Delehanty, J. B.; Huston, A. L.; Makara, J. K.; Medintz, I. L., Quantum Dot-Based Multiphoton Fluorescent Pipettes for Targeted Neuronal Electrophysiology. *Nature methods* **2014**, *11* (12), 1237-1241.
58. Antic, S. D., Action Potentials in Basal and Oblique Dendrites of Rat Neocortical Pyramidal Neurons. *The Journal of physiology* **2003**, *550* (Pt 1), 35-50.
59. Antic, S.; Major, G.; Zecevic, D., Fast Optical Recordings of Membrane Potential Changes from Dendrites of Pyramidal Neurons. *Journal of Neurophysiology* **1999**, *82* (3), 1615-1621.

60. Antić, S.; Zecević, D., Optical Signals from Neurons with Internally Applied Voltage-Sensitive Dyes. *J Neurosci* **1995**, *15* (2), 1392-405.
61. Grinvald, A.; Salzberg, B. M.; Lev-Ram, V.; Hildesheim, R., Optical Recording of Synaptic Potentials from Processes of Single Neurons Using Intracellular Potentiometric Dyes. *Biophysical Journal* **1987**, *51* (4), 643-651.
62. Obaid, A.; Shimizu, H.; Salzberg, B. In *Intracellular Staining with Potentiometric Dyes: Optical Signals from Identified Leech Neurons and Their Processes*, BIOLOGICAL BULLETIN, MARINE BIOLOGICAL LABORATORY 7 MBL ST, WOODS HOLE, MA 02543: **1982**; pp 388-389.
63. Dombeck, D. A.; Sacconi, L.; Blanchard-Desce, M.; Webb, W. W., Optical Recording of Fast Neuronal Membrane Potential Transients in Acute Mammalian Brain Slices by Second-Harmonic Generation Microscopy. *Journal of Neurophysiology* **2005**, *94* (5), 3628-3636.
64. Jaafari, N.; Vogt, K. E.; Saggau, P.; Leslie, L. M.; Zecevic, D.; Canepari, M., Combining Membrane Potential Imaging with Other Optical Techniques. In *Membrane Potential Imaging in the Nervous System and Heart*, Canepari, M.; Zecevic, D.; Bernus, O., Eds. Springer International Publishing: Cham, **2015**; pp 103-125.
65. Palmer, L. M.; Stuart, G. J., Site of Action Potential Initiation in Layer 5 Pyramidal Neurons. *J Neurosci* **2006**, *26* (6), 1854-1863.
66. Popovic, M. A.; Foust, A. J.; McCormick, D. A.; Zecevic, D., The Spatio-Temporal Characteristics of Action Potential Initiation in Layer 5 Pyramidal Neurons: A Voltage Imaging Study. *J Physiol* **2011**, *589* (17), 4167-87.
67. Palmer, L. M.; Stuart, G. J., Membrane Potential Changes in Dendritic Spines During Action Potentials and Synaptic Input. *J Neurosci* **2009**, *29* (21), 6897-6903.
68. Nuriya, M.; Jiang, J.; Nemet, B.; Eisenthal, K. B.; Yuste, R., Imaging Membrane Potential in Dendritic Spines. *Proceedings of the National Academy of Sciences - PNAS* **2006**, *103* (3), 786-790.

69. Araya, R.; Jiang, J.; Eiselthal, K. B.; Yuste, R., The Spine Neck Filters Membrane Potentials. *Proceedings of the National Academy of Sciences - PNAS* **2006**, *103* (47), 17961-17966.
70. Popovic, M. A.; Carnevale, N.; Rozsa, B.; Zecevic, D., Electrical Behaviour of Dendritic Spines as Revealed by Voltage Imaging. *Nat Commun* **2015**, *6*, 8436.
71. Alivisatos, A. P.; Chun, M.; Church, George M.; Greenspan, Ralph J.; Roukes, Michael L.; Yuste, R., The Brain Activity Map Project and the Challenge of Functional Connectomics. *Neuron (Cambridge, Mass.)* **2012**, *74* (6), 970-974.
72. Frost, W. N.; Brandon, C. J.; Bruno, A. M.; Humphries, M. D.; Moore-Kochlacs, C.; Sejnowski, T. J.; Wang, J.; Hill, E. S., Monitoring Spiking Activity of Many Individual Neurons in Invertebrate Ganglia. In *Membrane Potential Imaging in the Nervous System and Heart*, Canepari, M.; Zecevic, D.; Bernus, O., Eds. Springer International Publishing: Cham, **2015**; pp 127-145.
73. Grinvald, A.; Hildesheim, R., VSDI: A New Era in Functional Imaging of Cortical Dynamics. *Nature Reviews Neuroscience* **2004**, *5* (11), 874-885.
74. Grinvald, A.; Shoham, D.; Shmuel, A.; Glaser, D.; Vanzetta, I.; Shtoyerman, E.; Sloviter, H.; Wijnbergen, C.; Hildesheim, R.; Arieli, A., In-Vivo Optical Imaging of Cortical Architecture and Dynamics. In *Modern Techniques in Neuroscience Research*, Windhorst, U.; Johansson, H., Eds. Springer Berlin Heidelberg: Berlin, Heidelberg, **1999**; pp 893-969.
75. Grinvald, A.; Petersen, C. C. H., Imaging the Dynamics of Neocortical Population Activity in Behaving and Freely Moving Mammals. In *Membrane Potential Imaging in the Nervous System and Heart*, Canepari, M.; Zecevic, D.; Bernus, O., Eds. Springer International Publishing: Cham, **2015**; pp 273-296.
76. Bruno, Angela M.; Frost, William N.; Humphries, Mark D., Modular Deconstruction Reveals the Dynamical and Physical Building Blocks of a Locomotion Motor Program. *Neuron* **2015**, *86* (1), 304-318.
77. Jin, W.; Zhang, R.-J.; Wu, J.-y., Voltage-Sensitive Dye Imaging of Population Neuronal Activity in Cortical Tissue. *Journal of Neuroscience Methods* **2002**, *115* (1), 13-27.

78. Tai, D. C. S.; Caldwell, B. J.; LeGrice, I. J.; Hooks, D. A.; Pullan, A. J.; Smaill, B. H., Correction of Motion Artifact in Transmembrane Voltage-Sensitive Fluorescent Dye Emission in Hearts. *American Journal of Physiology - Heart and Circulatory Physiology* **2004**, *287* (3), 985-993.
79. Sjulson, L.; Miesenböck, G., Optical Recording of Action Potentials and Other Discrete Physiological Events: A Perspective from Signal Detection Theory. *Physiology* **2007**, *22* (1), 47-55.
80. Preuss, S.; Stein, W., Comparison of Two Voltage-Sensitive Dyes and Their Suitability for Long-Term Imaging of Neuronal Activity. *PLOS ONE* **2013**, *8* (10), e75678.
81. Tsytsarev, V.; Liao, L. D.; Kong, K. V.; Liu, Y. H.; Erzurumlu, R. S.; Olivo, M.; Thakor, N. V., Recent Progress in Voltage-Sensitive Dye Imaging for Neuroscience. *J Nanosci Nanotechnol* **2014**, *14* (7), 4733-44.
82. Rivnay, J.; Wang, H.; Fenno, L.; Deisseroth, K.; Malliaras George, G., Next-Generation Probes, Particles, and Proteins for Neural Interfacing. *Science Advances* **2017**, *3* (6), e1601649.
83. Nag, O. K.; Muroski, M. E.; Hastman, D. A.; Almeida, B.; Medintz, I. L.; Huston, A. L.; Delehanty, J. B., Nanoparticle-Mediated Visualization and Control of Cellular Membrane Potential: Strategies, Progress, and Remaining Issues. *ACS Nano* **2020**, *14* (3), 2659-2677.
84. Chan, E. M.; Xu, C.; Mao, A. W.; Han, G.; Owen, J. S.; Cohen, B. E.; Milliron, D. J., Reproducible, High-Throughput Synthesis of Colloidal Nanocrystals for Optimization in Multidimensional Parameter Space. *Nano Letters* **2010**, *10* (5), 1874-1885.
85. Epps, R. W.; Abolhasani, M., Modern Nanoscience: Convergence of Ai, Robotics, and Colloidal Synthesis. *Applied Physics Reviews* **2021**, *8* (4), 041316.
86. Kuo, Y.; Li, J.; Michalet, X.; Chizhik, A.; Meir, N.; Bar-Elli, O.; Chan, E.; Oron, D.; Enderlein, J.; Weiss, S., Characterizing the Quantum-Confined Stark Effect in Semiconductor Quantum Dots and Nanorods for Single-Molecule Electrophysiology. *ACS Photonics* **2018**, *5* (12), 4788-4800.

87. Wolfbeis, O. S., An Overview of Nanoparticles Commonly Used in Fluorescent Bioimaging. *Chemical Society Reviews* **2015**, *44* (14), 4743-4768.
88. Zhang, M.; Vojtech, L.; Ye, Z.; Hladik, F.; Nance, E., Quantum Dot Labeling and Visualization of Extracellular Vesicles. *ACS Applied Nano Materials* **2020**, *3* (7), 7211-7222.
89. Lichtman, J. W.; Conchello, J. A., Fluorescence Microscopy. *Nat Methods* **2005**, *2* (12), 910-9.
90. Reineck, P.; Francis, A.; Orth, A.; Lau, D. W. M.; Nixon-Luke, R. D. V.; Rastogi, I. D.; Razali, W. A. W.; Cordina, N. M.; Parker, L. M.; Sreenivasan, V. K. A., Brightness and Photostability of Emerging Red and near-Ir Fluorescent Nanomaterials for Bioimaging. *Advanced Optical Materials* **2016**, *4* (10), 1549-1557.
91. Kuhn, B.; Fromherz, P.; Denk, W., High Sensitivity of Stark-Shift Voltage-Sensing Dyes by One- or Two-Photon Excitation near the Red Spectral Edge. *Biophysical Journal* **2004**, *87* (1), 631-639.
92. Fisher, J. A. N.; Salzberg, B. M.; Yodh, A. G., Near Infrared Two-Photon Excitation Cross-Sections of Voltage-Sensitive Dyes. *Journal of Neuroscience Methods* **2005**, *148* (1), 94-102.
93. Larson, D. R.; Zipfel, W. R.; Williams, R. M.; Clark, S. W.; Bruchez, M. P.; Wise, F. W.; Webb, W. W., Water-Soluble Quantum Dots for Multiphoton Fluorescence Imaging in Vivo. *Science (American Association for the Advancement of Science)* **2003**, *300* (5624), 1434-1436.
94. Zhang, M.; Bishop, B. P.; Thompson, N. L.; Hildahl, K.; Dang, B.; Mironchuk, O.; Chen, N.; Aoki, R.; Holmberg, V. C.; Nance, E., Quantum Dot Cellular Uptake and Toxicity in the Developing Brain: Implications for Use as Imaging Probes. *Nanoscale advances* **2019**, *1* (9), 3424-3442.
95. Rosenthal, S. J.; Chang, J. C.; Kovtun, O.; McBride, J. R.; Tomlinson, I. D., Biocompatible Quantum Dots for Biological Applications. *Chemistry & biology* **2011**, *18* (1), 10-24.

96. Breger, J.; Delehanty, J. B.; Medintz, I. L., Continuing Progress toward Controlled Intracellular Delivery of Semiconductor Quantum Dots. *Wiley Interdisciplinary Reviews: Nanomedicine and Nanobiotechnology* **2015**, 7 (2), 131-151.
97. Olivotto, M.; Arcangeli, A.; Carlà, M.; Wanke, E., Electric Fields at the Plasma Membrane Level: A Neglected Element in the Mechanisms of Cell Signalling. *BioEssays* **1996**, 18 (6), 495-504.
98. Park, K.; Kuo, Y.; Shvadchak, V.; Ingargiola, A.; Dai, X.; Hsiung, L.; Kim, W.; Zhou, Z. H.; Zou, P.; Levine Alex, J.; Li, J.; Weiss, S., Membrane Insertion of—and Membrane Potential Sensing by—Semiconductor Voltage Nanosensors: Feasibility Demonstration. *Science Advances* **2018**, 4 (1), e1601453.
99. Grupi, A.; Ashur, I.; Degani-Katzav, N.; Yudovich, S.; Shapira, Z.; Marzouq, A.; Morgenstein, L.; Mandel, Y.; Weiss, S., Interfacing the Cell with “Biomimetic Membrane Proteins”. *Small (Weinheim an der Bergstrasse, Germany)* **2019**, 15 (52), e1903006-n/a.
100. Park, J.; Werley, C. A.; Venkatachalam, V.; Kralj, J. M.; Dib-Hajj, S. D.; Waxman, S. G.; Cohen, A. E., Screening Fluorescent Voltage Indicators with Spontaneously Spiking Hek Cells. *PLoS One* **2013**, 8 (12), e85221.
101. Gopalakrishnan, G.; Danelon, C.; Izewska, P.; Prummer, M.; Bolinger, P.-Y.; Geissbühler, I.; Demurtas, D.; Dubochet, J.; Vogel, H., Multifunctional Lipid/Quantum Dot Hybrid Nanocontainers for Controlled Targeting of Live Cells. *Angewandte Chemie International Edition* **2006**, 45 (33), 5478-5483.
102. Wi, H. S.; Kim, S. J.; Lee, K.; Kim, S. M.; Yang, H. S.; Pak, H. K., Incorporation of Quantum Dots into the Lipid Bilayer of Giant Unilamellar Vesicles and Its Stability. *Colloids and surfaces, B, Biointerfaces* **2012**, 97, 37-42.
103. Lira, R. B.; Seabra, M. A. B. L.; Matos, A. L. L.; Vasconcelos, J. V.; Bezerra, D. P.; de Paula, E.; Santos, B. S.; Fontes, A., Studies on Intracellular Delivery of Carboxyl-Coated Cdte Quantum Dots Mediated by Fusogenic Liposomes. *Journal of materials chemistry. B, Materials for biology and medicine* **2013**, 1 (34), 4297-4305.

104. Zheng, W.; Liu, Y.; West, A.; Schuler, E. E.; Yehl, K.; Dyer, R. B.; Kindt, J. T.; Salaita, K., Quantum Dots Encapsulated within Phospholipid Membranes: Phase-Dependent Structure, Photostability, and Site-Selective Functionalization. *Journal of the American Chemical Society* **2014**, *136* (5), 1992-1999.
105. Qu, W.; Zuo, W.; Li, N.; Hou, Y.; Song, Z.; Gou, G.; Yang, J., Design of Multifunctional Liposome-Quantum Dot Hybrid Nanocarriers and Their Biomedical Application. *Journal of drug targeting* **2017**, *25* (8), 661-672.
106. Vargas, K. M.; Shon, Y.-S., Hybrid Lipid-Nanoparticle Complexes for Biomedical Applications. *Journal of materials chemistry. B, Materials for biology and medicine* **2019**, *7* (5), 695-78.
107. Ludwig, A.; Serna, P.; Morgenstein, L.; Yang, G.; Bar-Elli, O.; Ortiz, G.; Miller, E.; Oron, D.; Grupi, A.; Weiss, S.; Triller, A., Development of Lipid-Coated Semiconductor Nanosensors for Recording of Membrane Potential in Neurons. *ACS Photonics* **2020**, *7* (5), 1141-1152.
108. Park, J.; Kuo, Y.; Li, J.; Huang, Y.-L.; Miller, E. W.; Weiss, S., Improved Surface Functionalization and Characterization of Membrane-Targeted Semiconductor Voltage Nanosensors. *The Journal of Physical Chemistry Letters* **2019**, *10* (14), 3906-3913.
109. Acker, Corey D.; Yan, P.; Loew, Leslie M., Single-Voxel Recording of Voltage Transients in Dendritic Spines. *Biophysical Journal* **2011**, *101* (2), L11-L13.
110. Zhou, W.-L.; Yan, P.; Wuskell, J. P.; Loew, L. M.; Antic, S. D., Intracellular Long-Wavelength Voltage-Sensitive Dyes for Studying the Dynamics of Action Potentials in Axons and Thin Dendrites. *Journal of Neuroscience Methods* **2007**, *164* (2), 225-239.
111. Amanda, J. F.; Valeria, Z.; Dimitrii, T.; Eirini, P.; Valentina, E., Computer-Generated Holography Enhances Voltage Dye Fluorescence Discrimination in Adjacent Neuronal Structures. *Neurophotonics* **2015**, *2* (2), 1-8.
112. Milojkovic, B. A.; Wuskell, J. P.; Loew, L. M.; Antic, S. D., Initiation of Sodium Spikelets in Basal Dendrites of Neocortical Pyramidal Neurons. *The Journal of Membrane Biology* **2005**, *208* (2), 155-169.

113. Curtis, D. R., Microelectrophoresis. In *Electrophysiological Methods*, Elsevier: **1964**; pp 144-190.
114. Lalley, P. M., Microiontophoresis and Pressure Ejection. In *Modern Techniques in Neuroscience Research*, Springer: **1999**; pp 193-212.

CHAPTER 2 INTRACELLULAR DELIVERY OF QUANTUM DOTS VIA MICROELECTROPHORESIS TECHNIQUE

CONTENTS

2.1	Context	52
2.2	Publication 1.....	54

2.1 Context

Although microelectrophoresis has been successfully deployed for the intracellular delivery of VSDs, adapting this approach for the delivery of nanomaterials needs specific optimizations. Successful microelectrophoretic delivery requires that the substances to be ejected are highly charged to move along with the electrical current and are stable in intracellular solution without precipitation to block the micropipette tips. Intracellular solution filled in the micropipettes contains high concentration of potassium, sodium and chloride ions, with osmolarity and pH properly adjusted to mimic the ionic content of cells during intracellular or patch clamp recordings. In the case of VSDs, their solubility can be easily tuned via adding substituents (such as sulfonic acid groups), as long as their optical properties and voltage sensitivities are not affected. In addition, VSDs are usually less than 1 nm in size, even if they are precipitated into clusters, they are still much smaller compared to the micropipette tip sizes. In the case of VSM, their dispersibility is controlled by surface coatings to provide either electrostatic (charged groups), steric (macromolecules) stabilization or the combination of these two methods. The high ionic concentration of intracellular solution significantly lowers their repulsive energy barrier and leads to their irreversible aggregation. In addition, most nanomaterials are typically in the range of 5 to 10 nm, such as the rod-shaped QDs mentioned above. The aggregation of nanomaterials will cause subsequent blockages in the tip of micropipettes during ejection. Therefore, the optimizations of nanomaterials suspensions, micropipette tip size, current magnitude and ejection duration are needed for the successful microelectrophoretic delivery of nanomaterials. The following research questions will be investigated and answered in this chapter:

1. What are the challenges of performing intracellular delivery of nanomaterials with microelectrophoresis technique?
2. What are the requirements of preparing nanomaterials suspension?
3. What are the impacts of nanomaterials suspension on the intracellular recording quality?
4. What are the requirements of micropipette fabrication?

5. Can QDs be successfully delivered into live cells with all these requirements being satisfied?

The work in this chapter has been published as cover picture and will be presented in publication format.

2.2 Publication 1

Cytoplasmic delivery of quantum dots via microelectrophoresis technique

Mengke Han,^{1,2} Jiangbo Zhao,^{1,2} Joseph Mahandas Fabian,³ Samuel Evans,^{2,4}

Sanam Mustafa,^{2,4} Yinlan Ruan,^{1,2} Steven Wiederman,^{2,4} Heike Ebendorff-Heidepriem^{1,2}

¹School of Physical Sciences, Institute for Photonics and Advanced Sensing (IPAS), The University of Adelaide, Adelaide, Australia

²ARC Centre of Excellence for Nanoscale BioPhotonics (CNBP), The University of Adelaide, Adelaide, Australia

³Flinders Medical Centre, Flinders University, Adelaide, Australia


⁴Adelaide Medical School, The University of Adelaide, Adelaide, Australia

Published: Han, M., Zhao, J., Fabian, J.M., Evans, S., Mustafa, S., Ruan, Y., Wiederman, S. and Ebendorff-Heidepriem, H. (2021), Cytoplasmic delivery of quantum dots via microelectrophoresis technique. *ELECTROPHORESIS*, 42: 1247-1254.

Statement of Authorship

Title of Paper	Cytoplasmic delivery of quantum dots via microelectrophoresis technique
Publication Status	<input checked="" type="checkbox"/> Published <input type="checkbox"/> Accepted for Publication <input type="checkbox"/> Submitted for Publication <input type="checkbox"/> Unpublished and Unsubmitted work written in manuscript style
Publication Details	Han, M., Zhao, J., Fabian, J.M., Evans, S., Mustafa, S., Ruan, Y., Wiederman, S. and Ebendorff-Heidepriem, H. (2021), Cytoplasmic delivery of quantum dots via microelectrophoresis technique. ELECTROPHORESIS, 42: 1247-1254.


Principal Author


Name of Principal Author (Candidate)	Mengke Han		
Contribution to the Paper	Designed the project, performed the experiments of QDs suspension, micropipettes fabrication and intracellular delivery, interpreted all the data, and wrote the whole manuscript.		
Overall percentage (%)	80%		
Certification:	This paper reports on original research I conducted during the period of my Higher Degree by Research candidature and is not subject to any obligations or contractual agreements with a third party that would constrain its inclusion in this thesis. I am the primary author of this paper.		
Signature		Date	05/01/2022

Co-Author Contributions

By signing the Statement of Authorship, each author certifies that:

- i. the candidate's stated contribution to the publication is accurate (as detailed above);
- ii. permission is granted for the candidate to include the publication in the thesis; and
- iii. the sum of all co-author contributions is equal to 100% less the candidate's stated contribution.

Name of Co-Author	Jiangbo Zhao		
Contribution to the Paper	Contributed to the conception and design of the project and revised the manuscript.		
Signature		Date	13/01/2022

Name of Co-Author	Joseph Mahandas Fabian		
Contribution to the Paper	Performed the experiment of intracellular recording on dragonflies and interpreted the data.		
Signature		Date	18/01/2022

Name of Co-Author	Samuel Evans		
Contribution to the Paper	Performed the experiment of cell culture.		
Signature		Date	10/01/2022

Name of Co-Author	Sanam Mustafa		
Contribution to the Paper	Helped in the conception and design of the project and manuscript evaluation.		
Signature		Date	17/07/2022

Name of Co-Author	Yinlan Ruan		
Contribution to the Paper	Helped in the conception and design of the project and manuscript evaluation.		
Signature		Date	13/01/2022

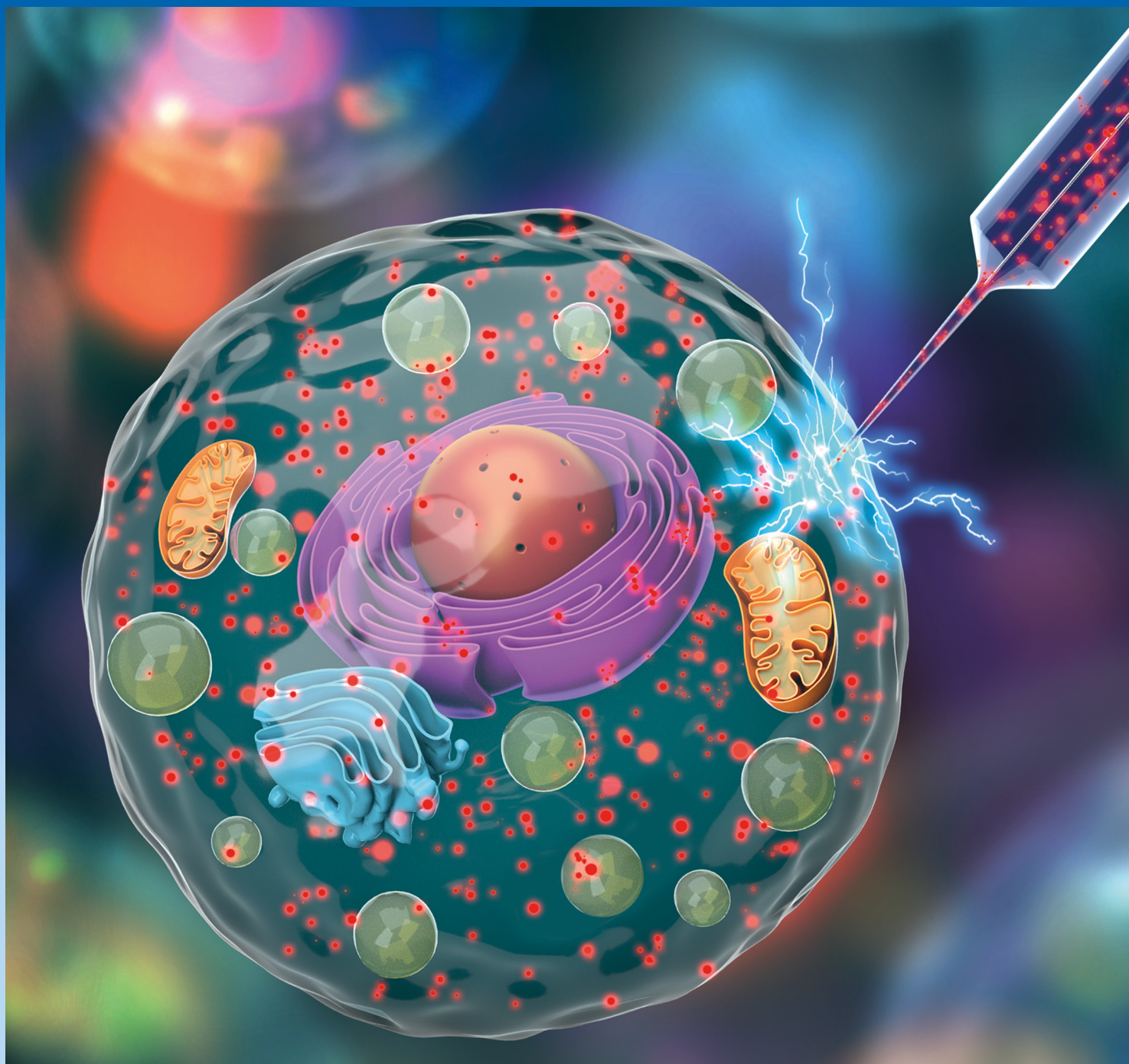
Name of Co-Author	Steven Wiederman		
Contribution to the Paper	Contributed to the conception and design of the project and revised the manuscript.		
Signature		Date	13/01/2022

Name of Co-Author	Heike Ebendorff-Heidepriem		
Contribution to the Paper	Helped in the conception and design of the project and contributed to structure and revise the manuscript.		
Signature		Date	13/01/2022

ELECTROPHORESIS

Electrokinetics  Fluidics  Proteomics

11  21



Mengke Han^{1,2} 
 Jiangbo Zhao^{1,2}
 Joseph Mahandas Fabian³
 Samuel Evans^{2,4}
 Sanam Mustafa^{2,4}
 Yinlan Ruan^{1,2}
 Steven Wiederman^{2,4}
 Heike
 Ebendorff-Heidepriem^{1,2}

¹School of Physical Sciences, Institute for Photonics and Advanced Sensing (IPAS), The University of Adelaide, Adelaide, Australia

²ARC Centre of Excellence for Nanoscale BioPhotonics (CNBP), The University of Adelaide, Adelaide, Australia

³Flinders Medical Centre, Flinders University, Adelaide, Australia

⁴Adelaide Medical School, The University of Adelaide, Adelaide, Australia

Received December 28, 2020

Accepted February 17, 2021

Research Article

Cytoplasmic delivery of quantum dots via microelectrophoresis technique

Nanoparticles with specific properties and functions have been developed for various biomedical research applications, such as *in vivo* and *in vitro* sensors, imaging agents and delivery vehicles of therapeutics. The development of an effective delivery method of nanoparticles into the intracellular environment is challenging and success in this endeavor would be beneficial to many biological studies. Here, the well-established microelectrophoresis technique was applied for the first time to deliver nanoparticles into living cells. An optimal protocol was explored to prepare semiconductive quantum dots suspensions having high monodispersity with average hydrodynamic diameter of 13.2–35.0 nm. Micropipettes were fabricated to have inner tip diameters of approximately 200 nm that are larger than quantum dots for ejection but less than 500 nm to minimize damage to the cell membrane. We demonstrated the successful delivery of quantum dots via small electrical currents (–0.2 nA) through micropipettes into the cytoplasm of living human embryonic kidney cells (roughly 20–30 μm in length) using microelectrophoresis technique. This method is promising as a simple and general strategy for delivering a variety of nanoparticles into the cellular environment.

Keywords:

Biosensor / Intracellular delivery / Microelectrophoresis / Nanoparticles / Quantum dots
 DOI 10.1002/elps.202000388

1 Introduction

The intracellular delivery of exogenous materials with high efficiency and specificity has shown great promise in deciphering and even modulating the complex, spatiotemporal interplay of biomolecules within living cells [1,2]. As a powerful technique widely applied in modern biology, microelectrophoresis uses electrical currents to eject charged substances through fine-tipped glass micropipettes into living cells [3]. Microelectrophoresis performs intracellular delivery in a highly controlled manner. It can limit the problematic diffusion of chemically and pharmacologically active substances from micropipettes, by simply applying a retaining current [3], which can reduce cell distortion and damage. In addition, as most biological membranes *in vivo* maintain resting membrane potential differences ranging from –30 to –180 mV [4], microelectrophoresis can readily locate target cells deep in tissue slice or living animals. Once the micropipette is pierced into the cytosol of target cell, it can measure intracellular electrical activity in real time [5].

Correspondence: Professor Heike Ebendorff-Heidepriem, School of Physical Sciences, Institute for Photonics and Advanced Sensing, The University of Adelaide, Adelaide, South Australia 5005, Australia

E-mail: heike.ebendorff@adelaide.edu.au

Abbreviations: **BSTMD**, binocular small target motion detector; **DLS**, dynamic light scattering; **HEK**, human embryonic kidney; **ID**, inner diameter; **OD**, outer diameter; **QDs**, quantum dots; **TEM**, transmission electron microscope

Although microelectrophoresis has been established since *circa* 1900 [6], no studies have been conducted to explore the intracellular microelectrophoretic delivery of nanoparticles, despite the rapid development of utilizing nanomaterials in various intracellular biological research and medical applications [2]. For example, fluorescent semiconductive quantum dots (QDs) with superior optical properties and surface groups permit real-time tracking of intracellular molecules over time scales of milliseconds to hours, offering a capability to monitor intracellular events that cannot be accomplished via organic fluorophores. The main challenge confronting microelectrophoretic delivery of nanoparticles is the possibility of nanoparticle aggregation in the tip of micropipettes during ejection, which can cause tip blockage and failed delivery. The reasons are twofold.

First, traditionally used silver/silver chloride (Ag/AgCl) electrodes in microelectrophoresis only conduct well (transform the flow of electrons from the current source to a flow of ions in solution) in solutions that contain substantial Cl^- ions [7]. Accordingly, target cells can be located and subsequently their intracellular electrical activity recorded with high signal to noise ratio and wide recording bandwidth (only for electrically excitable cells, i.e., neurons, muscle cells, and some endocrine cells). Therefore, potassium chloride (KCl) solution with concentration of 0.2–2 M is typically used to dissolve charged substances to be ejected [3,5]. The concentration of KCl should be as high as possible for low-noise

Color online: See article online to view Figs. 1 and 4 in color.

intracellular recording while considering the solubility of different substances. For nanoparticles, high KCl concentration significantly lowers their repulsive energy barrier, that is, zeta potential at their hydrodynamic diameters, which leads to the irreversible aggregation of nanoparticles [8]. This can cause blockages in the tip of micropipettes during ejection and thus failed microelectrophoresis.

Second, to impale cells with minimal damage, a rule of thumb is that the outer diameter (OD) near the tip of micropipettes should be less than 500 nm [3]. However, the inner diameter (ID) near the tip must be large enough to allow the ejection of nanoparticles having comparable hydrodynamic diameters. Tips that are too small will impede the ejection and subsequently cause the aggregation of nanoparticles in the tips, leading to failed microelectrophoresis.

In this paper, we addressed these technical hurdles by preparing optimal nanoparticle suspensions with a low KCl concentration and high pH to reach a compromise between the colloidal stability of nanoparticles for ejection and high-fidelity intracellular recording. In addition, we fabricated micropipettes having appropriate tip sizes to allow the intracellular delivery of nanoparticles into living cells with suitable ejecting current and duration. These results suggest the future potential of microelectrophoresis as a simple and precise approach in the intracellular delivery of various nanoparticles into the cellular environment.

2 Materials and methods

2.1 QDs suspension preparation and colloidal stability measurement

CdSe/ZnS core/shell structured QDs (emission maxima of 655 nm) with amine-derivatized PEG surface functional group (Q21521MP; Invitrogen), hereafter referred to as 655-QDs, were used to demonstrate intracellular microelectrophoresis. The KCl concentration and pH was adjusted by gradually adding 2 M KCl, 0.1 M hydrochloric acid (HCl), or 0.1 M sodium hydroxide (NaOH) into QDs suspension in fresh ultrapure water (concentration of QDs was consistently 10 nM). KCl, HCl, and NaOH solutions were centrifuged at 4000 revolutions per minute (rpm) for 1 min before the addition to remove any large-size impurities that can affect measurement results. Zetasizer nano ZSP (Malvern Instruments) was used for the studies on the colloidal stability of 655-QDs as it can measure both the hydrodynamic size of the nanoparticles via dynamic light scattering (DLS) and the zeta potential via laser Doppler electrophoresis in aqueous media [9]. For the Zetasizer measurements, the Henry's function was set at the value of 1.50 [10]. The dispersant was set to be water (temperature: 25.0 °C; viscosity: 0.8872 cP; refractive index: 1.330; dielectric constant: 78.5), and its viscosity was used as the viscosity of the sample. The refractive index and absorption of 655-QDs were set as 2.550 and 0.010 [11].

Table 1. The parameters of pulling program 1 and 2 in P-97 puller

Program		1	2	
Ramp		518	518	
Pressure		510	510	
Cycle	1	Heat	513	513
		Pull	0	0
		Velocity	8	8
	2	Time	1	1
		Heat	508	440
		Pull	100	100
	Velocity	65	65	
	Time	100	100	

2.2 Intracellular recording quality test

To determine if the low KCl concentration that is necessary for maintaining the colloidal stability of nanoparticles can permit high-fidelity intracellular recording, we compared the quality of intracellular recordings acquired from dragonflies using standard 2 M KCl, 0.01 M KCl, and optimized 655-QDs suspension. With their large head capsule and ease of dissection, dragonflies are an ideal model system for recording *in vivo*, intracellular activity. Wild-caught dragonflies (*Hemicordulia tau*) were immobilized with a mixture of beeswax and gum rosin (solid form of resin) (1:1) on a plastic articulating stage (as shown later in Fig. 2A). To gain the access to the brain surface, a small hole was dissected on the posterior surface of the head capsule. A working Ag/AgCl electrode (782500; A-M Systems) was connected to an intracellular bridge mode amplifier (BA-03X; npi electronic), and a counter Ag/AgCl electrode was inserted into the head capsule surface to form a complete electrical circuit. Using a pipette holder (PPH-1P-BNC; ALA Scientific Instruments) and a micromanipulator (MM-33; ALA Scientific Instruments), extremely fine-tipped glass micropipettes (pulled by program 1 in Table 1) were pierced into single lobula neurons. Neurons were stimulated by drifting small moving visual features across a high refresh rate (165 Hz) liquid crystal display monitor placed directly in front of the dragonfly. Data were digitized at 5 kHz with a 16-bit analog-to-digital converter and analyzed off-line with MATLAB. The visual stimulus elicited voltage changes across the cell membranes and the digitized data indicated successful intracellular neuronal recordings in real time.

2.3 Micropipette fabrication

P-97 Flaming/Brown type pipette puller (Sutter Instrument) was used to fabricate micropipettes from aluminosilicate glass capillaries (30-0108; Harvard Apparatus). The pulling programs are listed in Table 1. Micropipettes pulled by program 1 were used for intracellular recording on dragonflies. Micropipettes pulled by program 2 were used for microelectrophoresis of QDs. To measure the tip IDs and ODs with

high accuracy, fabricated micropipettes were coated with a 3-nm-thick platinum film and fixed in two different orientations onto scanning electron microscope stubs: either vertically for tip IDs or horizontally for tip ODs measurement under a FEI Quanta 450 FEG environmental scanning electron microscope. Thus, it was not possible to measure both the ID and the OD for the same micropipette tip.

2.4 Microelectrophoresis

Human embryonic kidney (HEK293) cells were seeded at 80 000 cells/dish onto a low-wall 35 mm imaging dish (80156; ibidi) and cultured (37°C in a humidified incubator at 5% CO₂) for 2 days in 1 mL DMEM supplemented with 2 mM L-glutamine and 10% fetal bovine serum. During electrophoresis, the media was changed to 2 mL DMEM supplemented with 25 mM HEPES (21063045; Thermo fisher) to maintain physiological pH in atmosphere at room temperature. HEK293 cells (60–70% confluency) were visualized with 40× water immersion objective of a Nikon Ti-E inverted microscope equipped with cage incubator (Okolab) (the setup is shown later in Fig. 4A). A stored aliquot of optimized QDs suspension was vortexed for 1 min and sonicated from 4°C to 24°C without the use of external heat for 30 min to fully disperse QDs. The QDs suspension was carefully backfilled into micropipettes via a flexible plastic needle (Warner instruments). The micropipette was inserted with an Ag/AgCl working electrode from the blunt end and was held by a micromanipulator (Sensapex) to slowly move toward a single cell at a 50° angle. Another Ag/AgCl counter electrode was carefully placed into the media. The two electrodes were connected to the headstage of the intracellular bridge mode amplifier (BX-01; npi) to form a complete electrical circuit. A change in potential difference around –20 to –40 mV indicated that the tip of micropipette was successfully pierced through the cell membrane into the cytoplasm of the cell. A small current of –0.2 nA was then applied to eject QDs into the cell for 3 min.

3 Results

3.1 Optimization of QDs suspension

The impact of KCl concentration on the colloidal stability of 655-QDs was investigated using particle size distribution (DLS technique) and zeta potential measurements. DLS measures the time-dependent fluctuation of scattered light intensity caused by the constant Brownian motion of particles, and reports their hydrodynamic diameters as the equivalent hydrodynamic diameters (D_H) of spheres that have the same average diffusion coefficient [12]. An established criterion for monodispersed nanoparticles is that their hydrodynamic diameters (D_H) should be less than twice of their diameters in the dry state (D_T) measured by transmission electron microscope (TEM) [13]. Figure 1A shows the image of 655-QDs

(dark dots) on the surface of a TEM grid. The average shape of 655-QDs was modeled as a prolate ellipsoid with the major axis (a_T) of 9.7 ± 1.6 nm and the minor axis (b_T) of 6.7 ± 0.8 nm (± 1 SD, $n = 82$) rather than ideal spheres. Therefore, as per the criterion for nanoparticle monodispersity in aqueous environment, monodispersed 655-QDs should theoretically have major hydrodynamic axes (a_H) in the range of 8.1–22.6 nm and minor hydrodynamic axes (b_H) in the range of 5.9–15.0 nm. To examine the monodispersity of elliptical 655-QDs based on the spherical hydrodynamic diameters reported by DLS technique, the following equation regarding the diffusion properties of anisotropic particles in Brownian motion [14] was used to translate the ellipsoidal dimensions (a_H and b_H) of 655-QDs to an equivalent diameter (D_H) of spheres having the same diffusion coefficient:

$$D_H = 2 \times \frac{(a_H^2 - b_H^2)^{1/2}}{\ln \left(\frac{a_H + (a_H^2 - b_H^2)^{1/2}}{b_H} \right)}$$

In view of the range of a_H and b_H dimensions, monodispersed 655-QDs were considered to have hydrodynamic diameters D_H over 13.2 nm and less than 35.0 nm.

Figure 1B compares the scattered light intensity of particles across a range of sizes in 0.01 M and 2 M KCl solutions. The dotted lines indicate the size range of monodispersed 655-QDs from 13.2 to 35.0 nm. In 2 M KCl, QDs completely aggregated with a mean size around 1.5 μ m due to the strong electrostatic screening effect caused by the high electrolyte concentration [8]. In 0.01 M KCl, only 59.2% of the scattered light came from QDs aggregates or artifacts (e.g., dust). Scattered light intensity is proportional to the sixth power of the particle radius and therefore the intensity-based size distribution is highly sensitive to very small numbers of aggregates or dust [15]. Thus, the number of QDs aggregates in 0.01 M KCl was negligible compared to the total number of particles in the sample (determined using Mie theory, as shown in Fig. 1C) [15]. Since the intensity-based size distribution is more reliable than number distribution, Fig. 1D (red line) shows the change in the fraction of light intensity scattered by monodispersed 655-QDs (i.e., portion of single QDs) with increasing KCl concentration. It sharply decreased from 40.8% in 0.01 M KCl to 7.5% in 0.1 M KCl. Note that there are no data on ultrapure water since the thickness of the electrical double layer of all particles is considered to be about 1 μ m [16], making nanoscale particle size distribution measurement in solution via DLS impossible.

The negative effect of KCl on the colloidal stability of 655-QDs revealed by DLS was also evidenced by zeta potential measurements. 655-QDs exhibited negative surface charge in ultrapure water, that is, 0 M KCl, leading to an average zeta potential of –29.9 mV (as shown in Fig. 1D, blue line). With increasing KCl concentration, the zeta potential (colloidal stability of 655-QDs) rapidly approached zero due to the stronger electrostatic screening effect [8]. The zeta potential of –29.9 mV for 0 M KCl agrees with a previous report on

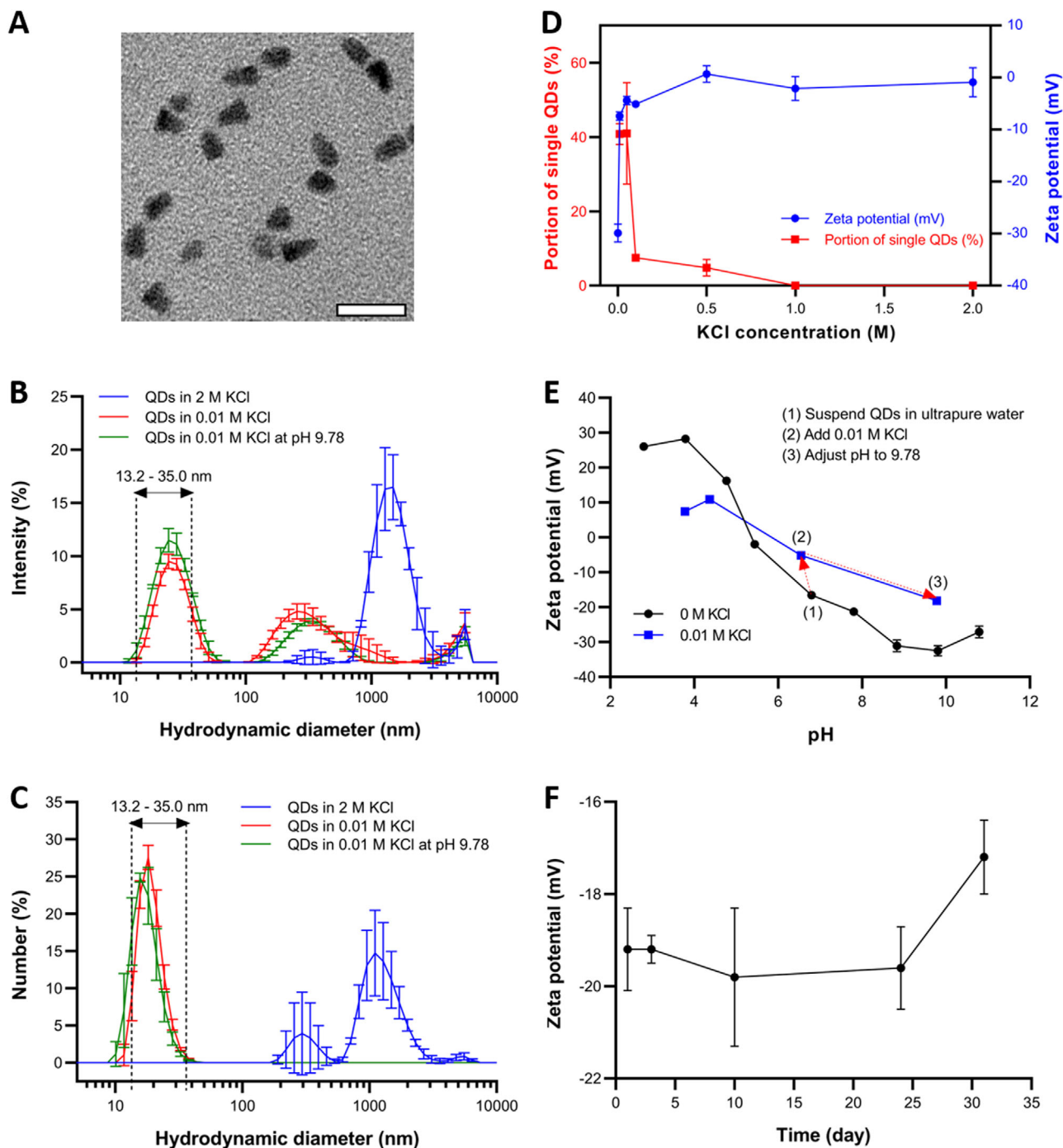


Figure 1. (A) TEM image of 655-QDs reveals an average shape of prolate ellipsoid with a major axis (a_T) of 9.7 ± 1.6 nm and a minor axis (b_T) of 6.7 ± 0.8 nm (± 1 SD with $n = 82$). Scale bar, 25 nm. (B) The size distribution by intensity and (C) by number of 655-QDs in 2 M KCl (pH 5.21), 0.01 M (pH 6.55) and optimized suspensions (0.01 M KCl adjusted to pH 9.78). Each data point comprises 12 repeat measurements of three independent samples (error bars, ± 1 SD with $n = 3$). The dot lines indicate the size range of monodispersed 655-QDs from 13.2 to 35.0 nm. (D) The zeta potential of 655-QDs and the portion of single QDs (determined as fraction of light intensity scattered by monodispersed 655-QDs) as a function of KCl concentration. Error bars, ± 1 SD with $n = 3$. (E) The zeta potential of 655-QDs in ultrapure water and 0.01 M KCl solution with different pH values. Error bars, ± 1 SD with $n = 3$. Inserted with each step of the optimal preparation process of 655-QDs suspension for microelectrophoresis. (F) The stability of 655-QDs zeta potential in optimized suspension. Error bars, ± 1 SD with $n = 3$.

the zeta potential of gold nanoparticles that are also surface-functionalized with amine-derivatized PEG [17].

The measurements of the zeta potential and size distribution of 655-QDs in different KCl solutions (Fig. 1D) show that a KCl concentration as low as 0.01 M is most suitable for achieving high zeta potential (absolute value), which is essential to maintain colloidal stability. However, the zeta potential of -7.4 mV for 655-QDs in 0.01 M KCl solution is still not sufficiently high (absolute value) considering that particles with zeta potential more positive than 30 mV or more negative than -30 mV are generally considered to represent sufficient repulsion to maintain their colloidal stability [9]. Thus, we investigated the effect of pH adjustment on the zeta potential of 655-QDs and evaluated its capability to further stabilize 655-QDs.

We commenced with testing impact of pH for QDs suspended in ultrapure water, that is, 0 M KCl (Fig. 1E, black line). The as-prepared QD suspension (without pH adjustment) had a pH of ~ 7 and a zeta potential of -16.6 mV. Note that this zeta potential value (-16.6 mV) was different to that of the QD suspension in ultrapure water used for the study of the impact of KCl concentration (-29.9 mV). This difference was attributed to the large uncertainty of zeta potential measurements in ultrapure water due to low conductivity. The increase of the pH by addition of alkali (NaOH) resulted in a more negative charge for 655-QDs particles (decreased zeta potential). Conversely, the decrease of the pH by addition of acid (HCl) increased the zeta potential. The most stable state of 655-QDs was achieved by adjusting the pH of QDs suspension to 9.81, where the maximal zeta potential (absolute value) of -32.5 mV was obtained.

Next, we investigated the impact of pH for QDs suspended in 0.01 M KCl solution (Fig. 1E, blue line). Without pH adjustment, the QD suspension had a zeta potential of -5.2 mV and a pH of 6.55. For lower pH of 3.78 and 4.37, the zeta potential increased to $+7.4$ and $+10.9$ mV, respectively. For higher pH of 9.78, the zeta potential decreased to -18.2 mV. These results show that both lower and higher pH can enhance the absolute value of the zeta potential and thus the colloidal stability compared to the QD suspension without pH adjustment. Thus, pH adjustment can effectively buffer the negative effect of 0.01 M KCl on the stability of 655-QDs.

Although a stable state of 655-QDs also exists at acid pH, a strong acid environment ($\text{pH} < 4$) is not recommended by the supplier, as the polymer coating can dissociate, exposing and dissolving the core/shell structure. In addition, due to the high mobility of hydrogen ions (H^+), a large amount of H^+ in microelectrophoresis can result in lowering of the pH in the vicinity of the tip of micropipettes [18]. This localized change in pH has been proposed to excite the cell undergoing intracellular recording and interfere with the normal physiological state [19]. On the contrary, 655-QDs do not degrade in a strong basic environment ($\text{pH} > 9$) as noted by the supplier. Furthermore, in comparison to the electrophoretic mobility of H^+ ($36.25 \mu\text{mcm/Vs}$ in water at 25.0°C), hydroxide ion (OH^-) has a lower electrophoretic mobility ($20.50 \mu\text{m cm/Vs}$

in water at 25.0°C), resulting in less effect on the intracellular activity [20].

Based on the investigation of KCl concentration and pH adjustment on the colloidal stability of QDs, we established the following optimal protocol for the preparation of QDs suspension for microelectrophoresis. The method is to initially dilute QDs stock solution with fresh ultrapure water to 10 nM and then gradually add 2 M KCl to the suspension until a final KCl concentration of 0.01 M achieved. Finally, the pH is adjusted to 9.78 by gradually adding freshly prepared 0.1 M NaOH to further stabilize QDs (indicated by dashed red lines with arrow in Fig. 1E). The green curve in Fig. 1B shows the size distribution of optimized 655-QDs suspension, where 53.9% of scattered light comes from monodispersed QDs that constitute 91.4% of the total number of particles in the sample as shown in Fig. 1C.

For practical microelectrophoresis applications, preparation of fresh suspensions would be too time consuming. A stock suspension with good colloidal stability and ready for use would be highly beneficial. Figure 1F shows the shelf life of optimized 655-QDs suspensions (0.01 M KCl at pH 9.78). They were aliquoted and stored at 4.0°C in dark. The zeta potential values of QDs in these intact aliquots were measured on different days, which remained the same for at least 24 days, indicative of this beneficial, long-term colloidal stability.

3.2 The effect of KCl concentration on the quality of intracellular recording

The highest KCl concentration suitable to maintain colloidal stability of QDs was determined to be 0.01 M, which raised the problem whether such a low electrolyte concentration and the existence of 655-QDs in optimized suspensions allow for the recording of intracellular activity with sufficiently high fidelity in real time. Thus, we compared the quality of intracellular recordings acquired by 2 M KCl solution (used in standard dragonfly electrophysiology) with those of 0.01 M KCl solution and optimized 655-QDs suspension (0.01 M KCl at pH 9.78). The intracellular recordings were captured from visual neurons, binocular small target motion detector (BSTMD2), in the optic lobes of living dragonflies [21]. When BSTMD2 is presented with a small drifting target, the cell responds by significantly increasing the frequency of action potential firing.

Figure 2B shows the typical raw responses (left panel) and an enlarged view of individual spike waveforms (right panel) recorded by 2 M KCl, 0.01 M KCl, and optimized 655-QDs suspension from BSTMD2 cells ($n = 6$) presented with a small moving target. The average tip resistance for micropipettes filled with 2 M KCl, 0.01 M KCl, and optimized 655-QDs suspension was 120, 335, and 300 $\text{M}\Omega$, respectively. Although the recordings acquired by using low KCl concentration (0.01 M KCl without QDs and optimized 655-QDs suspension) had a greater degree of variation in quality (i.e., noise and signal amplitude) than the recordings acquired

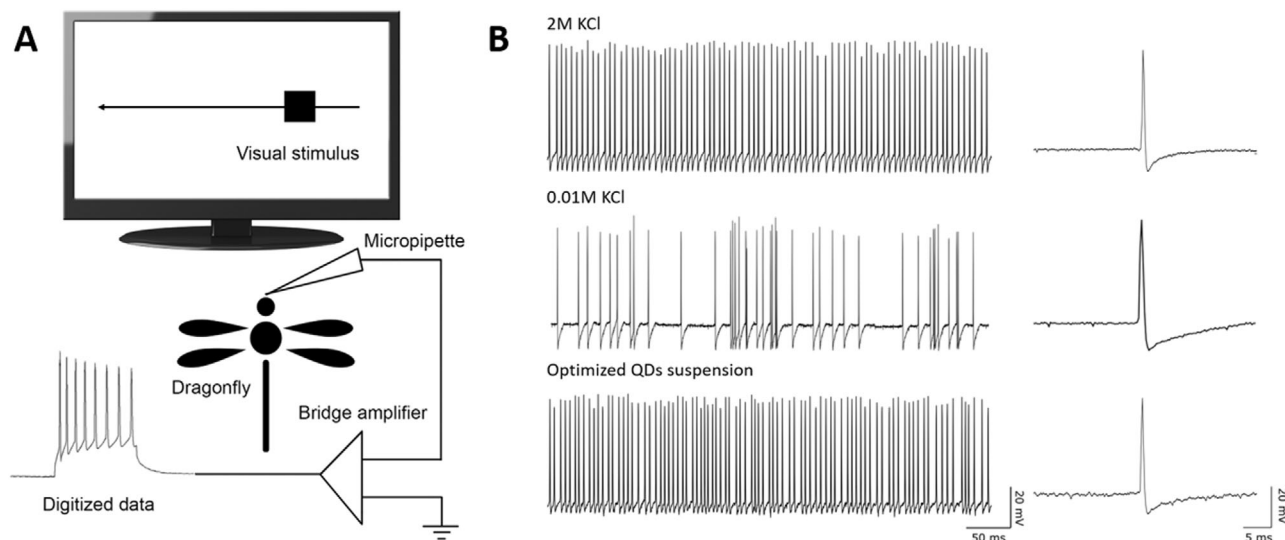


Figure 2. (A) Schematic illustration of the experiment setup for intracellular recording of dragonflies. A liquid crystal display (LCD) monitor was placed in front of the dragonfly for stimulating visual neurons by drifting small moving objects. The visual stimulus elicited voltage changes across the cell membranes of single lobula neurons, which were recorded in real time. (B) The responses of two BSTMD2 cells in two separate dragonflies to the presentation of a drifting object, which were recorded with micropipettes filled with 2 M KCl solution, 0.01 M KCl solution, and optimized 655-QDs suspension (0.01 M KCl at pH 9.78).

by 2 M KCl, it was possible to count spikes that were distinct from the resting potential without any issue in temporal responsiveness. In addition, spiking responses and individual action potential waveforms remained very similar for all cases.

As a conclusion, KCl concentration of 0.01 M and the existence of 655-QDs in suspensions can precisely locate target cells, and then produce high-fidelity intracellular recordings.

3.3 Optimizing the tip size of micropipette for intracellular delivery

For successful microelectrophoresis, the tip ID of the micropipette is required to be larger than the sum of hydrodynamic diameters of nanoparticles and other dissolved ions that pass through the tip for conductivity. The range of hydrodynamic diameter of monodispersed 655-QDs is 13.2–35.0 nm. The theoretical hydrated diameters of K^+ , Cl^- , and Na^+ ions are 0.3, 0.4, and 0.2 nm, respectively [22]. Considering the unavoidable trace amount of QDs aggregates or artifacts (e.g., dust) existing in the optimized QDs suspension (Fig. 1B), the tip ID of the micropipette should be as large as possible to eliminate tip blockage. However, as proposed by previous studies, the tip OD should be less than 500 nm to avoid physical damage to living cells [3]. To achieve small tip OD yet large enough tip ID, we chose aluminosilicate glass for the fabrication of micropipettes since a unique characteristic of aluminosilicate micropipettes is that the ratio of their ID to OD increases remarkably toward the tip [23]. Thus, they have extremely thin wall near the tip, which provides the smallest possible tip OD to avoid physical damage to cells.

The pulling program 1 listed in Table 1 was designed to fabricate micropipettes with tip ID of ca. 100 nm in previous studies of standard dragonfly electrophysiology [24]. To achieve larger tip ID suitable for QDs ejection, we reduced the heat value in the second cycle from 508 in program 1 to 440 in program 2. Figure 3 shows the SEM images of aluminosilicate micropipettes pulled by program 2 in front and side views. The average tip OD of 26 fabricated micropipettes was 202 nm with a tolerance of ± 35 nm (± 1 SD). The average tip ID of another 26 micropipettes was 206 nm with a larger tolerance of ± 46 nm (± 1 SD). These two averages were nearly identical, which validated the unique characteristics of aluminosilicate micropipettes. Their extremely thin wall near the tip made the tip OD as small as possible to minimize the physical damage to cell membrane while having large enough tip ID for the ejection. The average tip ID of approximately 200 nm was the maximum achievable size by lowering the heat value in the second cycle. For lower heat values, the aluminosilicate capillaries did not soften sufficiently to form micropipettes. The variance was in part caused by the observational error due to the inconsistency of pipette angle when manually fixing micropipettes onto the vertical SEM sample holder. In addition, when pulling micropipettes, capillaries with slightly different IDs (0.52 ± 0.03 mm, ± 1 SD, $n = 26$) and ODs (0.99 ± 0.02 mm, ± 1 SD, $n = 26$) had different distances to the box heating filament and different volume of air enclosed in the internal channel, which altered the glass temperature and resulted in variations in tip ID and OD of micropipettes [25].

In summary, the range of tip IDs of our aluminosilicate micropipettes is suitable for the ejection of 655-QDs and the tip ODs are less than 500 nm to avoid physical damage to cells as proposed by previous studies [3].

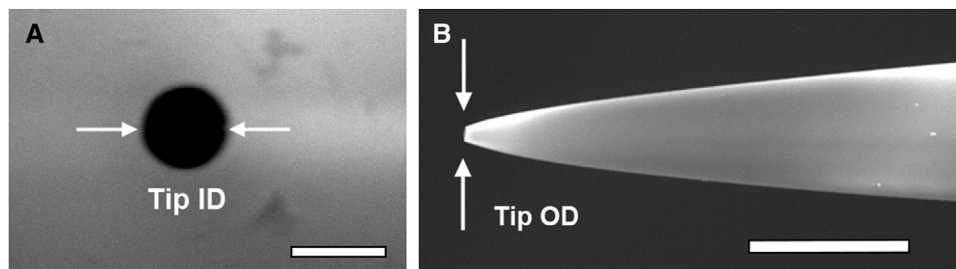


Figure 3. (A) High-resolution SEM image of a micropipette for microelectrophoresis of 655-QDs with a tip ID of 211 nm (front view). The orifice of micropipette is the black circle near the center of the image. Scale bar, 250 nm. (B) High-resolution SEM image of another micropipette (pulled with program 2) with a tip OD of 212 nm (side view). Scale bar, 2.5 μm .

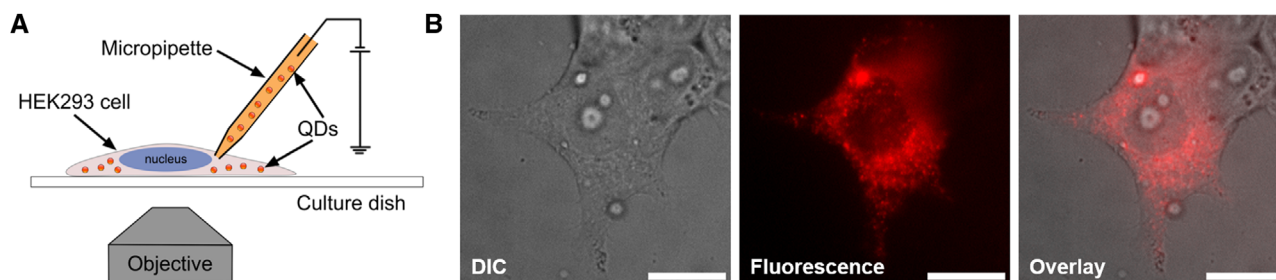


Figure 4. (A) Diagram of microelectrophoresis of 655-QDs into HEK293 cells. (B) Differential interference contrast (DIC), fluorescence, and overlay images of a HEK293 cell with microelectrophoretically-delivered 655-QDs. The red dots in the cytoplasm are 655-QDs. Scale bar, 10 μm .

3.4 Successful cytoplasmic delivery of QDs into living cells via microelectrophoresis

Figure 4B shows the differential interference contrast, and fluorescent and overlay images of the typical results after microelectrophoresis delivery of 655-QDs into HEK cells ($n = 20$). QDs evenly dispersed throughout the cytoplasm without entering the nucleus. During microelectrophoresis, the resistance of micropipettes was frequently measured to confirm that there was no blockage or breakage in the tips. The resistance of several micropipettes varied from 50 to 80 M Ω due to the variation in their tip sizes and remained the same when removed out of the cells after delivery, which indicated that there was no tip blockage or breakage happened during microelectrophoresis.

4 Concluding remarks

We demonstrated for the first time the use of the well-established microelectrophoresis technique for the successful delivery of nanoparticles, such as QDs used here, into the cytoplasm of living cells. This was achieved by overcoming the following two critical challenges. First, we prepared QDs suspensions with low KCl concentration and high pH value, which maintained high QDs colloidal stability to prevent aggregation and blockages in the tip of micropipettes during ejection, while being able to record the intracellular electrical activity of dragonfly neurons with high fidelity. Second, we fabricated micropipettes with inner tip diameters of approximately 200 nm, which was large enough to allow

the ejection of QDs and less than 500 nm to avoid physical damage to HEK293 cells as proposed by previous studies [3]. This successful microelectrophoretic ejection of QDs lays the foundation for further studies and applications of microelectrophoresis technique for the intracellular delivery of various nanoparticles.

This work was performed in part at the Optofab node of the Australian National Fabrication Facility (ANFF) utilizing Commonwealth and SA State Government funding. The authors acknowledge partial support from the Australian Research Council Centre of Excellence for Nanoscale BioPhotonics (CNBP) (CE140100003) and Discovery Early Career Researcher Award (DECRA) from Australian Research Council (ARC) (DE150100548). M.H. thanks K. Neubauer, A. Slattery, and J. Sibbons for their assistance in SEM, TEM, and live cell microscopy at Adelaide Microscopy.

The authors have declared no conflict of interest.

DATA AVAILABILITY STATEMENT

The data that support the findings of this study are available from the corresponding author upon reasonable request.

5 References

- [1] Stewart, M. P., Sharei, A., Ding, X., Sahay, G., Langer, R., Jensen, K. F., *Nature* 2016, 538, 183–192.

- [2] Chou, L. Y., Ming, K., Chan, W. C., *Chem. Soc. Rev.* 2011, 40, 233–245.
- [3] Curtis, D. R., *Microelectrophoresis*, Academic Press, New York 1964.
- [4] Tekle, E., Astumian, R. D., Chock, P. B., *Biochem. Biophys. Res. Commun.* 1990, 172, 282–287.
- [5] Mobbs, P., Becker, D., Williamson, R., Bate, M., Warner, A., in: Ogden, D. C. (Ed.), *Microelectrode Techniques: The Plymouth Workshop Handbook*, Company of Biologists, Cambridge, UK 1994, pp. 361–387.
- [6] Lalley, P. M., in: Windhorst, U., Johansson H. (Eds.), *Modern Techniques in Neuroscience Research*, Springer, Berlin 1999, pp. 193–212.
- [7] Axon Instruments, *The Axon Guide for Electrophysiology and Biophysics Laboratory Techniques*, Axon Instruments, Foster City, CA 1993.
- [8] Zhang, W., in: Capco, D. G., Chen, Y. (Eds.), *Nanomaterial: Advances in Experimental Medicine and Biology*, Springer, Dordrecht 2014, pp. 19–43.
- [9] Clogston, J. D., Patri, A. K., in: McNeil S.E. (Ed.), *Characterization of Nanoparticles Intended for Drug Delivery*, Humana Press, Totowa, NJ 2011, pp. 63–70.
- [10] Henry, D., *Proc. R. Soc. Lond. Ser. A* 1931, 133, 106–129.
- [11] Hondow, N., Brydson, R., Wang, P., Holton, M. D., Brown, M. R., Rees, P., Summers, H. D., Brown, A., *J. Nanopart. Res.* 2012, 14, 1–15.
- [12] Pecora, R., *Dynamic Light Scattering: Applications of Photon Correlation Spectroscopy*, Springer Science & Business Media, New York 2013.
- [13] Moon, J., Choi, K.-S., Kim, B., Yoon, K.-H., Seong, T.-Y., Woo, K., *J. Phys. Chem. C* 2009, 113, 7114–7119.
- [14] Perrin, F., *J. Phys. Radium* 1936, 7, 1–11.
- [15] Mie, G., *Ann. Phys. (Berlin, Ger.)* 1908, 330, 377–445.
- [16] Israelachvili, J. N., *Intermolecular and Surface Forces*, Academic Press, London 2011.
- [17] Xia, X., Yang, M., Wang, Y., Zheng, Y., Li, Q., Chen, J., Xia, Y., *ACS Nano* 2012, 6, 512–522.
- [18] Gruol, D. L., Barker, J. L., Huang, L. Y., MacDonald, J. F., Smith, T. G., Jr., *Brain Res.* 1980, 183, 247–252.
- [19] Frederickson, R. C., Jordan, L. M., Phillis, J. W., *Brain Res.* 1971, 35, 556–560.
- [20] Duso, A. B., Chen, D. D. Y., *Anal. Chem.* 2002, 74, 2938–2942.
- [21] O'Carroll, D., *Nature* 1993, 362, 541–543.
- [22] Marcus, Y., *Chem. Rev.* 1988, 88, 1475–1498.
- [23] Sutter Instrument, P-97 Pipette Cookbook, Sutter Instrument, Novato, CA 2008.
- [24] O'Carroll, D. C., *Proc. SPIE Electron. Struct. MEMS II* 2001, 4591, 1–11. <https://doi.org/10.1117/12.449135>
- [25] Chen, M. J., Stokes, Y. M., Buchak, P., Crowdy, D. G., Foo, H. T., Dowler, A., Ebendorff-Heidepriem, H., *Opt. Mater. Express* 2016, 6, 166–180.

CHAPTER 3 INTRACELLULAR FATE OF MICROELECTROPHORETIC DELIVERED QUANTUM DOTS

CONTENTS

3.1	Context	68
3.2	Publication 2.....	69
3.3	Supporting information	81
3.4	Intracellular delivery of quantum dots into SH-SY5Y cells	86
3.5	References	88

3.1 Context

The work presented in Publication I provides an optimal protocol to prepare QDs suspension that meets the requirements of high surface charge, colloidal stability, and intracellular recording quality. QDs were successfully delivered into live HEK293 cells via small electrical current of -0.2 nA for 3 mins. The micropipette tip size of 200 nm was proven to be large enough for the ejection of QDs. These results demonstrated that microelectrophoresis is an effective method for the intracellular delivery of nanomaterials. The next step is to further explore the intracellular fate of these delivered QDs and their impact on the cell health. In addition, the applicability of microelectrophoresis to other types of cells has not been test yet. The following research questions will be answered in this chapter:

1. Is microelectrophoresis technique able to control the amount of nanomaterials to be delivered into live cells?
2. How are the delivered nanomaterials distributed and diffused within the cytoplasm?
3. What are the impacts of nanomaterials amount on the short-term and long-term cell viability and proliferation?
4. Are the delivered nanomaterials aggregated within the cytoplasm?
5. Whether microelectrophoresis can be applied to deliver nanomaterials to different cell types?

Part of the work in this chapter has been published and will be presented in publication format. The rest of the work will be presented in conventional format.

3.2 Publication 2

Controlled delivery of quantum dots using microelectrophoresis technique: Intracellular behavior and preservation of cell viability

Mengke Han,^{1,2} Samuel Evans,^{2,3} Sanam Mustafa,^{2,3} Steven Wiederman,^{2,3} Heike Ebendorff-Heidepriem^{1,2}

¹Institute for Photonics and Advanced Sensing (IPAS) and School of Physical Sciences, The University of Adelaide, Adelaide, South Australia 5005, Australia

²ARC Centre of Excellence for Nanoscale BioPhotonics (CNBP), The University of Adelaide, Adelaide, South Australia 5005, Australia


³Adelaide Medical School, The University of Adelaide, Adelaide, South Australia 5005, Australia

Published: Han, M., Evans, S., Mustafa, S., Wiederman, S. and Ebendorff-Heidepriem, H. (2022), Controlled delivery of quantum dots using microelectrophoresis technique: Intracellular behavior and preservation of cell viability, *Bioelectrochemistry*, Volume 144, 108035, ISSN 1567-5394.

Statement of Authorship

Title of Paper	Controlled delivery of quantum dots using microelectrophoresis technique: Intracellular behavior and preservation of cell viability
Publication Status	<input checked="" type="checkbox"/> Published <input type="checkbox"/> Accepted for Publication <input type="checkbox"/> Submitted for Publication <input type="checkbox"/> Unpublished and Unsubmitted work written in manuscript style
Publication Details	Mengke Han, Samuel Evans, Sanam Mustafa, Steven Wiederman, Heike Ebendorff-Heidepriem, Controlled delivery of quantum dots using microelectrophoresis technique: Intracellular behavior and preservation of cell viability, Bioelectrochemistry, Volume 144, 2022, 108035, ISSN 1567-5394.


Principal Author


Name of Principal Author (Candidate)	Mengke Han
Contribution to the Paper	Designed the project, performed the experiments of QDs suspension, micropipettes fabrication, intracellular delivery, cell viability test, and cell imaging, interpreted all the data, and wrote the whole manuscript.
Overall percentage (%)	90%
Certification:	This paper reports on original research I conducted during the period of my Higher Degree by Research candidature and is not subject to any obligations or contractual agreements with a third party that would constrain its inclusion in this thesis. I am the primary author of this paper.
Signature	 Date 05/01/2022

Co-Author Contributions

By signing the Statement of Authorship, each author certifies that:

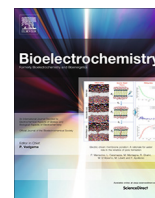
- i. the candidate's stated contribution to the publication is accurate (as detailed above);
- ii. permission is granted for the candidate to include the publication in the thesis; and
- iii. the sum of all co-author contributions is equal to 100% less the candidate's stated contribution.

Name of Co-Author	Samuel Evans
Contribution to the Paper	Performed the experiments of cell culture and fixation and helped in manuscript evaluation.
Signature	 Date 10/01/2022

Name of Co-Author	Sanam Mustafa
Contribution to the Paper	Helped in the conception and design of the project and revised the manuscript.
Signature	 Date 17/01/2022

Name of Co-Author	Steven Wiederman		
Contribution to the Paper	Helped in the conception and design of the project and revised the manuscript.		
Signature		Date	13/01/2022

Name of Co-Author	Heike Ebendorff-Heidepriem		
Contribution to the Paper	Helped in the conception and design of the project and contributed to structure and revise the manuscript.		
Signature		Date	13/01/2022



Controlled delivery of quantum dots using microelectrophoresis technique: Intracellular behavior and preservation of cell viability

Mengke Han^{a,b}, Samuel Evans^{b,c}, Sanam Mustafa^{b,c}, Steven Wiederman^{b,c}, Heike Ebdorff-Heidepriem^{a,b,*}

^aInstitute for Photonics and Advanced Sensing (IPAS) and School of Physical Sciences, The University of Adelaide, Adelaide, South Australia 5005, Australia

^bARC Centre of Excellence for Nanoscale BioPhotonics (CNBP), The University of Adelaide, Adelaide, South Australia 5005, Australia

^cAdelaide Medical School, The University of Adelaide, Adelaide, South Australia 5005, Australia

ARTICLE INFO

Article history:

Received 19 September 2021

Received in revised form 24 November 2021

Accepted 1 December 2021

Available online 4 December 2021

Keywords:

Intracellular delivery

Microelectrophoresis

Nanoparticles

Quantum dots

Intracellular tracking

ABSTRACT

The use of synthetic nanomaterials as contrast agents, sensors, and drug delivery vehicles in biological research primarily requires effective approaches for intracellular delivery. Recently, the well-accepted microelectrophoresis technique has been reported to exhibit the ability to deliver nanomaterials, quantum dots (QDs) as an example, into live cells, but information about cell viability and intracellular fate of delivered nanomaterials is yet to be provided. Here we show that cell viability following microelectrophoresis of QDs is strongly correlated with the amount of delivered QDs, which can be finely controlled by tuning the ejection duration to maintain long-term cell survival. We reveal that microelectrophoretic delivered QDs distribute homogeneously and present pure Brownian diffusion inside the cytoplasm without endosomal entrapment, having great potential for the study of dynamic intracellular events. We validate that microelectrophoresis is a powerful technique for the effective intracellular delivery of QDs and potentially various functional nanomaterials in biological research.

© 2021 Elsevier B.V. All rights reserved.

1. Introduction

Engineered nanomaterials with desired physical and chemical properties have been developed and widely used as imaging agents and delivery vehicles to decipher and modulate complex cellular processes.[1] Most of these applications require the effective cytosolic delivery of nanomaterials into living cells.[1,2] The major obstacle to intracellular delivery is the lipidic plasma membrane acting as a highly regulated barrier to prevent direct translocation of exogenous materials.[2–4] The delivery challenge of nanomaterials must be addressed before their promise in research or therapeutic and diagnostic applications can be fulfilled.[2] Current intracellular delivery strategies can be categorized into two modalities: (1) carrier-based techniques, which involve endocytosis and membrane fusion pathways, and (2) membrane-disruption-based techniques, which include plasma membrane permeabilization and direct penetration mechanisms.[2,5] For carrier-based delivery, a key issue is that only around 1% of the nanomaterials as car-

goes can escape endosomes as endocytosis is tightly regulated.[2,5,6] Most of these nanomaterials become entrapped within acidic lysosomes and experience degradation or regurgitation back to the cell surface.[2,5,7] Moreover, carrier-based delivery systems are inherently limited by the restricted combination of feasible cargoes, carrier materials and cell types.[2,5] In contrast, membrane-disruption-based techniques can bypass the endosomal entrapment by directly delivering nanomaterials of interest into the cell cytosol.[2] Nanomaterials that are freely dispersed throughout the cytoplasm have higher chances to reach target subcellular structures and organelles to elicit intended biological responses and medical functions.[8] Moreover, membrane-disruption-based modalities are near-universal, being able to deliver almost any submicron nanomaterial that can be dispersed in solution.[2,3,5] The latest understanding of membrane repair pathways indicates that cells are well equipped to deal with membrane disruption, which is a common event in their life.[2]

For membrane-disruption-based techniques, a diverse array of approaches have been developed to create transient discontinuities in the plasma membrane for the intracellular delivery of nanomaterials.[2,5] These approaches can be categorized as either permeabilization or direct penetration mechanism.[2] Techniques employing permeabilization mechanism, rely on mechanical,[9-

* Corresponding author at: School of Physical Sciences, Institute for Photonics and Advanced Sensing, The University of Adelaide, Adelaide, South Australia 5005, Australia.

E-mail address: heike.ebdorff@adelaide.edu.au (H. Ebdorff-Heidepriem).

[14] electrical,[15–18] optical,[19–22] and biochemical means,[12,23,24] to transiently permeabilize the membrane to nanomaterials present in the extracellular solution (i.e., cell culture media). [2] Nanomaterials then diffuse through membrane disruptions into the cytoplasm according to their concentration gradient.[2] Once cells detect the breached membrane, they rapidly activate the membrane repair processes to restore boundary integrity and then rebalance the membrane and cytoplasmic homeostasis to bring themselves back to full health.[2,25,26] The problem associated with permeabilization is that serum proteins in the culture media may adsorb nonspecifically onto the surface of nanomaterials to form protein coronas.[27–30] This will substantially alter the characteristics of these nanomaterials with an unintentional biological identity and impact nanotoxicology studies.[27–30] By contrast, techniques employing direct penetration mechanism can avoid the alteration of nanomaterials physicochemical properties occurred in permeabilization techniques.[8] They use a conduit or vehicle to break through the membrane and then create the direct entry for nanomaterials,[2] e.g., pressure microinjection,[15,31–34] biolistic projectiles,[35–39] and nanoneedles.[40–42]

Among direct penetration methods, microelectrophoresis technique uses electrical currents to introduce charged substances through fine-tipped glass micropipettes into living cells.[43] It has long been in widespread use for the intracellular delivery of fluorescent dyes, antibodies and plasmid DNA.[44–47] Recently, the feasibility of adapting microelectrophoresis for the intracellular delivery of nanomaterials has been demonstrated for the first time, where highly monodispersed QDs (prepared by an optimized protocol) were ejected through micropipettes with appropriate tip size into living cells.[48] Compared to pressure microinjection, which is also a pipette-based direct penetration technique, microelectrophoresis takes advantage of fine electrophoretic propulsion to drive charged nanomaterials into cells rather than high pressure pulses,[49–51] which avoids untoward impact on cytoplasmic pressure and provides higher cell viability post injection.[44] Moreover, for adherent cultured cells, microinjection is purely based on optical observation, where the height of cells and tip of micropipettes are difficult to determine (i.e., whether the tip just impales the adherent cell or touches the cell culture dish through the cell).[44] Therefore, multiple injection attempts are often necessary, which further decreases the cell viability and leads to fairly low injection success rates.[44] In contrast, microelectrophoresis offers accurate position feedback about the approach, penetration and injection process for the user via electrophysiological measurements.[52] Impalement of target cells is confirmed when the resting membrane potential (about -30 to -180 mV) is recorded,[53,54] which is applicable to cell culture,[44,55] tissue slice and small animals.[43,45,47,53,56–58] Although the feasibility has been confirmed,[48] implementation of microelectrophoresis technique for the delivery of nanomaterials is still at a nascent stage, where the cell viability following microelectrophoresis and the intracellular fate of delivered nanomaterials have not been investigated.

In this study, we examine the implication of microelectrophoresis technique for delivered QDs inside cytoplasm and cell survival. We present the ability of microelectrophoresis to finely control the amount of QDs to be loaded into single cells by adjusting the ejection duration, which has substantial impact on short-term and long-term cell health. We observe and report the diffusion properties and spatiotemporal distribution of microelectrophoretic delivered QDs inside cytoplasm. Our findings provide a deeper understanding of the performance of microelectrophoretic-mediated delivery of nanomaterials. We anticipate that our work will benefit the intracellular delivery toolkit and catalyze new

delivery solutions for QDs and possibly other synthetic nanomaterials.

2. Experimental section

2.1. Characterization and preparation of QDs suspension.

The QDs (Q21521MP; Invitrogen) used here were encapsulated within amine-derivatized polyethylene glycol (PEG) polymer, which is a standard strategy to provide colloidal stability. These nonbranched PEG ligands have large exclusion volumes due to their high conformational entropy, and high resistance to biomolecules adsorption via steric repulsion.[59–61] Moreover, PEG modification is considered to be the best biocompatible material to mitigate QDs-induced adverse effects.[62–64] It forms a fence-like structure on the QD surface, which can effectively prevent the chemical degradation of QDs and the release of metal ions to the intracellular environment.[62] To further prevent the aggregation tendency of QDs within the tip of micropipettes and inside live cells following ejection, we used the optimized protocol reported previously to prepare QDs suspensions to fill micropipettes.[48] QDs were prepared in 0.01 M KCl solution to a concentration of 10 nM with pH adjusted to 9.78. Measurements with Zetasizer nano ZSP (Malvern Instruments) confirmed that the QDs were fully monodispersed with theoretically expected hydrodynamic diameters of ~ 10 – 35 nm (Fig. 1a) and a stable negative zeta potential of -18.2 mV.

2.2. Cell culture and microelectrophoresis process.

Human embryonic kidney (HEK293) cells were seeded at 80,000 cells/dish onto a low-wall 35 mm imaging dish (80156; ibidi) and cultured (37 °C in a humidified incubator at 5% CO_2) for two days in 1 mL Dulbecco's modified Eagle's media (DMEM) supplemented with 2 mM L-glutamine and 10% fetal bovine serum (FBS) prior to the electrophoretic delivery of QDs. During electrophoresis, the medium was changed to 2 mL DMEM supplemented with 25 mM HEPES and 5% FBS (21063045; Thermo fisher) to maintain physiological pH in atmosphere at room temperature. A glass micropipette with tip ID of ca. 200 nm was backfilled with QDs suspension. The micropipette was inserted with an Ag/AgCl working electrode from the blunt end and was held by a micromanipulator (Sensapex) to move towards target cells at a 50° angle (Fig. 1b). Another Ag/AgCl counter electrode was carefully placed into the medium. The two electrodes were connected to the headstage of an intracellular bridge mode amplifier (BX-01; np) to form a complete electrical circuit. A change in potential difference around -20 to -40 mV indicated that the tip of micropipette was successfully pierced through the cell membrane into the cytoplasm of the cell. An electrical current of -0.2 nA was then applied to eject QDs into the cell.

2.3. Live cell imaging and QDs tracking.

HEK293 cells and the micropipette were visualized during the microelectrophoresis process (Fig. 1c) using 40X water immersion objective (1.25NA) on a Nikon Ti-E inverted microscope equipped with cage incubator (Okolab). Delivered QDs clusters (emission maxima of 655 nm) were imaged immediately after injection and tracked with 100X oil immersion objective (1.45NA) using 440 nm excitation light.

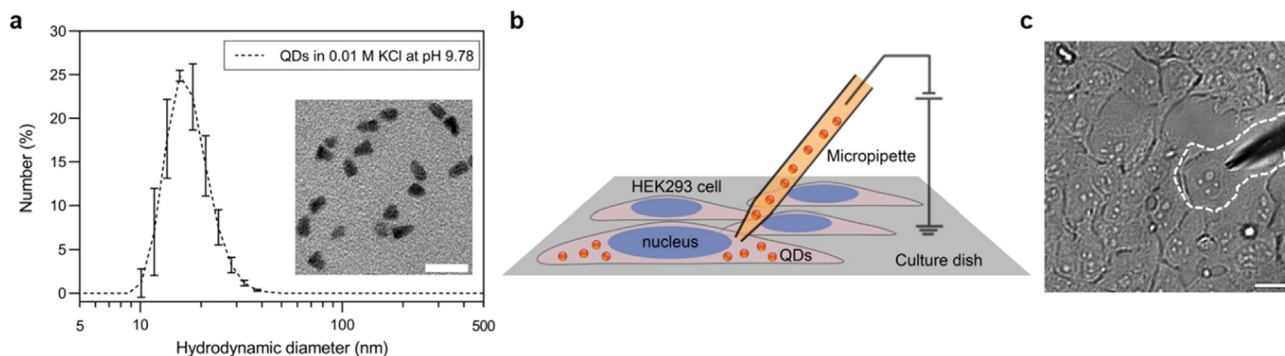


Fig. 1. (a) Hydrodynamic diameter distribution of QDs in 0.01 M KCl solution with pH adjusted to 9.78, indicating the monodispersity of QDs. Inset shows the transmission electron microscope (TEM) image of QDs. Scale bar, 25 nm. (b) Schematic of the microelectrostatic delivery of QDs into HEK293 cells. (c) Differential interference contrast (DIC) micrograph showing a cell being pierced with a micropipette filled with QDs suspension. The cell is outlined with white dotted lines for better visibility. Scale bar, 20 μm .

2.4. Data analysis.

The Manual Tracking plugin in ImageJ was used to analyze the time-lapse image series of delivered QDs by tracking the locations of QDs clusters in each frame. The localization of QDs clusters in a frame was established by fitting the fluorescence signal of the cluster using a Gaussian, and the center of the Gaussian was considered as the cluster location. By connecting the locations in all frames, the trajectory of a QD cluster over a certain period was identified. The $x(t)$, $y(t)$ positions of QDs clusters in each frame were determined and exported by ImageJ software. The $x(t)$, $y(t)$ information on a QD cluster was then imported into a freely available MATLAB tool @msdanalyser for the calculation of MSD using the following equation:[65]

$$MSD(n\Delta t) = \frac{1}{N} \sum_{i=1}^N ((x_{i+n} - x_i)^2 + (y_{i+n} - y_i)^2)$$

where N is the total number of frames, Δt is the interval between frames, and x_i and y_i are the positions on the i th frame. MSD was then plotted against time. Here we only took the first 7 s data points for the fitting of MSD plots to achieve optimum accuracy for the diffusion coefficient.[66,67] It has been suggested that the accuracy of a MSD curve is influenced by the limited localization precision of the trajectory and noise in an experimental situation, thus the accuracy of each data point in a MSD curve varies with respect to each other.[66,68,69] Moreover, for increasing lag times, the accuracy of these data points decreases due to the progressively decreasing averaging of the available data.[69] Therefore, taking too many data points into account for fitting the MSD curve can lead to a deterioration rather than an improvement of the result.[69] A linear dependency of MSD on time indicates pure Brownian diffusion. MSD was fitted to $4Dt$ to generate the diffusion coefficient D .

2.5. Cell viability test, confocal microscopy and 3D visualization.

The viability of treated cells was tested *in situ* by NucRed Dead 647 reagent (R37113; Thermo fisher). We added two drops of the reagent per mL cell culture media and incubated the cells for 15 mins. The NucRed was then excited at 640 nm by live cell fluorescence microscopy and emitted at 670 nm, which did not interfere with QDs excitation (440 nm) and emission (655 nm). The reagent entered the cell through compromised plasma membrane and then bound to nuclear DNA to examine the viability. Immediately after cell viability examination, cell culture medium was removed from the dishes and the cells were washed twice with

phosphate-buffered saline (PBS). Then 1 mL 4% paraformaldehyde solution was added to the dishes to fix the cells at room temperature for 10 min. After that, the cells were washed with PBS for three times to remove residual paraformaldehyde. The confocal images of the fixed cells were collected on an inverted confocal laser scanning microscope (FV3000; Olympus) using 405 nm excitation laser and 60x oil immersion objective lens (1.40NA). Optimized emission detection bandwidths were configured by Olympus control software. All confocal z-stacks were processed and reconstructed using IMARIS software package (Bitplane AG, Zurich, Switzerland) for 3D visualization.

3. Results and discussion

3.1. Impact of ejection duration on QDs amount and distribution.

Under a constant current of -0.2nA , HEK cells were injected with QDs for either 1, 2 or 3 min. The differential interference contrast (DIC), fluorescence, and overlaid images of typical results clearly revealed that a longer ejection duration led to stronger and denser fluorescence signals (Fig. 2), which indicates higher loading of QDs into the cells. Moreover, an expanded distribution of delivered QDs throughout the cytoplasm was achieved after a longer ejection duration. As a control, QD filled micropipettes were embedded into the cytoplasm for 3 mins with no current applied. The sole QDs fluorescent spot observed near the injection point in the control cell was caused by their passive diffusion from the orifice. This phenomenon was also observed in QDs-delivered cells (i.e., injected with QDs via microelectrophoresis). QDs were concentrated near the injection point from where they then migrated into the cytoplasm under the applied electrical current.

3.2. Optimization of imaging conditions.

The cell viability after microelectrophoresis is affected by photodamage that occurs during fluorescence imaging. Therefore, it is important to consider the excitation strength that cells can sustain and use them efficiently in live cell experiments to prevent phototoxicity effects.[70] In this study, the fluorescence of the delivered QDs (emission maxima of 655 nm) was excited using blue light at 440 nm, which is genotoxic as it can produce reactive oxygen species to directly damage deoxyribonucleic acid (DNA) base and break DNA stands.[71-73] Upon excitation, QDs themselves act as photosensitizers and form free radicals that react with intracellular contents as well.[74] If the cell cannot handle the oxidative stress, these accumulating phototoxic events during irradiation will ultimately kill it.[70,75] As expected, after prolonged

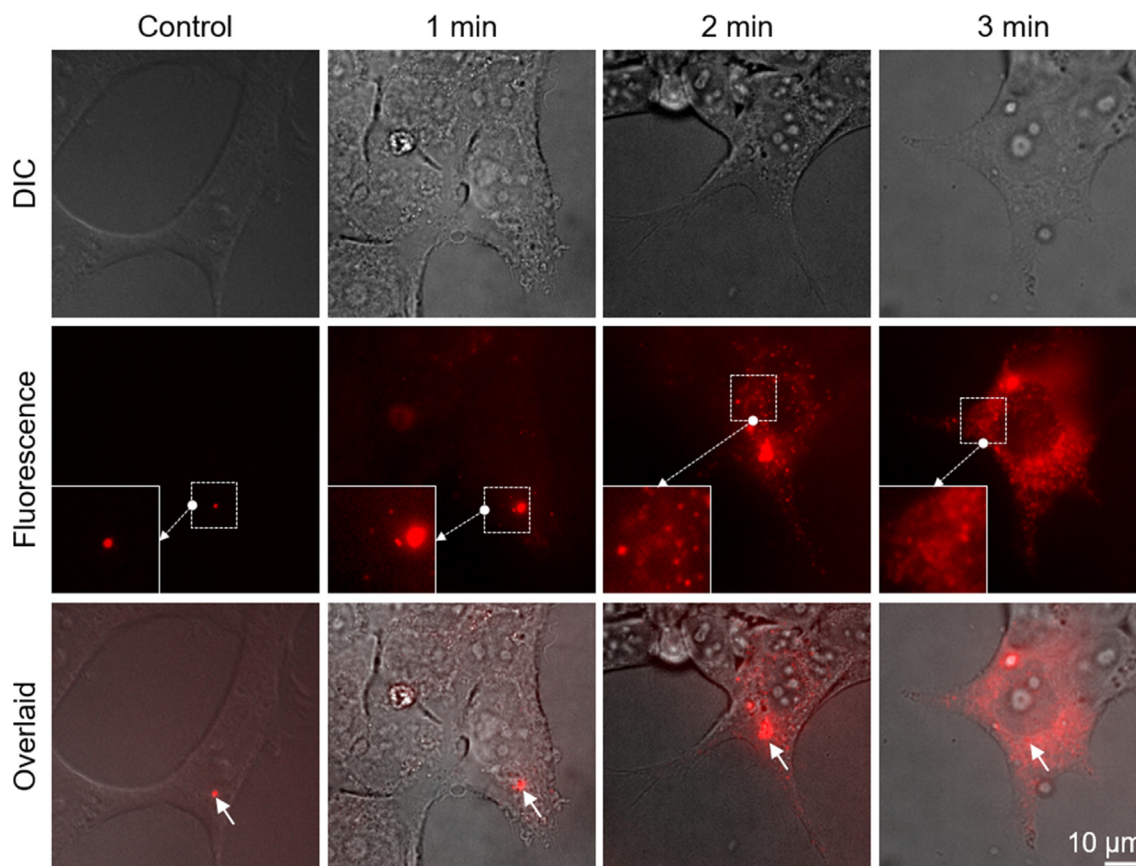


Fig. 2. Representative DIC, fluorescence and overlaid images of HEK293 cells with microelectrophoretic-delivered QDs under a constant current of -0.2nA for 1, 2 and 3 mins ($n = 50$ in 8 independent experiments). No current was applied to the control cell. Scale bar, $10\ \mu\text{m}$. Magnified insets (left bottom on fluorescence images) show the details of delivered QDs in the areas outlined by white dash lines. The injection points are indicated by white arrows on overlaid images.

exposure to 440 nm excitation for 1 min, we observed that a QDs-delivered cell (injected for 2 mins) and its neighbours quickly died (Figure S1). We optimized the imaging conditions by using a much lower 440 nm light intensity along with shorter exposure time and maximal camera gain. With optimal imaging conditions, we were able to study the impact of QDs amount on short-term and long-term cell viability as described in the following.

3.3. Impact of QDs amount on short-term cell viability.

The average volume of mammalian cells is approx. 3–5 picoliter.[76–78] The interior membrane-enclosed compartments together occupy nearly half of this small space, further reducing the free volume available to diffusing substances in the cytoplasm.[76,79] Therefore, it is important to ensure that the ejecting current is of adequate duration so that the resulting damage to cells is not too severe or prolonged, otherwise the cells will be unable to repair and recover.[2,43] Here, each cell was constantly monitored for 10 min to make sure no obvious morphology change occurred after the injection of QDs. Within this period, all cells sustained the 1 and 2 mins loading of QDs ($n = 20$ for each duration). However, among other 10 cells with excessive loading of QDs (3 mins ejection duration), four cells did not survive, where visible morphology change was observed after the injection. In a notable example of a cell with 3 mins loading of QDs (Fig. 3a), a visible blister-like protrusion of $\sim 10\ \mu\text{m}$ size and full of QDs was observed on the cell surface after 4 mins following the injection (Fig. 3b). The formation of this blister-like protrusion can be attributed to the Gibbs-Donnan effect.[80] When the cell was loaded with large amount of QDs, these negatively charged particles strongly

absorbed a massive amount of positive ions near the surface.[81] The decrease of intracellular free cations induced osmolarities imbalance, drawing extracellular cations into the cytoplasm.[81] The cations accumulation caused a charge gradient which subsequently facilitated the entry of extracellular anions, ultimately resulting in intracellular hyper osmosis and the excessive influx of osmotically obliged water.[81–83] Then the hypoosmotic pressure generated outward tension and strain in the contractile cytoskeleton,[84,85] which led to the extensively swollen cell that we observed. It has been proposed that the swelling can activate specific stress signaling events and is an early manifestation of necrotic cell death.[86]

3.4. Impact of QDs amount on long-term cell viability.

As described above, the magnitude of damage, (i.e., the amount of delivered QDs), that each cell can sustain in short term is variable, with some cells being instantly killed while others remain almost unaffected. We further monitored the unaffected cells to determine their long-term viability. To quantify the long-term cell viability, we stained the QDs-delivered cells with NucRed Dead 647 reagent after 24 h incubation, which enters the damaged or dead cell through compromised plasma membrane and then emits far-red fluorescence at 661 nm upon binding to nuclear DNA (Figure S2). A less amount of delivered QDs, (i.e., 1 min and 2 mins ejection duration), resulted in better cell survival, where the percentage of viable cells changed from 100% after 10 mins observation to 95% and 80% after 24 h incubation ($n = 20$ for each duration, in 8 independent experiments, Fig. 4a). However, a higher loading of QDs, (i.e., 3 mins ejection duration), further

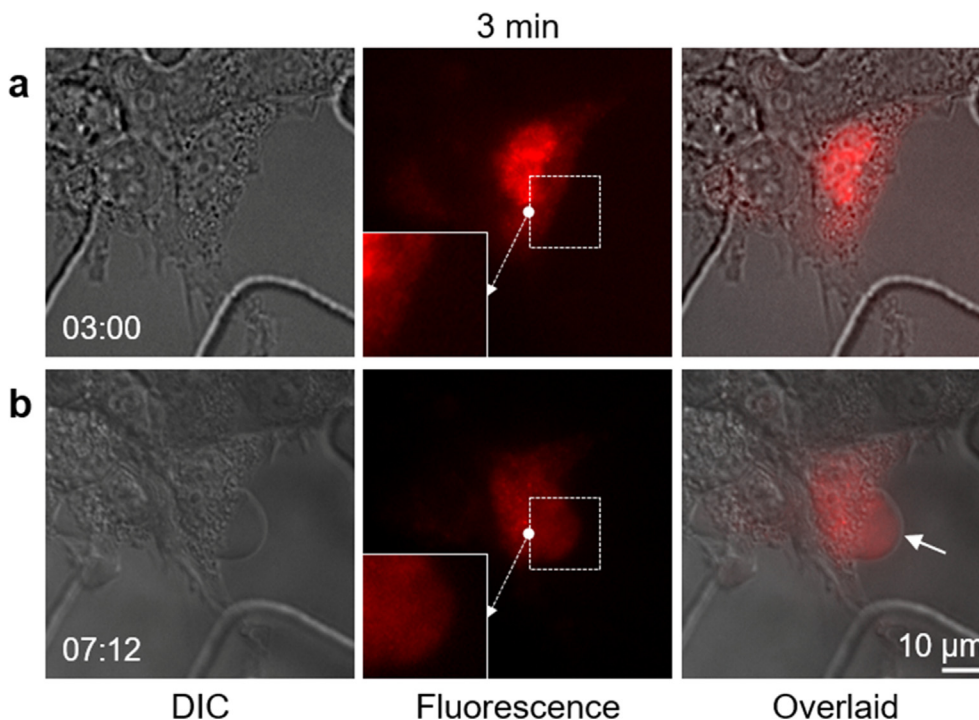


Fig. 3. (a) DIC, fluorescence and overlaid images of a HEK293 cell injected with QDs under a constant current of -0.2nA for 3 mins. (b) A blister-like protrusion with a size of $\sim 10\ \mu\text{m}$ was then formed on the cell surface 4 mins after the injection, indicated by the white arrow. Magnified insets (left bottom on fluorescence images) show the details of delivered QDs in the protrusion outlined by white dash lines. The timestamp for the captured image is noted on the left bottom. The start time of injection is set as 00:00. Scale bar, $10\ \mu\text{m}$.

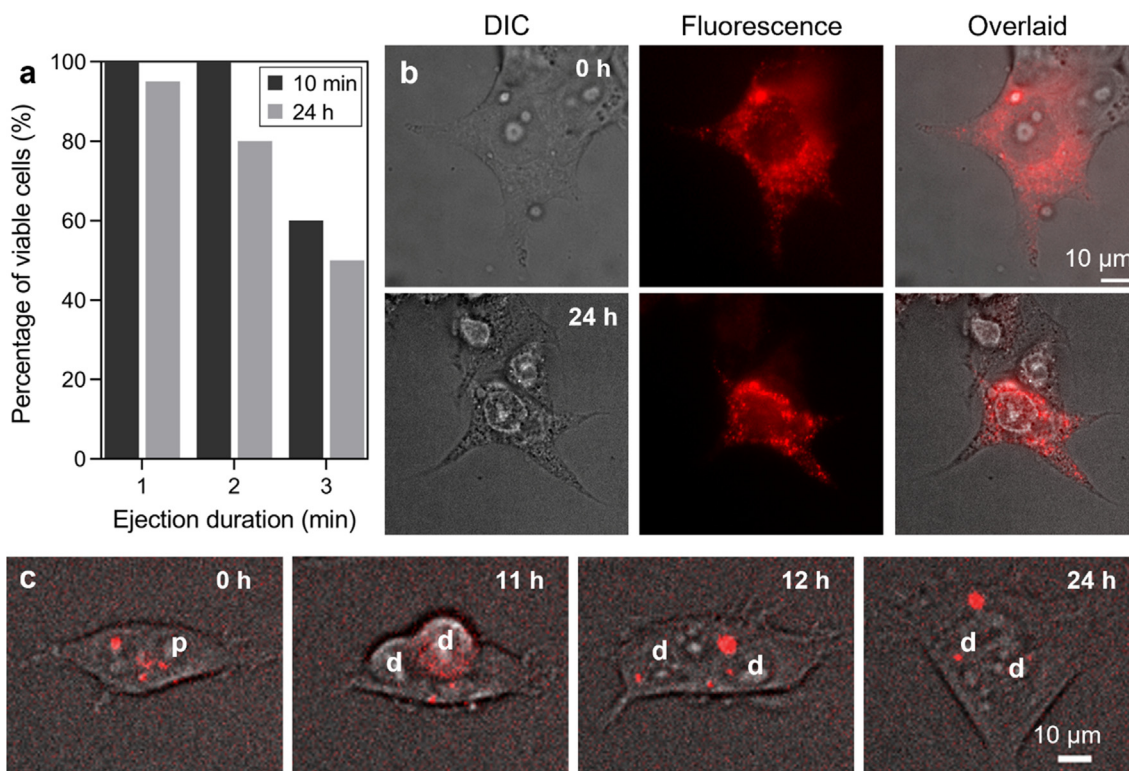


Fig. 4. (a) Cell viability following the microelectroporation delivery of QDs with different ejection duration after 10 mins and 24 h incubation (number of cells: 20 cells for 1 min and 2 mins, 10 cells for 3 mins ejection duration in 8 independent experiments, respectively). (b) DIC, fluorescence and overlaid images of a HEK293 cell with microelectroporation-delivered QDs for 3 mins and after 24 h incubation. Scale bar, $10\ \mu\text{m}$. (c) Overlaid time-lapse images for 24 h of a live HEK293 cell delivered with QDs for 1 min. “p” marks parental cell and “d” is for the corresponding daughter cells. The proliferation event occurred after 11 h incubation. Scale bar, $10\ \mu\text{m}$.

decreased the percentage of viable cells from 60% after 10 mins observation to 50% after 24 h incubation ($n = 10$). We found that cells sustaining the 3 mins loading of QDs in short term were able to survive after 24 h incubation, as shown in Fig. 4b for one example. Besides the fluorescence-based cell viability tests that assess cell membrane integrity, another important indication of a live cell is its capability to reproduce.[87] Therefore, we monitored these QDs-delivered cells during 24 h incubation and observed that several cells with 1 min loading of QDs were able to proliferate after 24 h, where the progression of mitosis was observed, and their QDs were inherited by their daughter cells (Fig. 4c). We attribute the retention of cell viability to the reduced loading of QDs, which avoids undesirable perturbation to the intracellular environment. This demonstrates the major advantage of microelectrophoresis to achieve accurate dispensation of QDs to individual cells, thus preserving the health of the cell to the maximum extent possible.

3.5. Size distribution of delivered QDs.

The aqueous cytoplasm is a space crowded with macromolecules where all intracellular activities that are not sequestered within membrane-bounded organelles occur.[76,88,89] Once delivered into this complex and crowded system, the high ionic strength of the cytoplasm can induce charge screening of nanomaterials. Moreover, the nonspecific adsorption of biomolecules can affect the dispersity of nanomaterials, both leading to ubiquitous and inevitable aggregation phenomenon of all nanomaterials.[30] The QDs used in this study were simply encapsulated with amine-derivatized PEG polymers to provide colloidal stability and thus they were nontargeted to any designated site of action.

They were expected to eventually aggregate in the complex intracellular environment. To examine the dispersity of delivered QDs inside live cells in real time, we used fluorescence microscopy where the fluorescence of QDs was collected by an 100x oil immersion objective (1.45NA) to achieve highest spatial resolution of $0.13 \mu\text{m}$ per pixel (i.e., the size of a diffraction-limited spot). This highest achievable resolution was not sufficient to reveal the details, i.e., the number of individual QDs within a spot.[90] Although TEM provides higher resolution around 0.2 nm ,[91] it is not applicable for live cell imaging yet and thus was not employed here.[87] We randomly selected and measured the size of 115 QDs fluorescent spots in the cytoplasm of 10 QDs-delivered cells, where most of them were in the range of 0.3 to $0.7 \mu\text{m}$ (Fig. 5a). This infers that delivered QDs remained inside the cytoplasm instead of entering the nucleus as they were much larger than the size of the nuclear envelope pores of $\sim 10 \text{ nm}$. [92]

3.6. Dynamic motion of delivered QDs.

Nanomaterials that freely diffuse throughout the cytoplasm have higher chances to interact with target biological entities.[8] Therefore, we tracked the intracellular movement of the QDs fluorescent spots over time by taking time-lapse image series. The QDs trajectories were identified by linking the center of the spots in subsequent frames (1 s per frame). The trajectories of a $0.4 \mu\text{m}$ and a $0.7 \mu\text{m}$ QDs fluorescent spot near each other in the same cell were captured for 30 s (Fig. 5b). They both showed incessant random walk due to Brownian motion rather than linear movements, [93] which was reasonable since the PEG coatings here had no functionality, (i.e., conjugation with macromolecules), other than

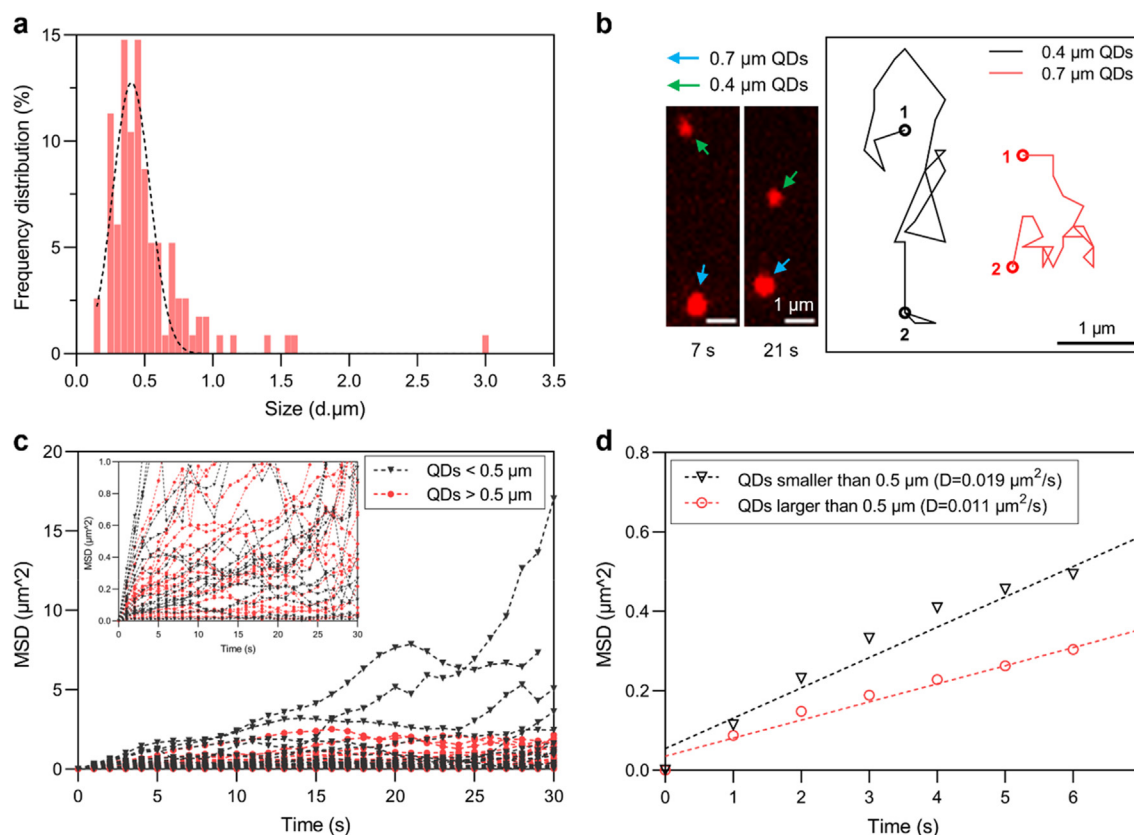


Fig. 5. (a) Size distribution of QDs fluorescent spots inside live HEK293 cells (10 cells, 115 spots). (b) QDs fluorescence spot trajectory comparison between 0.7 and $0.4 \mu\text{m}$. Scale bar $1 \mu\text{m}$. Left panel $t = 7 \text{ s}$; Right panel $t = 21 \text{ s}$. (c) Mean square displacement (MSD) curves derived from the trajectory of QDs fluorescent spots having different sizes (20 spots in 5 cells for each size range) in Brownian motion (30 points, time step $\Delta t = 1 \text{ s}$). Inset shows the trajectory of larger QDs fluorescent spots having MSD lower than $1 \mu\text{m}^2$. (d) Fitting of the weighted mean of all MSD plots in the first 7 s ($R^2 = 95\%$ for smaller spots, $R^2 = 97\%$ for larger spots) with diffusion coefficient calculated.

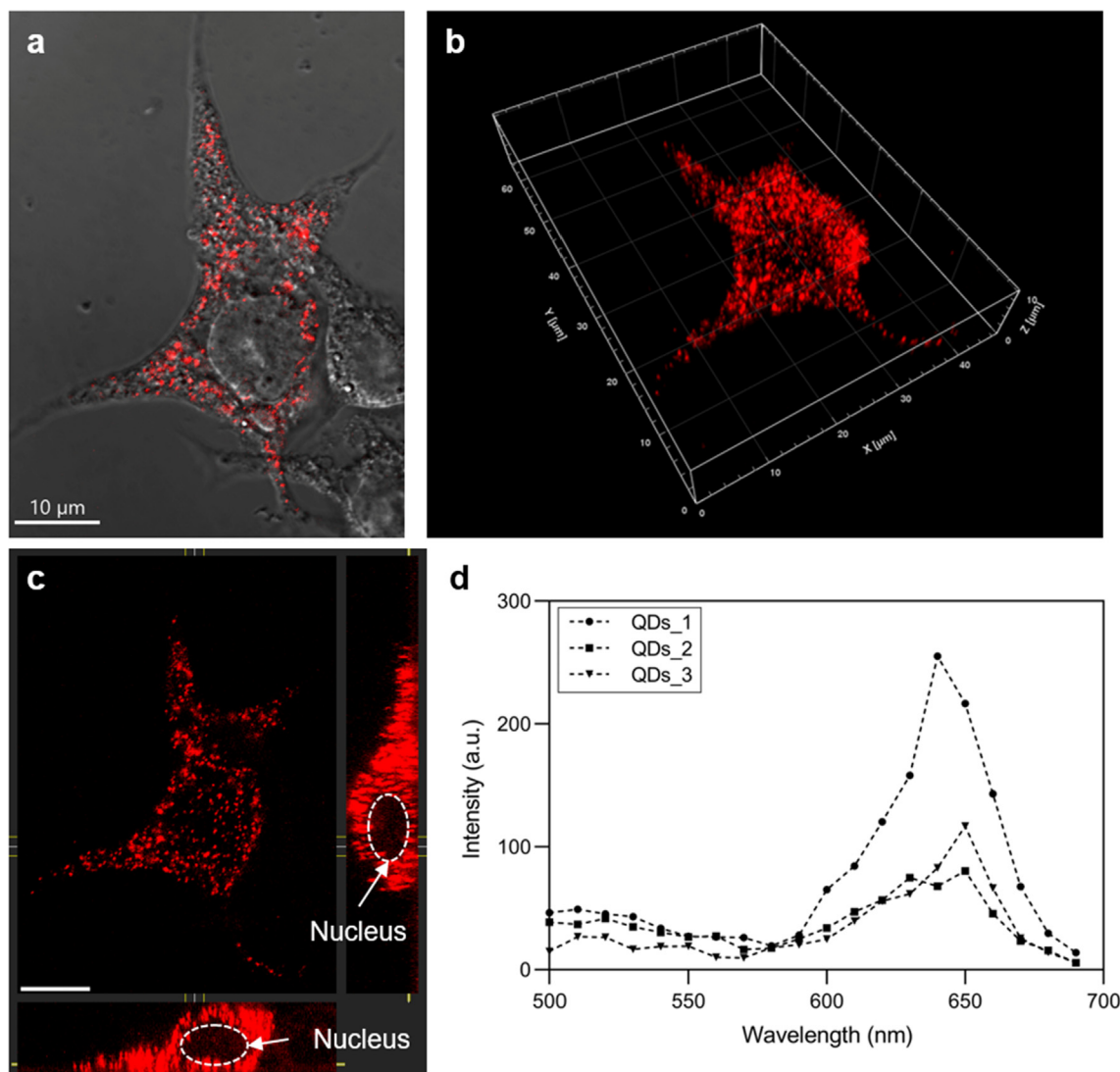


Fig. 6. (a) Overlaid confocal image of the cell after fixation. (b) Reconstruction of confocal z-stack images showing the 3D distribution of delivered QDs. (c) The y-z and x-z cross-sectional image stacks through the yz and xz planes. Cell nucleus was indicated by white dash lines and arrows. (d) The spectral curve of three QDs fluorescent spots acquired by λ -stack function.

providing biocompatibility for QDs.[94] The difference was that the 0.7 μm QDs fluorescent spot was more confined spatially, presumably by intracellular obstacles due to its larger size. Thus, we hypothesize that QDs fluorescent spots with different sizes could have varying dynamic motion. We used mean square displacement (MSD) analysis to characterize the trajectories of more QDs fluorescent spots (Fig. 5c, see the Supporting Information for data analysis details). We sorted them into two groups according to their sizes, either above or below 0.5 μm . For each size range, we randomly selected 20 fluorescent spots in 5 cells (frequency distribution in Figure S3). Movies on the QDs movement are provided in the Supporting Information. Except for several small spots that rapidly diffused far away from their original sites after 15 s, there were no obvious differences in the movement of most delivered QDs. The fitting of the weighted mean of all MSD plots for two size ranges in the first 7 s were both linear (Fig. 5d), indicating a pure Brownian motion, with a mean diffusion coefficient (D) of $0.019 \pm 0.004 \mu\text{m}^2/\text{s}$ for smaller QDs fluorescent spots and a slightly reduced D of $0.011 \pm 0.002 \mu\text{m}^2/\text{s}$ for larger QDs fluorescent spots. These results match the range observed in other studies.[16,95,96] indicating that microelectrophoresis did not alter the diffusion proper-

ties of QDs. This showcases the potential of microelectrophoretic delivered QDs as fluorescent labels to monitor dynamic events within the cytoplasm.

3.7. 3D distribution and spectrum of delivered QDs.

Cells with delivered QDs were immediately fixed after 24 h incubation and the cell viability test described above. To reconstruct the distribution of these delivered QDs in three dimensions, z-stacks sectioning through entire fixed cells were taken by confocal laser scanning microscopy (Fig. 6a,b). The y-z and x-z cross-sectional image stacks through the yz and xz planes confirmed that QDs were homogeneously dispersed throughout the cytoplasm instead of on the cell surface or inside the nucleus (Fig. 6c). To validate that the collected fluorescence signals were from delivered QDs, we also acquired spectral data as a series of images at different wavelength bands by steps (λ -stacks). Each band spans a limited spectral region of 10 nm (Figure S4). We selected three fluorescent spots and merged their intensity values to show a continuous spectral curve with peak position at 655 nm (Fig. 6d), which matched the emission maxima specification of QDs used

in this study. This is direct evidence showing that the collected fluorescence signals were from delivered QDs, rather than background autofluorescence arising from endogenous fluorophores. [97]

4. Conclusions

In summary, we demonstrate that microelectrophoresis technique has the capacity to deliver QDs homogeneously into the cytoplasm of live cells without endosomal entrapment or entering the nucleus. By adjusting the ejection duration, we can control the amount of QDs to be dispensed into individual cells and thus avoid undesirable perturbation to the intracellular environment and preserve their health. Delivered QDs diffuse freely inside the cytoplasm, thus having the potential for labeling and probing long-term intracellular dynamic events. These results point to an opportunity for future studies with microelectrophoresis, where it is a promising strategy for the intracellular delivery of QDs and potentially other nanomaterials into a wide range of cell types.

For future studies, more accurate imaging techniques, (e.g., live cell TEM and super resolution microscopy), [98,99] are expected to resolve and evaluate the dispersity of single QDs and other nanomaterials after microelectrophoretic delivery, which were not assessable here by fluorescence microscopy due to limited resolution and sensitivity.

Declaration of Competing Interest

The authors declare that they have no known competing financial interests or personal relationships that could have appeared to influence the work reported in this paper.

Acknowledgements

This work was performed in part at the Optofab node of the Australian National Fabrication Facility (ANFF) utilizing Commonwealth and SA State Government funding. The authors acknowledge partial support from the Australian Research Council Centre of Excellence for Nanoscale BioPhotonics (CNBP) (CE140100003) and Discovery Early Career Researcher Award (DECRA) from Australian Research Council (ARC) (DE150100548). M.H. thanks J. Sibbons for her assistance in live cell and confocal microscopy at Adelaide Microscopy.

Appendix A. Supplementary material

Supplementary data to this article can be found online at <https://doi.org/10.1016/j.bioelechem.2021.108035>.

References

- [1] L.Y. Chou, K. Ming, W.C. Chan, *Chem. Soc. Rev.* 40 (2011) 233–245.
- [2] M.P. Stewart, R. Langer, K.F. Jensen, *Chem. Rev.* 118 (2018) 7409–7531.
- [3] M. Sun, X. Duan, *Nanotechnology and Precision Engineering* 3 (2020) 18–31.
- [4] A.I. Prokop, *Delivery: Fundamentals and Applications*, Vol. 5, Springer Science & Business Media, 2011.
- [5] M.P. Stewart, A. Sharei, X. Ding, G. Sahay, R. Langer, K.F. Jensen, *Nature* 538 (2016) 183–192.
- [6] J. Gilleron, W. Querbes, A. Zeigerer, A. Borodovsky, G. Marsico, U. Schubert, K. Manygoats, S. Seifert, C. Andree, M. Stöter, *Nat. Biotechnol.* 31 (2013) 638–646.
- [7] G. Sahay, W. Querbes, C. Alabi, A. Eltoukhy, S. Sarkar, C. Zurenko, E. Karagiannis, K. Love, D. Chen, R. Zoncu, *Nat. Biotechnol.* 31 (2013) 653–658.
- [8] N.D. Donahue, H. Acar, S. Wilhelm, *Adv. Drug Deliv. Rev.* 143 (2019) 68–96.
- [9] N.T. Emerson, C.-H. Hsia, I.U. Rafalska-Metcalf, H. Yang, *Nanoscale* 6 (2014) 4538–4543.
- [10] J. Lee, A. Sharei, W.Y. Sim, A. Adamo, R. Langer, K.F. Jensen, M.G. Bawendi, *Nano Lett.* 12 (2012) 6322–6327.
- [11] Y. Wang, Y. Yang, L. Yan, S.Y. Kwok, W. Li, Z. Wang, X. Zhu, G. Zhu, W. Zhang, X. Chen, *Nat. Commun.* 5 (2014) 1–9.

- [12] K. Medepalli, B.W. Alphenaar, R.S. Keynton, P. Sethu, *Nanotechnology* 24 (2013) 205101.
- [13] J. Xu, T. Teslaa, T.-H. Wu, P.-Y. Chiou, M.A. Teitell, S. Weiss, *Nano Lett.* 12 (2012) 5669–5672.
- [14] Y. Deng, M. Kizer, M. Rada, J. Sage, X. Wang, D.-J. Cheon, A.J. Chung, *Nano Lett.* 18 (2018) 2705–2710.
- [15] A.M. Derfus, W.C. Chan, S.N. Bhatia, *Adv. Mater.* 16 (2004) 961–966.
- [16] C. Sun, Z. Cao, M. Wu, C. Lu, *Anal. Chem.* 86 (2014) 11403–11409.
- [17] Katrukha, E. A.; Mikhaylova, M.; van Brakel, H. X.; en Henegouwen, P. M. v. B.; Akhmanova, A.; Hoogenraad, C. C.; Kapitein, L. C. *Nature communications* 2017, 8, 1–8.
- [18] P.E. Boukany, A. Morss, W.-C. Liao, B. Henslee, H. Jung, X. Zhang, B. Yu, X. Wang, Y. Wu, L. Li, *Nat. Nanotechnol.* 6 (2011) 747–754.
- [19] K. Rhodes, I. Clark, M. Zatzoff, T. Eustaquio, K.L. Hoyte, M.R. Koller, *Methods Cell Biol.* 82 (2007) 309–333.
- [20] I. Clark, E.G. Hanania, J. Stevens, M. Gallina, A. Fieck, R. Brandes, B.O. Palsson, M.R. Koller, *J. Biomed. Opt.* 11 (2006) 014034.
- [21] C. McDougall, D.J. Stevenson, C.T. Brown, F. Gunn-Moore, K. Dholakia, *J. Biophotonics* 2 (2009) 736–743.
- [22] J. Umanzor-Alvarez, E.C. Wade, A. Gifford, K. Nontapot, A. Cruz-Reese, T. Gotoh, J.C. Sible, G.A. Khodaparast, *Biotechnol. J.* 6 (2011) 519–524.
- [23] R. Levy, U. Shaheen, Y. Cesbron, V. See, *Nano reviews* 1 (2010) 4889.
- [24] Lukyanenko, V. In *Cellular and Subcellular Nanotechnology*; Springer, 2013, pp 57–63
- [25] S.T. Cooper, P.L. McNeil, *Physiol. Rev.* 95 (2015) 1205–1240.
- [26] P.L. McNeil, T. Kirchhausen, *Nat. Rev. Mol. Cell Biol.* 6 (2005) 499–505.
- [27] M. Mahmoudi, N. Bertrand, H. Zope, O.C. Farokhzad, *Nano Today* 11 (2016) 817–832.
- [28] A. Albanese, P.S. Tang, W.C. Chan, *Annu. Rev. Biomed. Eng.* 14 (2012) 1–16.
- [29] C.D. Walkey, W.C. Chan, *Chem. Soc. Rev.* 41 (2012) 2780–2799.
- [30] I. Montes-Burgos, D. Walczyk, P. Hole, J. Smith, I. Lynch, K. Dawson, *J. Nanopart. Res.* 12 (2010) 47–53.
- [31] J.R. Slotkin, L. Chakrabarti, H.N. Dai, R.S. Carney, T. Hirata, B.S. Bregman, G.I. Gallicano, J.G. Corbin, T.F. Haydar, *Developmental dynamics: an official publication of the American Association of Anatomists* 236 (2007) 3393–3401.
- [32] I.L. Medintz, T. Pons, J.B. Delehanty, K. Susumu, M. Brunel, P.E. Dawson, H. Mattoussi, *Bioconjug. Chem.* 19 (2008) 1785–1795.
- [33] R. Singhal, Z. Orynbayeva, R.V.K. Sundaram, J.J. Niu, S. Bhattacharyya, E.A. Vitol, M.G. Schrlau, E.S. Papazoglou, G. Friedman, Y. Gogotsi, *Nat. Nanotechnol.* 6 (2011) 57–64.
- [34] B. Dubertret, P. Skourides, D.J. Norris, V. Noireaux, A.H. Brivanlou, A. Libchaber, *Science* 298 (2002) 1759–1762.
- [35] K. Nishizawa, M. Bremerich, H. Ayade, C.F. Schmidt, T. Ariga, D. Mizuno, *Sci. Adv.* 3 (2017) e1700318.
- [36] J.A. O'Brien, S.C. Lummis, *BMC Biotech.* 11 (2011) 1–6.
- [37] Y. Li, S.A. Vanapalli, M.H. Duits, *Biorheology* 46 (2009) 309–321.
- [38] D. Wirtz, *Annu. Rev. Biophys.* 38 (2009) 301–326.
- [39] A. Webster, P. Coupland, F. Houghton, H. Leese, J. Aylott, *Biochem. Soc. Trans.* 35 (2007) 538–543.
- [40] S. Park, Y.-S. Kim, W.B. Kim, S. Jon, *Nano Lett.* 9 (2009) 1325–1329.
- [41] J.-A. Huang, V. Caprettini, Y. Zhao, G. Melle, N. Maccaferri, L. Deleye, X. Zambrana-Puyalto, M. Ardini, F. Tattusi, M. Dipalo, *Nano Lett.* 19 (2019) 722–731.
- [42] E. Hebisch, M. Hjort, D. Volpati, C.N. Prinz, *Small* (2021) 2006421.
- [43] Curtis, D. R. In *Electrophysiological Methods*; Elsevier, 1964, pp 144–190
- [44] M. Simonis, W. Hübner, A. Wilking, T. Huser, S. Hennig, *Sci. Rep.* 7 (2017) 41277.
- [45] E.H. Buhl, J. Lübke, *Neuroscience* 28 (1989) 3–16.
- [46] S.L. Moya, B. Diaz-Castro, M.R. Gangwani, B.S. Khakh, *J Vis Exp* (2019).
- [47] A.O. Stretton, E.A. Kravitz, *Science* 162 (1968) 132–134.
- [48] Han, M.; Zhao, J.; Fabian, J. M.; Evans, S.; Mustafa, S.; Ruan, Y.; Wiederman, S.; Ebdorff-Heidepriem, H. *Electrophoresis* 2021
- [49] G. Minaschek, J. Bereiter-Hahn, G. Bertholdt, *Exp. Cell Res.* 183 (1989) 434–442.
- [50] V.B. Lu, D.J. Williams, Y.-J. Won, S.R. Ikeda, *Journal of visualized experiments: JoVE* (2009).
- [51] M. Bartoli, W.C. Claycomb, *Mol. Cell. Biochem.* 172 (1997) 103–109.
- [52] R. Gold, *Techniques, Comp. Axon Instruments*, 1993.
- [53] Mobbs, P.; Becker, D.; Williamson, R.; Bate, M.; Warner, A. In *Microelectrode techniques. The plymouth workshop handbook, 2nd ed. Cambridge UK: The Company of Biologists Ltd*; Citeseer, 1994, pp 361–387.
- [54] E. Tekle, R.D. Astumian, P.B. Chock, *Biochem. Biophys. Res. Commun.* 172 (1990) 282–287.
- [55] F.O. Laforge, J. Carpino, S.A. Rotenberg, M.V. Mirkin, *Proc. Natl. Acad. Sci.* 104 (2007) 11895–11900.
- [56] P. Lalley, M. In *Modern Techniques in Neuroscience Research*, Springer (1999) 193–212.
- [57] S.L. Moya, B. Diaz-Castro, M.R. Gangwani, K.B.S. JoVE, (*Journal of Visualized Experiments*) (2019) e60225.
- [58] S.D. Wiederman, J.M. Fabian, J.R. Dunbier, D.C. O'Carroll, *Elife* 6 (2017) e26478.
- [59] M. Ulusoy, R. Jonczyk, J.-G. Walter, S. Springer, A. Lavrentieva, F. Stahl, M. Green, T. Scheper, *Bioconjug. Chem.* 27 (2016) 414–426.
- [60] Harris, J. M. *Poly (ethylene glycol) chemistry: biotechnical and biomedical applications*; Springer Science & Business Media, 1992
- [61] J. Piehler, A. Brecht, R. Valiokas, B. Liedberg, G. Gauglitz, *Biosens. Bioelectron.* 15 (2000) 473–481.

- [62] Y. Du, Y. Zhong, J. Dong, C. Qian, S. Sun, L. Gao, D. Yang, *RSC Adv.* 9 (2019) 12218–12225.
- [63] M. Ali, D. Zayed, W. Ramadan, O.A. Kamel, M. Shehab, S. Ebrahim, *International Nano Letters* 9 (2019) 61–71.
- [64] B. Pelaz, P. del Pino, P. Maffre, R. Hartmann, M. Gallego, S. Rivera-Fernandez, J. M. de la Fuente, G.U. Nienhaus, W.J. Parak, *ACS Nano* 9 (2015) 6996–7008.
- [65] N. Tarantino, J.-Y. Tinevez, E.F. Crowell, B. Boisson, R. Henriques, M. Mhlanga, F. Agou, A. Israël, E. Laplantine, *J. Cell Biol.* 204 (2014) 231–245.
- [66] D. Ernst, J. Köhler, *PCCP* 15 (2013) 3429–3432.
- [67] F. Verpillat, F. Joud, P. Desbiolles, M. Gross, *Opt. Express* 19 (2011) 26044–26055.
- [68] X. Michalet, *Phys. Rev. E* 82 (2010) 041914.
- [69] D. Ernst, J. Köhler, *Phys. Chem. Chem. Phys.* 15 (2013) 845–849.
- [70] S. Wäldchen, J. Lehmann, T. Klein, S. Van De Linde, M. Sauer, *Sci. Rep.* 5 (2015) 15348.
- [71] J. Ge, D.K. Wood, D.M. Weingeist, S. Prasongtanakij, P. Navasumrit, M. Ruchirawat, B.P. Engelward, *Cytometry Part A* 83 (2013) 552–560.
- [72] C. Kielbassa, L. Roza, B. Epe, *Carcinogenesis* 18 (1997) 811–816.
- [73] M. Pflaum, O. Will, B. Epe, *Carcinogenesis* 18 (1997) 2225–2231.
- [74] Yaghini, E.; Seifalian, A. M.; MacRobert, A. J. **2009**.
- [75] J.M. McCord, *The American journal of medicine* 108 (2000) 652–659.
- [76] K. Luby-Phelps, In *International review of cytology*, Elsevier (1999) 189–221.
- [77] P. Hansma, B. Drake, O. Marti, S. Gould, C. Prater, *Science* 243 (1989) 641–643.
- [78] Y.E. Korchev, J. Gorelik, M.J. Lab, E.V. Sviderskaya, C.L. Johnston, C.R. Coombes, I. Vodyanoy, C.R. Edwards, *Biophys. J.* 78 (2000) 451–457.
- [79] B. Alberts, A. Johnson, J. Lewis, M. Raff, K. Roberts, P. Walter, *Molecular Biology of the Cell*, 4th edition, Garland Science, 2002.
- [80] F.G. Donnan, *J. Membr. Sci.* 100 (1995) 45–55.
- [81] B.S. Elkin, M.A. Shaik, B. Morrison III, *Philosophical Transactions of the Royal Society A: Mathematical, Physical and Engineering Sciences* 368 (2010) 585–603.
- [82] K. Strange, *Adv. Physiol. Educ.* 28 (2004) 155–159.
- [83] J. Zhang, Y. Wang, Z. Zheng, X. Sun, T. Chen, C. Li, X. Zhang, J. Guo, *Redox Biol.* 21 (2019) 101112.
- [84] Janmey, P. A.; Cunningham, C. C.; Oster, G. F.; Stossel, T. P. In *Mechanics of Swelling*; Springer, 1992, pp 333–346.
- [85] E. Evans, In *Mechanics of Swelling*, Springer (1992) 293–313.
- [86] Fulda, S.; Gorman, A. M.; Hori, O.; Samali, A. *International journal of cell biology* **2010**, 2010.
- [87] N. de Jonge, D.B. Peckys, *ACS Nano* 10 (2016) 9061–9063.
- [88] K. Luby-Phelps, *Mol. Biol. Cell* 24 (2013) 2593–2596.
- [89] R.P. Sear, *J. Phys.: Condens. Matter* 17 (2005) S3587.
- [90] R.E. Thompson, D.R. Larson, W.W. Webb, *Biophys. J.* 82 (2002) 2775–2783.
- [91] D.J. Smith, *Mater. Today* 12 (2010) 10–16.
- [92] M. Mazzanti, J.O. Bustamante, H. Oberleithner, *Physiol. Rev.* 81 (2001) 1–19.
- [93] R. Brown, *The philosophical magazine* 4 (1828) 161–173.
- [94] W. Liu, A.B. Greytak, J. Lee, C.R. Wong, J. Park, L.F. Marshall, W. Jiang, P.N. Curtin, A.Y. Ting, D.G. Nocera, *J. Am. Chem. Soc.* 132 (2010) 472–483.
- [95] S. Courty, C. Luccardini, Y. Bellaiche, G. Cappello, M. Dahan, *Nano Lett.* 6 (2006) 1491–1495.
- [96] J. Yoo, T. Kambara, K. Gonda, H. Higuchi, *Exp. Cell Res.* 314 (2008) 3563–3569.
- [97] M. Monici, *Biotechnol. Annu. Rev.* 11 (2005) 227–256.
- [98] J. Hanne, H.J. Falk, F. Görlitz, P. Hoyer, J. Engelhardt, S.J. Sahl, S.W. Hell, *Nat. Commun.* 6 (2015) 1–6.
- [99] J. Park, H. Park, P. Ercius, A.F. Pegoraro, C. Xu, J.W. Kim, S.H. Han, D.A. Weitz, *Nano Lett.* 15 (2015) 4737–4744.

Supporting Information for:
Controlled delivery of quantum dots using microelectrophoresis technique: intracellular behavior and preservation of cell viability

Mengke Han,^{1,2} Samuel Evans,^{2,3} Sanam Mustafa,^{2,3} Steven Wiederman^{2,3} and Heike Ebendorff-Heidepriem^{1,2,*}

¹ Institute for Photonics and Advanced Sensing (IPAS) and School of Physical Sciences, The University of Adelaide, Adelaide, South Australia 5005, Australia.

² ARC Centre of Excellence for Nanoscale BioPhotonics (CNBP), The University of Adelaide, Adelaide, South Australia 5005, Australia.

³ Adelaide Medical School, The University of Adelaide, Adelaide, South Australia 5005, Australia.

* Correspondence should be addressed to the following author:

Heike Ebendorff-Heidepriem (Professor)

School of Physical Sciences

Institute for Photonics and Advanced Sensing

The University of Adelaide, Adelaide, South Australia 5005, Australia

heike.ebendorff@adelaide.edu.au

- 1. Cell viability test and cell necrosis caused by excessive irradiation.**
- 2. Size distribution of QDs fluorescent spots for tracking.**
- 3. Spectral imaging via λ -stack function.**
- 4. The caption of supplementary movie.**

1. Cell viability test and cell necrosis caused by excessive irradiation.

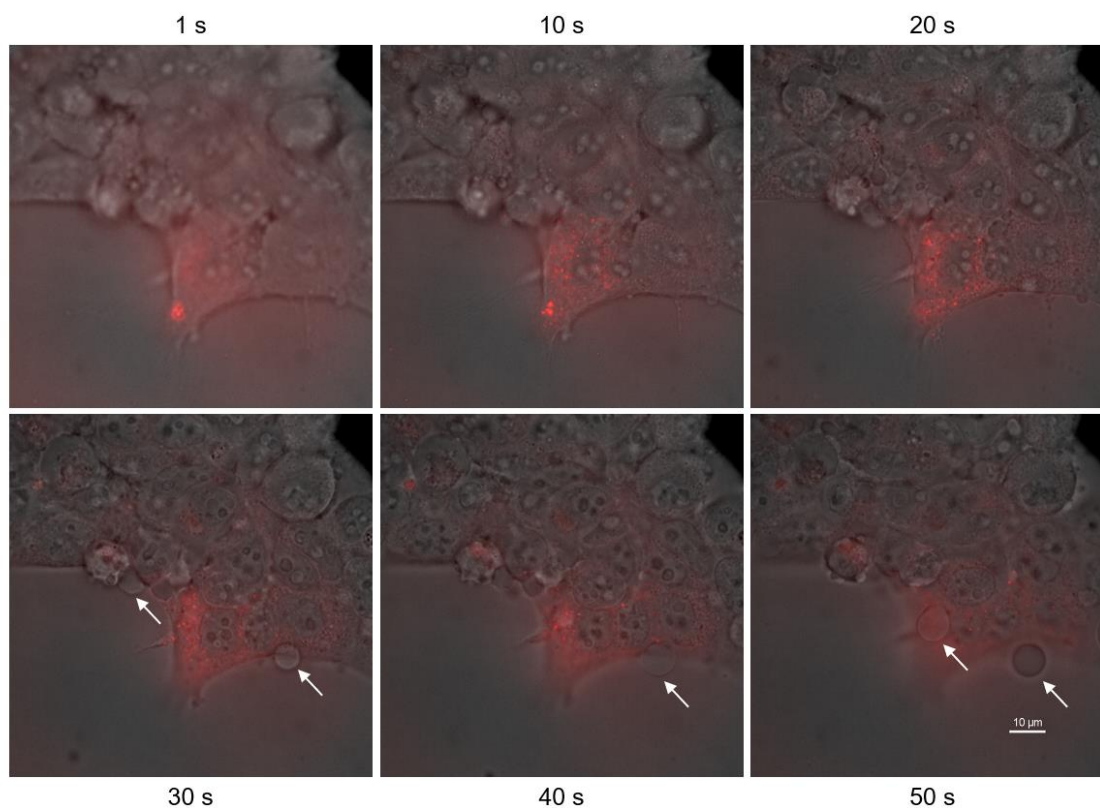


Figure S1 During z-stack image acquisition of a QDs-delivered cell using fluorescent live cell microscopy, the excessive 440 nm excitation light caused cell necrosis over time. Necrosis-induced large blebs on the surface of treated cell and its neighbours were indicated by white arrows. Scale bar, 10 μm.

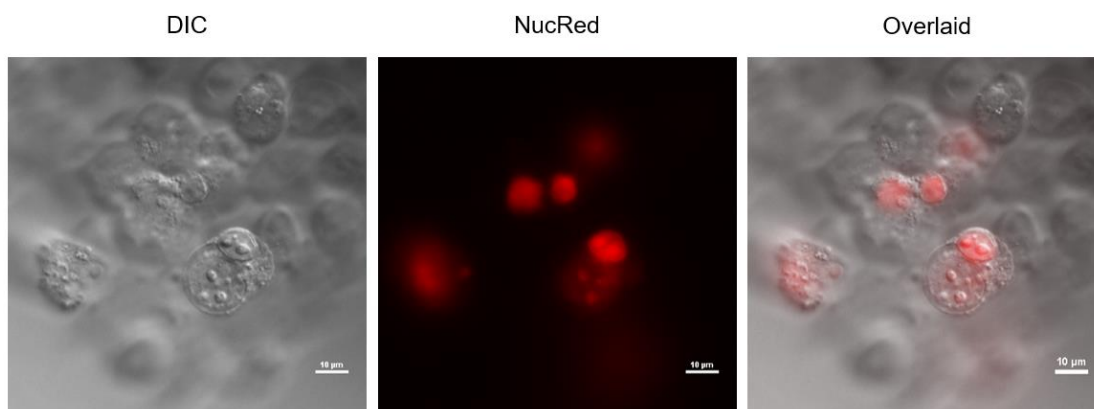


Figure S2 An example of dying cells left at room temperature for 5 hours where the nucleus was stained with NucRed Dead 647 reagent. Scale bar, 10 μm.

2. Size distribution of QDs fluorescent spots for tracking.

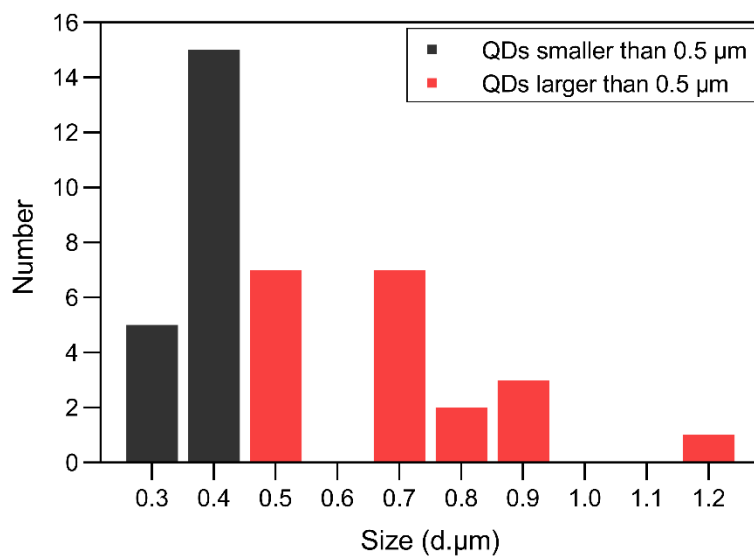


Figure S3 Size distribution of QDs fluorescent spots for tracking inside live HEK293 cells (5 cells, 20 spots for each group).

3. Spectral imaging via λ -stack function.

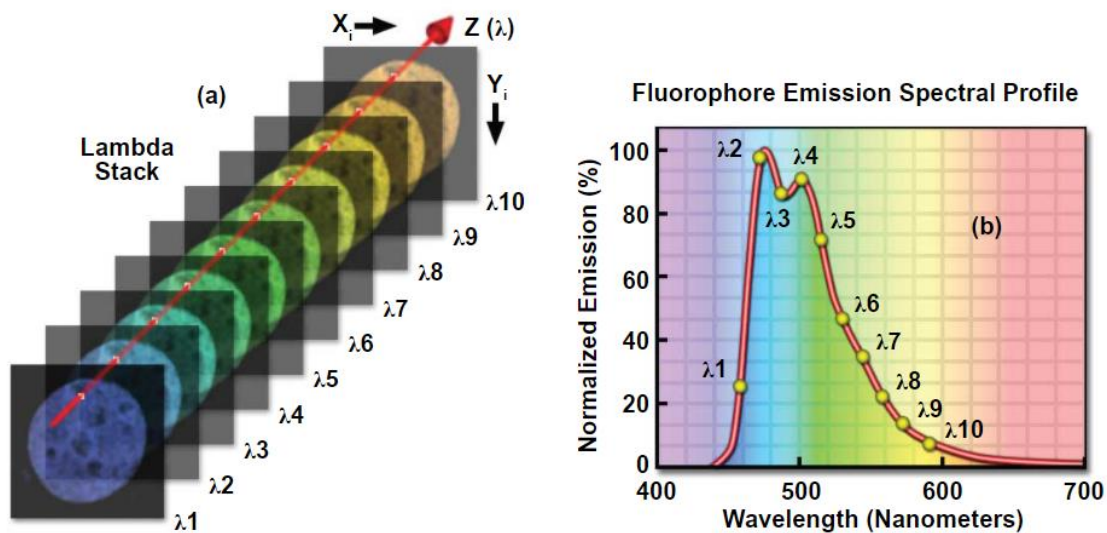


Figure S4 (a) The intensity and/or color of the pixel i changes as a function of fluorescence emission signal strength and wavelength, respectively, when monitored from one end of the λ -stack to the other. (b) By plotting pixel intensity versus wavelength on a linear graph, the emission spectral profile of the fluorophore spatially located at pixel i can readily be determined. Modified according to the online resource from Nikon instruments, (<https://www.microscopyu.com/techniques/confocal/spectral-imaging-and-linear-unmixing>).

4. The caption of supplementary movie.

The movie shows the random motion of QDs clusters inside the cytoplasm of a treated cell. The movie was captured and played at 1 fps.

3.4 Intracellular delivery of quantum dots into SH-SY5Y cells

To test the applicability of microelectrophoresis technique to other cell types, the popular SH-SY5Y neuroblastoma cell line was used to demonstrate the intracellular delivery of QDs as well. SH-SY5Y cell line is widely used in Parkinson's disease research.¹ Primary mammalian neurons derived from embryonic central nervous system tissue have limitations in practical applications. Once these primary neurons are terminally differentiated into mature neurons, they are not able to be propagated.² Transformed neuronal-like cell lines, such as the SH-SY5Y cells used here, can overcome this limitation.³ This cell line is frequently chosen because of its human origin (a metastatic bone tumor biopsy) and ease of maintenance.⁴ All the operations for QDs delivery were identical to that been done to HEK293 cells, except that the cell culture procedure was different as shown below:

Cell culture conditions: SH-SY5Y cells were maintained in Dulbecco's modified Eagle's medium (DMEM) supplemented with 4.5 g/L glucose, 10% w/v Fetal Bovine Serum, 2 mM L-Glutamine, 1 x non-essential amino acid solution. Plated into ibidi dishes at 60,000 cells/dish in

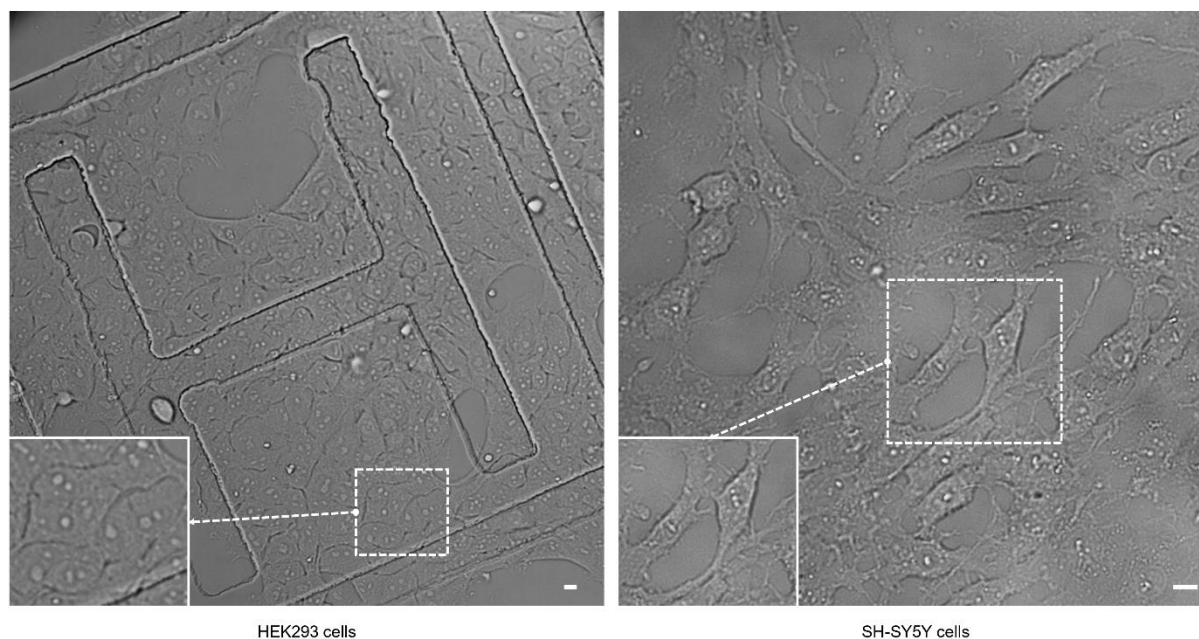


Figure 9 DIC images of HEK293 and SH-SY5Y cells. Scale bar, 10 μ m. Magnified insets (left bottom) show the morphological differences between HEK293 and SH-SY5Y cells in the areas outlined by white dash lines.

growth media. After 48 hours, 1.5 mL imaging media (1:1 maintenance media supplemented with 25 mM HEPES and PRF DMEM supplemented with 1 x non-essential amino acid (NEAA) was added. Cells were returned to incubator before imaging. PRF DMEM: Dulbecco's modified Eagle's medium (DMEM), high glucose, HEPES, no phenol red.

There are significant morphological differences between HEK293 and undifferentiated SH-SY5Y cells (Figure 9). HEK293 cells are epithelial-like cells, exhibiting polygonal shape with regular dimensions, whereas SH-SY5Y cells are fibroblast-like cells, presenting elongated shape and branching projections. Considering the appearance of SH-SY5Y cells, the longest ejection duration of 3 mins was used to ensure the highest possible loading of QDs for filling the distal ends and the strongest fluorescence signals to be detected (Figure 10). Delivered QDs evenly distributed throughout the cytoplasm and spread into the projections. In all 10 treated cells, two of them survived the 24 hours incubation where QDs remained within the cytoplasm after cell fixation, whereas others died with obvious morphological changes. Although Cell 2 survived the 3 mins loading of QDs, it had a significant morphological change and shrunk into spherical shape. These preliminary results proved again that the retention of cell viability was largely due to the reduced

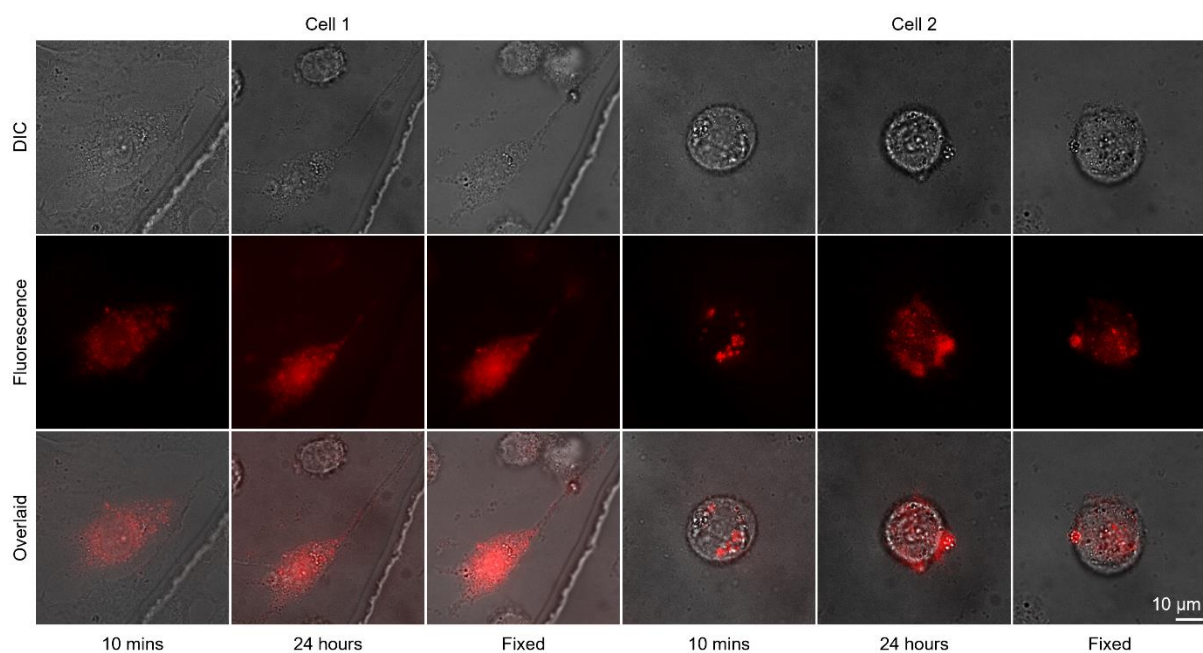


Figure 10 DIC, fluorescence and overlaid images of two SH-SY5Y cells with microelectroforetic-delivered QDs under a constant current of - 0.2 nA for 3 mins (n = 10 in 3 independent experiments). Scale bar, 10 µm.

loading of QDs, which avoided the undesirable perturbation to the intracellular environment. Therefore, the ejection duration needs to be finely optimized for any given cell type. Nevertheless, it has been demonstrated here that microelectrophoresis technique can be readily applied to other cell types. The induction of differentiation in SH-SY5Y cells, commonly through the addition of retinoic acid, will be the subject of a future work, where they possess a more mature, neuron-like phenotype.² The optimization of loading conditions and post-injection cell viability assays for differentiated SH-SY5Y cells would greatly facilitate the intracellular delivery of QDs into neurons.

3.5 References

1. Xicoy, H.; Wieringa, B.; Martens, G. J. M., The Sh-Sy5y Cell Line in Parkinson's Disease Research: A Systematic Review. *Mol Neurodegener* **2017**, *12* (1), 10-10.
2. Kovalevich, J.; Langford, D., Considerations for the Use of Sh-Sy5y Neuroblastoma Cells in Neurobiology. *Methods Mol Biol* **2013**, *1078*, 9-21.
3. Constantinescu, R.; Constantinescu, A. T.; Reichmann, H.; Janetzky, B., Neuronal Differentiation and Long-Term Culture of the Human Neuroblastoma Line Sh-Sy5y. *J Neural Transm Suppl* **2007**, (72), 17-28.
4. Buttiglione, M.; Vitiello, F.; Sardella, E.; Petrone, L.; Nardulli, M.; Favia, P.; d'Agostino, R.; Gristina, R., Behaviour of Sh-Sy5y Neuroblastoma Cell Line Grown in Different Media and on Different Chemically Modified Substrates. *Biomaterials* **2007**, *28* (19), 2932-45.

CHAPTER 4 CONCLUSIONS

CONTENTS

4.1	Potential of microelectrophoretic delivered nanomaterials in voltage imaging.....	90
4.2	Future directions.....	92
4.3	References	94

4.1 Potential of microelectrophoretic delivered nanomaterials in voltage imaging

The ability to selectively stain a single neuron via the intracellular delivery of optical voltage sensors is of crucial importance in studying its extremely complex functions. Microelectrophoresis technique has long been an effective method for introducing VSDs into single neurons. Delivered VSDs are able to spread into branching neuronal processes and the finest neuronal structures, such as dendritic spines, where the signal integration is often accomplished. These amphiphilic VSDs then spontaneously insert into the plasma membrane bilayer, making the multisite voltage imaging over the whole structure of the neuron possible. The first part of this thesis is the initial attempt to systematically study the feasibility of adapting microelectrophoresis technique for the intracellular delivery of VSM (QDs used as an example). Though nanomaterials possess superior optical and biocompatible properties surpassing VSDs, their relatively larger sizes and colloidal instability make the requirements for successful microelectrophoresis considerably more demanding than that of VSDs.

In Chapter 2, an optimal protocol was designed to prepare the QDs suspension, by which QDs attained high surface charges to repel each other and monodisperse without aggregation. The low KCl concentration required for maintaining the colloidal stability of QDs enabled the high-quality intracellular recordings to locate the target cells. It is noteworthy that this protocol can preserve the colloidal stability of QDs for at least 24 days, which is beneficial for its practical application. This protocol provides a general solution to the preparation of other types of nanomaterials, where the pH and KCl concentration are the core considerations. Charged QDs were successfully loaded into live HEK293 cells by a mild electrical current (-0.2 nA) through micropipettes with suitable tip sizes around 200 nm, being large enough for the ejection of QDs having ~ 30 nm hydrodynamic diameters and less than 500 nm, the rule of thumb to avoid mechanical damage to live cells.

With all these key parameters optimized and the feasibility verified, in Chapter 3, following-up investigations were made on the ability of microelectrophoresis technique to control the loading dose of QDs, its subsequent impact on cell viability, and the intracellular fate of these delivered QDs. The phenomena observed here in these studies strongly support the potential applicability of

microelectrophoresis technique in the nanomaterials-mediated voltage imaging of single neurons, where certain critical requirements have been met.

First, internally loaded voltage sensors should diffuse readily throughout the soma and spread into the thin axonal and dendritic processes. Here, facilitated by electrical current, QDs were able to quickly fill the cytoplasm and reach the furthest cell boundary within 3 mins, demonstrated in both HEK293 and SH-SY5Y cells. In addition, compared to the prolonged staining via free diffusion and microinjection, the short durations of electrophoretic forces (≤ 3 mins) avoid the excessive physical damage caused by micropipettes to treated cells.

Second, intracellular voltage sensors should self-insert into the plasma membrane bilayer. Here, limited by the access to membrane-targeted QDs, commercially available QDs with surface functionalization of amine-derivatized PEG were used as prototypes for feasibility test without specific targeting functions. The analysis of intracellular dynamics of these non-targeted QDs reveals that smaller-sized QDs clusters (< 500 nm) are freely diffusing within the cytoplasm, presenting higher MSD than that of larger clusters, which are prone to be spatially confined by intracellular obstacles. Limited by the resolution of fluorescence microscopy used here, the trajectories of single QDs are not obtainable and thus they are presumed to be readily diffusing in a larger spatial extent. These results implicate that single membrane-targeted QDs, internally loaded via microelectrophoresis technique, would freely diffuse throughout the cytoplasm and exploit their amphiphilicity to spontaneously insert into the membrane bilayer, whereas the large-sized clusters would be stationary as background signals.

Third, delivered voltage sensors should retain within the neuron without appreciable leakage. Here, after 24 hours incubation, microelectrophoretic delivered QDs still reside within HEK293 and SH-SY5Y cells, where no evident leakage has been observed nor photobleaching. This would significantly extend the experimental duration.

Finally, delivered voltage sensors should not lead to toxic effect. Here, cell viability is largely determined by the loading dose of QDs relative to cell sizes. Proper loading of QDs can preserve

cell health as well as proliferation, whereas excessive loading tends to cause dramatic cell death. Depending on the length of neuronal processes, microelectrophoresis technique would enable the fine-tuning of the loading dose of VSM, preserving the cell viability to the largest extent without altering normal neuronal functions.

Overall, this series of work contributes key information and original findings that encourage the future implementation of microelectrophoresis technique in the intracellular loading of VSM, offering a new path for the robust optical visualization of the complex and dynamic electrical activities occurring in single neurons.

4.2 Future directions

In light of the exciting and promising results above, it is anticipated that these non-targeted QDs will be reliably delivered into neuronal-like cells, e.g., differentiated SH-SY5Y and self-spiking HEK293 cells, and further into single neurons in brain slices or brain tissues in animal models using microelectrophoresis technique, which should be the next priority research interests. The featured two-photon absorption coefficients of QDs, which is 10 to 1,000 times larger than those of VSDs and fluorescent proteins,¹ would be an outstanding characteristic that is beneficial to deeper brain tissue imaging. More importantly, it has been reported that the electric field sensitivities of type I QDs and quasi type II NRs are enhanced under two-photon excitation compared to single-photon excitation.² In addition, two-photon excitation at near-infrared wavelengths for thick tissue penetration reduces the impact of photodamage and thus enables the investigation of subsurface neurons over longer time periods. Meanwhile, it remains to be seen whether membrane-targeted QDs can be spontaneously insert into the plasma membrane bilayer after microelectrophoretic delivery. The cell membrane is complicated, dynamic, heterogeneous, and variable in composition across cell types. Although special amphiphilic peptides and pure lipids coating have been reported as viable strategies to facilitate the self-insertion of rod-shaped QDs into the membrane, there is still significant room for improvement in the orientation and retention of these membrane-targeted QDs for robust membrane voltage sensing. Moreover, with the general guideline to prepare nanomaterials suspension provided in this thesis, another research

focus would be to expand the deliverable nanomaterials list, such as NDs and other potential nano voltage sensors in the future.

To minimize the photodamage to live cells, the investigation on the intracellular fate of delivered QDs was performed here using fluorescence microscopy with the highest spatial resolution of 0.13 μm per pixel, which was not sufficient to reveal individual QDs having hydrodynamic diameters between 10 to 35 nm. The accurate description of the dispersity of delivered nanomaterials inside the cytoplasm is expected to be achievable with the use of super resolution microscopy or live cell TEM in the future. Meanwhile, for now, aggregation is a ubiquitous and inevitable phenomenon among all nanomaterials in biological studies, which could turn them into nonfunctional states. The exposure to high concentration of ions decreases the screening length of charged chemical groups on the nanomaterials surface and reduces their electrostatic repulsive force. The nonspecific adsorption of biomolecules, predominantly proteins, can also affect the dispersity of nanomaterials. In this work, QDs are purely encapsulated with amine-derivatized PEG polymers to provide colloidal stability and are nontargeted to any designated site of action. Thus, they will eventually aggregate in the complex intracellular environment. The result of size distribution analysis of delivered QDs is as expected, where they are aggregated into clusters within the range of 0.3 to 0.7 μm . Thus, the optimization of nanomaterials themselves, including surface functionalization, shape, size and chemical composition, is the key in improving their dispersity in biological applications.

Future progress in nanotechnology is predicted to catalyze creative ideas and breakthroughs for the revolution in neuroscience. If all the considerations discussed above are properly addressed, VSM could present far better performance than current sensors to advance our understanding of the brain. Applying nanomaterials for in vivo brain imaging and disease diagnosis in human will remain extremely challenging and continue to be a long-term goal. In the near future, nanomaterials-mediated voltage imaging would be able to monitor neuronal activities in relevant animal models and uncover the mysteries of the brain that are impossible to be answered previously.

4.3 References

1. Resch-Genger, U.; Grabolle, M.; Cavaliere-Jaricot, S.; Nitschke, R.; Nann, T., Quantum Dots Versus Organic Dyes as Fluorescent Labels. *Nat Methods* **2008**, *5* (9), 763-75.
2. Jooen, S.; Coene, Y. d.; Deschaume, O.; Zámbo, D.; Aubert, T.; Hens, Z.; Dorfs, D.; Verbiest, T.; Clays, K.; Callewaert, G.; Bartic, C., Enhanced Electric Field Sensitivity of Quantum Dot/Rod Two-Photon Fluorescence and Its Relevance for Cell Transmembrane Voltage Imaging. *Nanophotonics* **2021**, *10* (9), 2407-2420.

Part II Voltage sensitivity of nanomaterials

CONTENTS

Chapter 5	Introduction.....	96
Chapter 6	Methods	121
Chapter 7	Sandwich device characterization.....	125
Chapter 8	Conclusions.....	131

CHAPTER 5 INTRODUCTION

CONTENTS

5.1	Physical origin of nanomaterials' voltage sensitivity	97
5.1.1	Quantum dots	97
5.1.2	Nanodiamonds	102
5.2	Characterizing the response of nanomaterials upon external voltage modulation.....	107
5.2.1	Quantum dots	107
5.2.2	Nanodiamonds	111
5.3	Part II aims and scope.....	113
5.4	References	114

5.1 Physical origin of nanomaterials' voltage sensitivity

5.1.1 Quantum dots

When direct-gap semiconductors absorb a photon, an electron is excited from the valence band into the conduction band. In this process, an electron-hole pair (i.e., exciton) is created in the bulk materials. It is a hydrogenic-like bound state that forms due to the Coulombic attraction between

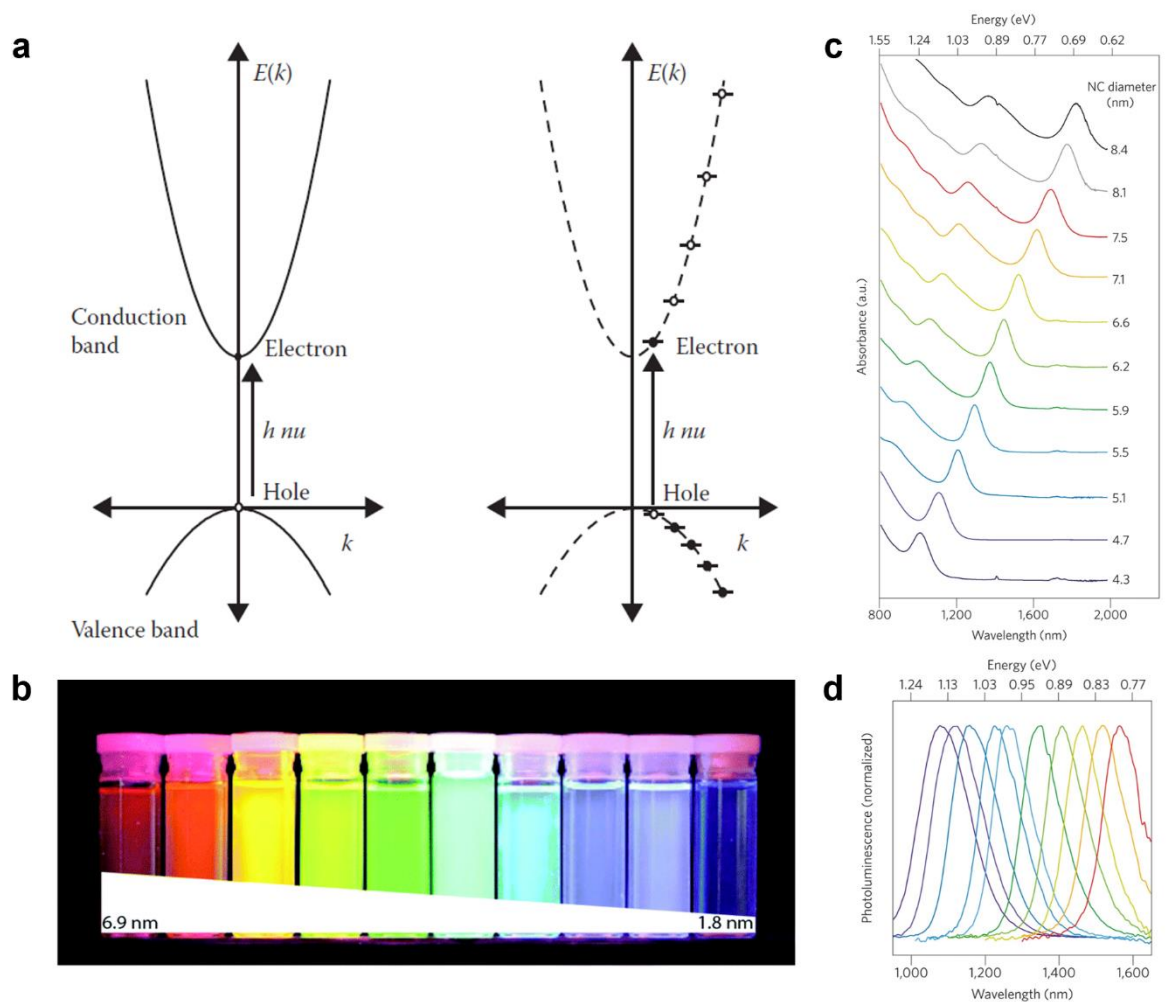


Figure 11 (a) Comparison between the band diagram for direct gap bulk semiconductors (left) and the quantization of the bulk bands, which induces the discrete optical transitions in finite size semiconductor nanocrystals (right). (b) Distinguishable emission colors of CdSe/ZnS QDs having different sizes excited with a near-UV lamp. (c) and (d) The absorption and PL spectra measured at 10 K in PbS QDs with diameters varying from 4.3 to 8.4 nm. Colours are the same in (c) and (d). Reproduced from references 2, 3, and 4.

the electron and hole.¹ As semiconductors shrink into the nanoscale, especially comparable to or smaller than the natural length of the exciton (i.e., Bohr's radius of the bulk materials), where charge carriers (electrons and holes) are confined in all three dimensions (QDs), the quantum size effect occurs with unique electronic properties emerging. In contrast to the continuous energy values in bulk materials, in QDs, the valence and conduction bands are discrete and quantized into a ladder of energy levels for the hole and electron (Figure 11a).² Therefore, the absorption spectra of bulk semiconductors is continuous above the band gap, whereas the spectra of QDs has a series of discrete electronic transitions between these quantized levels (Figure 11b).³ In addition, the band gap of QDs is dependent on the degree of spatial confinement and thus their emission spectra are size-tunable (Figure 11c, d).⁴

When an electric field is applied to QDs, energy levels within the valence and conduction bands shift towards higher and lower values, and this phenomenon is referred to as the quantum-confined Stark effect (QCSE, Figure 12).^{5,6} It effectively reduces the band gap of QDs and leads to a redshift in the emission spectra, with the shift magnitude proportional to the square of the electric field.¹ It also causes the polarization of charge carriers, i.e., the electron and hole in the exciton, that opposes the external electric field, leading to the reduction in the overlap integral between the wavefunction of the electron (Ψ_e) and hole (Ψ_h). This increases the radiative lifetime (τ_r) of QDs that is inversely

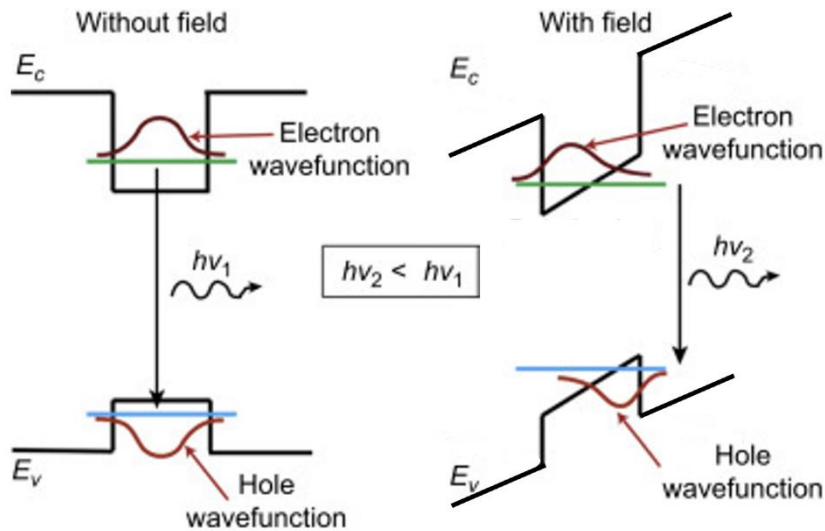


Figure 12 The strong electric-field shift of the electron and hole wavefunctions in opposite directions within the QDs. This results in a red shift of the QD PL referred to as the quantum-confined Stark effect (QCSE). Reproduced from reference 5.

proportional to the overlap between the electron and hole wavefunctions, $\tau_r \propto |\langle \Psi_e | \Psi_h \rangle|^{-2}$, and hence raises the fraction of excitation events that produce nonradiative decay, giving rise to the reduction in quantum yield and consequently a dimming of fluorescence intensity and broadening of PL spectra.

Besides the decrease in radiative decay rate, the increase in ionization probability of QDs upon the application of electric field also contributes to their PL quenching. In the absence of electric field, QDs ionization is the reason for the recurring intermittency in their emission,⁷⁻¹⁰ which is known as blinking (Figure 13a).^{11, 12} One of the photoexcited carriers (electron or hole) could be either thermally ejected from the core to the QD surface, or via Auger ionization and direct quantum mechanical tunnelling, with the remaining carrier residing in the core.^{13, 14} Upon photoexcitation, the annihilation energy generated from the recombination of another exciton is transferred to this remaining carrier, leading to non-radiative Auger recombination. The time of non-radiative Auger recombination is on the order of 10 - 100 ps, which is much shorter than the radiative decay time

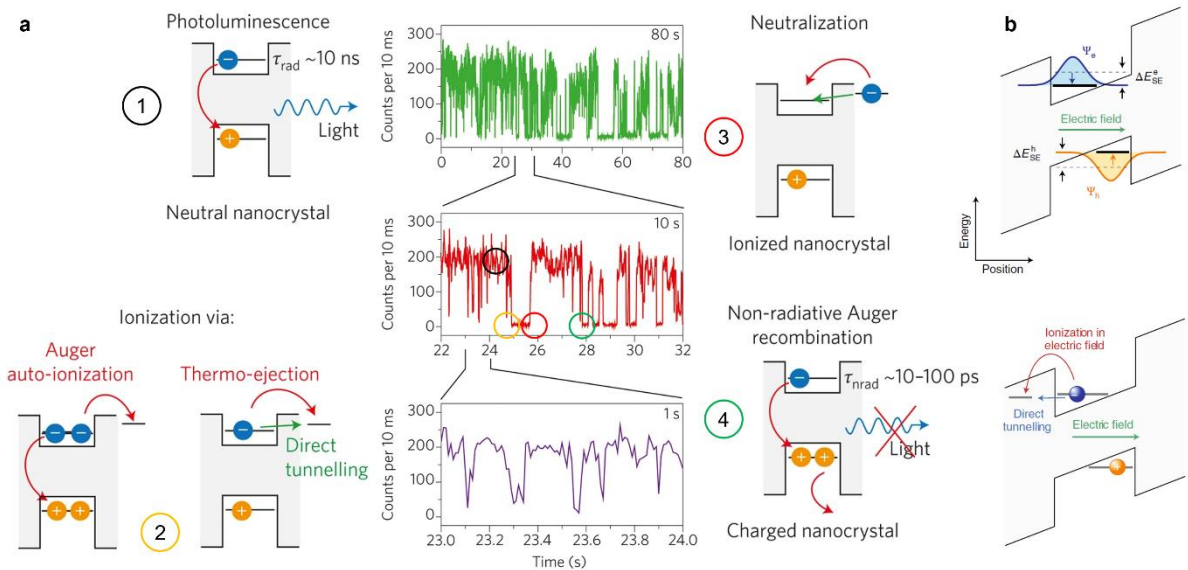


Figure 13 (a) Time trace of a single ~ 2.9 nm radius CdSe QD showing blinking over a sequence of three expanded timescales. Optical excitation of the neutral QD leads to PL with a radiative decay time on the order of 10 ns. Excitation of the charged QD leads to fast non-radiative Auger recombination with a decay time on the order of 10 - 100 ps. The circles with different colors correspond to the processes that lead to and the phenomena that control the fluorescence trajectory. (b) The number of ionized QDs in an ensemble increases with electric field because it decreases the confining barriers for both electrons and holes, increasing the probability of QD ionization, resulting in a corresponding decrease in PL intensity. Reproduced from references 11, 12, and 15.

of 10 - 100 ns and thus the PL of ionized QDs is completely or partly quenched. After some period of time, the ejected carrier returns to the core and restores the neutrality and radiative decay of QDs. The external electric field increases the probability for the ejection of charge carriers to the QDs surface, which lies in the reduction in the Coulomb interaction between the electrons and holes, resulting in a corresponding decrease in PL intensity (Figure 13b and c).¹⁵

The voltage sensitivity of QDs, i.e., the magnitude of QCSE and ionization probability, is determined by their composition, size, band structure and shape. The composition determines the effective mass of the charge carriers. The larger effective mass leads to the lower energy, making the carriers more susceptible to external perturbations, i.e., the higher polarizability and thus greater sensitivity to electric field. The size of QDs determines the maximum distance between the charge carriers, where longer distance reduces the Coulomb interaction and thus increases the magnitude of QCSE.

For core/shell QDs, the band structure of the shell with respect to that of the core determines how the charge carriers are confined, and thus affects the strength of Coulomb interaction between them, i.e., the polarizability (Figure 14a).¹⁶ In type I QDs, the shell has wider band gap than the core and thus the charge carriers remain confined to the core.¹⁷ In quasi type II QDs, the shell has a slightly larger band gap than the core, with only a small offset between the conduction or valence bands.¹⁸ Therefore, one charge carrier delocalizes over the entire structure while the other remains confined to the core.¹⁹ In type II QDs, though the core and shell have a similar band gap, the shell has either higher or lower energy than that of the core. Therefore, one charge carrier relocates towards the shell, while the other remains confined to the core. The band structure of type II QDs allows for the largest separation between the charge carriers and hence the highest sensitivity to voltage changes.

Practically, the wavelength shift of type I and quasi type II QDs is quite similar under electric fields. However, the band structure of QDs also plays an important role in the suppression of non-radiative Auger recombination during the blinking phenomenon. It has been reported that type I

shows a moderate emission intensity quenching of 22%, whereas quasi type II QDs drastically quenched 63% under a 500 kV/cm electric field.²⁰

Although composition, size, and band structure of QDs all contribute to the voltage sensitivity, their impacts are weak compared to that of the QDs shape.²¹ Both theoretical and experimental studies show that type II nanorods (NRs) having a spherical core inside an elongated shell, and other asymmetric semiconductor nanocrystals, are generally more sensitive to electric fields than spherical QDs, due to enhanced separation between the charge carriers (Figure 14b).^{16, 22} In addition, as the exciton is a permanent electric dipole, the wavelength shift of asymmetric type II NRs is approximately in linear relationship with the voltage changes, whereas the wavelength shift of spherical QDs has a quadratic dependence on the voltage changes.²² Most importantly, the relative orientation between NRs and electric field determines whether the emission peak shifts to shorter or longer wavelengths.²² Therefore, asymmetric NRs are sensitive to the direction of the electric field. This distinguished feature makes them ideal for sensing membrane potential changes, as they can report the inversion of membrane potential, i.e., from -70 mV to 30 mV, whereas symmetrical particles can only sense the difference between the absolute values of 40 mV.

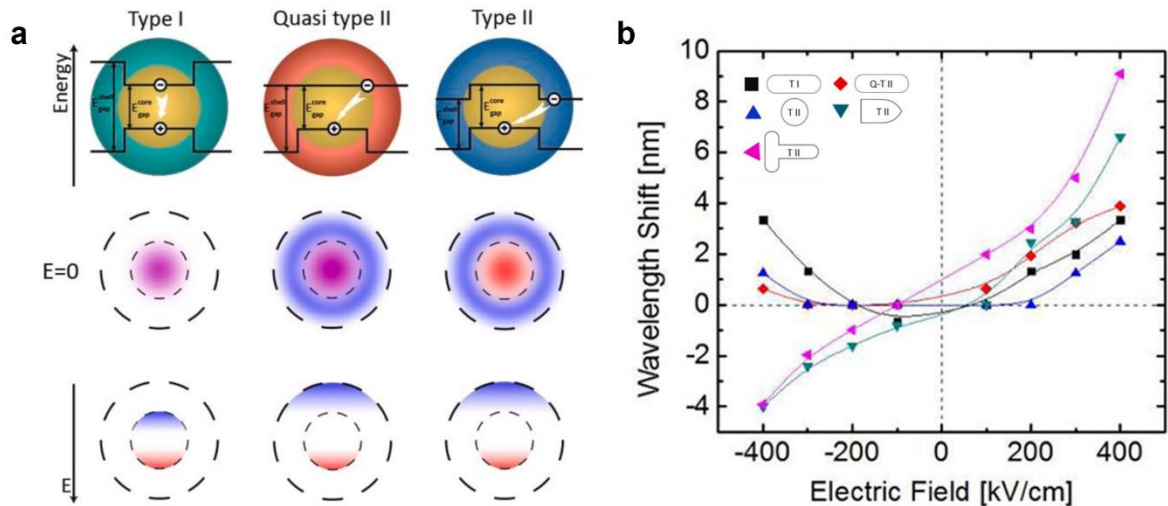


Figure 14 (a) Top: types of core/shell semiconductor nanostructures depending on the confinement of the charge carriers. Middle: Distribution of the charge carriers in semiconductor nanostructures when no electric field is applied. Bottom: distribution of the charge carriers within semiconductor nanostructures under an external electric field. (b) Voltage response of different types of QDs. The shape of the particles is schematically depicted in the legend. Reproduced from references 16 and 22.

All the PL responses of QDs, spectral shift, changes in the emission intensity and excited state lifetime, are electro-optic effects and occur on picosecond time scales, providing high fidelity to track membrane potential changes having millisecond time scales.²⁰ In addition, the large spectral shift of NRs makes the ratiometric measurements at multiple emission wavelengths possible to avoid the noisy intensity change measurements, which provides higher sensitivity to detect minute changes in electrical signals.

The above thorough understanding of the physical origin of QDs voltage sensitivity stems from the dramatic improvements in the synthesis of high-quality QDs, which provide intricate control over the material, size, shape, shell thickness, doping, heterostructure, and band alignment.^{18, 21, 23} This makes the precise engineering of the charge carriers possible to significantly improve their voltage sensitivity.²² In the future, QDs or NRs having sizable responses in fluorescence intensity, lifetime, and emission peak wavelength to electric fields, are promising candidates for monitoring neuronal activity.²⁴

5.1.2 Nanodiamonds

In diamond, impurities refer to one or a few foreign atoms or vacancies that naturally occur in the lattice.²⁵ They produce additional electronic states within the wide band gap of diamond,²⁶ forming fluorescent color centers that absorb and emit light in the visible spectrum.^{27, 28} These color centers are protected within the diamond lattice and thus their optical properties are unprecedentedly stable.^{29, 30} Among the hundreds of different color centers that have been reported, nitrogen vacancy (NV) center that consists of a nitrogen atom, which replaces a carbon atom next to an adjacent empty site in the diamond lattice (Figure 15a),³¹ is the most well studied and has received increasing attention over the past few decades in diverse fields, such as quantum information processing.^{32, 33}

Currently, there are two major routes for nitrogen-containing nanodiamonds (NDs) synthesis, the “bottom-up” method, detonation, and the “top-down” method, high-pressure high-temperature (HPHT).^{25, 34-36} Detonation nanodiamond (DND) is produced by the detonation of a mixture of

carbon-containing and oxygen-deficient explosives, such as trinitrotoluene (TNT) and hexogen (RDX), in a nonoxidizing medium inside closed chambers.^{27, 34, 35} Along with the dropping pressure and temperature, supersaturated carbon vapor from the explosives condenses into liquid droplets and crystallizes to form NDs. DNDs have high nitrogen content up to 2 - 3 wt%, but these nitrogen atoms are primarily in aggregated states, which renders DNDs optically inactive.³⁷ In contrast, HPHT NDs are obtained by crushing micron sized diamonds that grow from carbon sources, such as graphite or diamond powder, together with metal catalysts under high pressure and temperature in a hydraulic press.³⁶ HPHT NDs have nitrogen impurities at the level of 100-200 ppm and are primarily in substitutional states.³⁷ Vacancies can be created by causing radiation damage to the diamond with high-energy particles, including electrons, protons, and He⁺.³⁷ Subsequent annealing treatment at high temperature (> 700 °C) leads to the diffusion of the vacancies towards substitutional nitrogen atoms and forms NV color centers.³⁸⁻⁴⁰ Besides the different content and state of nitrogen impurities, DNDs and HPHT NDs have distinct size and morphology. DNDs are 3 - 5 nm in size and typically spherical in shape. Although the micron sized diamonds (40 - 200 μm) grown via HPHT synthesis are almost perfect polyhedral shapes, the crushing process results in smaller sized particles (available from 10 nm to 100 μm), exhibiting highly irregular shapes, distributed sizes, and sharp facets (Figure 15b).³⁹ Unlike the well-controlled synthesis of QDs, this is the major limitation of using fluorescent HPHT NDs in biological applications, which requires further efforts.^{39, 41, 42}

The NV centers can be converted among three different charge states,⁴³ the neutral NV⁰ state, with a zero-phonon line (ZPL) at 575 nm, the negatively charged NV⁻ state, with a ZPL at 637 nm,

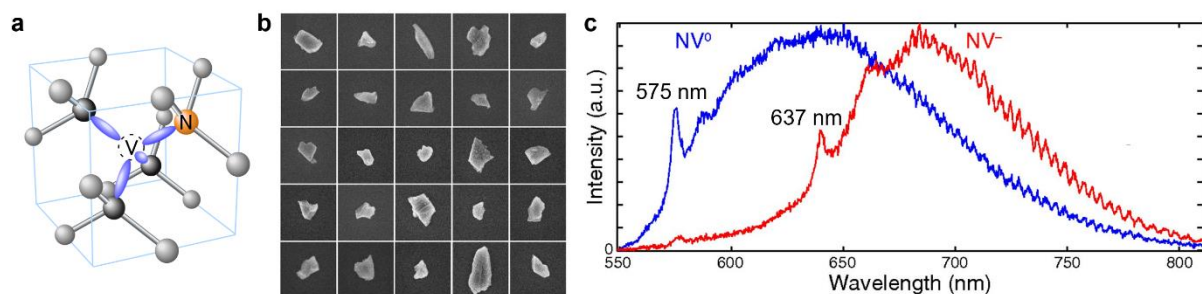


Figure 15 (a) Structure of a NV center comprising a substitutional nitrogen atom and a neighboring vacancy in the diamond lattice. (b) SEM images of 25 fluorescent HPHT NDs. The size of each square is 500 nm × 500 nm. (c) Fluorescence spectrum of NV⁰ (blue curve) and NV⁻ state (red curve). Reproduced from references 31, 32 and 39.

and the positively charged nonfluorescent state NV^+ (Figure 15c).³² The charge state of NV centers depends on the relative position of the Fermi level (E_F) to the charge transition level ($E_{NV^{0/-}}$ and $E_{NV^{+/0}}$), which determines whether the center takes up or loses an electron. For instance, the $NV^{0/-}$ charge transition level marks the transition from the neutral to the negatively charged state. When the Fermi level is above the $NV^{0/-}$ level, an electron is taken up by the center and vice versa.

It has been reported that the surface termination of diamonds strongly affects the charge state of NV centers near the surface.^{44, 45} The C-H bonds of the hydrogen-terminated diamond surface induce an effective surface dipole moment and thus present a negative electron affinity (χ).⁴⁶ When the diamond is in contact with air, a layer of atmospheric adsorbates will form at its surface (Figure 16a).⁴⁷ These adsorbates keep accepting electrons from the valence band and the NV centers in the band gap until the Fermi level of the diamond equilibrates with the surface adsorbate state (μ) (Figure 16b).⁴⁷ The equilibration induces the bending of the conduction and valence bands together with the NV charge state transition levels, $E_{NV^{0/-}}$ and $E_{NV^{+/0}}$. This leads to the formation of a two-dimensional hole gas (2-DHG) in the potential well at the diamond surface, making the hydrogen-terminated diamond conductive. Close to the surface, these transition levels can move above the

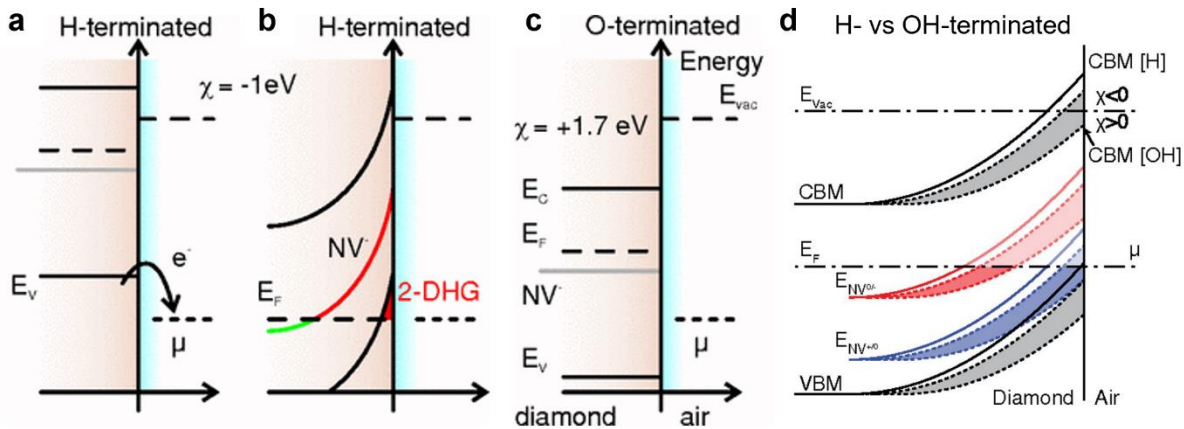


Figure 16 (a) Energy band structure schematic of H-terminated diamond. The bands are shifted upward by the hydrogen termination. Electrons can transfer into the adsorbed layer. (b) A two-dimensional hole gas (2-DHG) is induced at the surface when the equilibrium is established. Close to the surface, the strong band bending modifies the charge states. (c) Energy-band schematic of O-terminated diamond. The conduction band lies below the vacuum level and the NV^- level lies below the Fermi level. (d) Energy band structure schematic showing the band bending near hydrogen (solid) and hydroxyl (dashed) terminated diamond surfaces in atmospheric conditions. Close to the surface, these transition levels can move above the Fermi level (light red and blue lines) and result in a change in the NV charge state depending on their distance to the surface. Reproduced from references 32 and 47.

E_F and results in a change in the NV charge state depending on their distance to the surface.⁴⁸ NV centers that are deep below the surface can be in the negative charge state as the $E_{NV^{0/-}}$ is below the E_F . Near the surface, the $E_{NV^{0/-}}$ level moves above E_F , converting the near-surface NV^- states to NV^0 . The large band bending at hydrogenated surfaces can further convert NV centers closest to the surface from the NV^0 state to the NV^+ state (Figure 16d).³² In contrast, band bending does not occur for strongly oxidized diamond surfaces as they exhibit a large positive electron affinity and near-surface NV centers remain in the negative charge state (Figure 16c).⁴⁷ However, some oxygen surface termination groups, such as hydroxyl, can present either positive or negative electron affinities depending on the type of surface reconstruction and crystallographic orientation of the diamond surface, which can also induce upward band bending in the diamond and affect the NV charge state (Figure 16d).³²

Recent studies show that externally applied electric field across the NDs can induce strong band bending and vary the relative position between the Fermi level and the NV charge state transition levels, causing the switch of the NV charge states and hence fluorescence changes.⁴⁹ The voltage modulation of the charge state and fluorescence of NV centers strongly depends on the surface termination of NDs. Two types of NDs were investigated, hydrogenated NDs (mean size of 12 nm) with primarily hydrogen surface termination groups, and hydroxylated NDs (mean size of 18 nm) with primarily hydroxyl surface termination groups.

For hydrogenated NDs, as introduced above, the NV^0 state predominantly attributes to their PL with negligible contribution from NV^- due to the near-surface band bending. The surface of hydrogen terminated NDs is conductive due to the formation of 2-DHG. When the conductive ND surface is in direct electrical contact with the working electrode (indium tin oxide, ITO), an increase in the applied voltage (Ψ_{app}) across the NDs induces a decrease in NV^0 emission, whereas the PL of NV^- remains unchanged (Figure 17a).³² However, when the conductive ND surface is not in direct electrical contact with the ITO electrode but is deposited on an alumina spacer layer, almost no PL change can be observed. These results indicate that charge transfer between the ITO working electrode and the conductive hydrogenated NDs' surface is the dominant mechanism by which the applied voltage induces band bending, which shifts the NV charge state from NV^0 to the nonfluorescent NV^+ state (Figure 17b).³² Although the applied voltage could also induce band

bending for hydrogenated NDs on the alumina spacer layer, it is screened by the conductive surface surrounding the NDs.

For hydroxylated NDs, the built-in voltage difference between the ITO working electrode and the electrolyte surrounding NDs results in the $E_{NV^{0/-}}$ level being slightly below E_F so that the PL of NV centers are primarily contributed from the neutral charge state (75%) with 25% from the NV^- .³² When the non-conductive ND surface is in direct electrical contact with the ITO working electrode, a decrease in the applied voltage from 0 to -0.75 V leads to an increase in the total PL of 24% while the contribution from NV^- increases to 45% (Figure 17c).³² When the non-conductive ND surface is on the alumina spacer layer, the PL modulation persists. These results suggest that the band bending induced by the potential difference across the NDs is the dominant mechanism. The decrease in the applied voltage induces the further band bending of the $E_{NV^{0/-}}$ below the E_F , resulting in an increased probability of the NV centers to be in the negative charge state (Figure 17b).³²

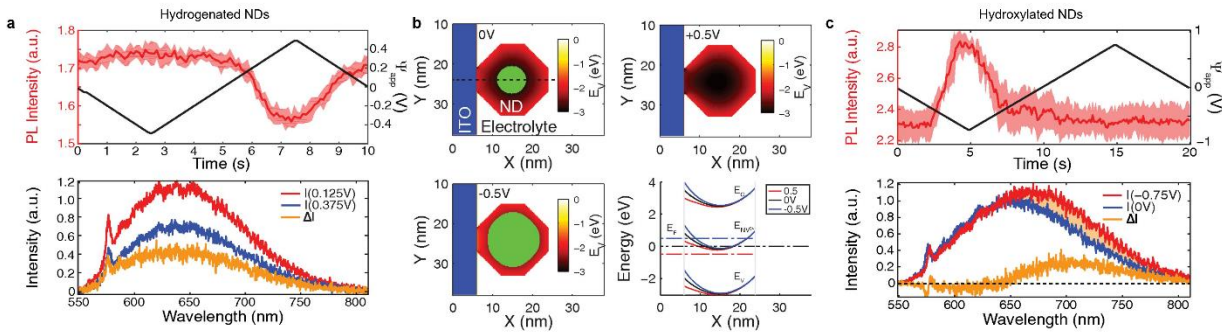


Figure 17 (a) Top: cycle-averaged mean PL response of an isolated single NV center in a hydrogenated ND to applied potential difference. Bottom: PL spectrum of the same NV center obtained by applying a 250 mV amplitude square-wave voltage with a DC bias of 125 and 375 mV, respectively. (b) Numerical simulation result of the energy band diagram of the the cross-section of the ITO/ND/electrolyte system for the three applied potential differences. (c) Top: cycle-averaged mean PL response of an isolated single NV in a hydroxylated ND center to applied potential difference. Bottom: PL spectrum of the same NV center obtained at 0 V and at -0.75 V, respectively. Reproduced from reference 32.

Overall, these findings suggest that there are two different mechanisms by which the applied voltage can modulate the charge state of the NV centers, the surface charge transfer occurring in the hydrogenated NDs, and the band bending occurring in the hydroxylated NDs. Due to the strong

band bending caused by hydrogen, the average energy difference between $E_{NV^{0/-}}$ and E_F in hydrogenated NDs is smaller than the average energy difference between $E_{NV^{+/0}}$ and E_F in hydroxylated NDs. Therefore, a larger voltage difference is required to perturb the NV charge state in hydroxylated NDs compared with hydrogenated NDs.³² Furthermore, it has been reported that the voltage sensitivity of a single hydroxylated ND can be down to 100 mV, and the voltage sensitivity of multiple hydrogenated NDs can be down to 20 mV.³² These results suggest that the NV centers of NDs could enable the detection of membrane potential changes, along with their superior biocompatibility and exceptional photostability.³⁰

The charge state of NV centers also depends on their distance to the surface, the crystallographic orientations on individual surfaces, and the heterogeneity of functional groups. These give rise to the complex energy structure of any single ND and the inhomogeneity between different NDs. Various responses to the same applied potential difference have been observed within a population of NDs having the same surface termination. Therefore, it is difficult to predict the response of a single ND to external electric field. There is still large room for improvement in the synthesis of high-quality engineered NDs with well-controlled shape, NV centers and surface properties.³⁶

5.2 Characterizing the response of nanomaterials upon external voltage modulation

The above introduction on the physical origin, especially the experimental results, of the voltage sensitivity of QDs, NRs and NDs, relies on capacitive devices that apply electric field across these nanomaterials and enable the quantification of their PL responses at single particle level with high throughput. This section describes several devices featuring different designs that have been used to test the voltage sensitivity of nanomaterials and discusses their strengths and weaknesses.

5.2.1 Quantum dots

- Horizontally patterned device

Park and coworkers designed a horizontal electrode array that consists of two forked electrodes interlocking on a glass plate and presenting an interdigitated pattern (Figure 18a).²² QDs and NRs having different composition, size, shape and band structure, were dissolved in toluene and drop-casted onto the device. Applying a voltage difference between the two electrodes created an electric

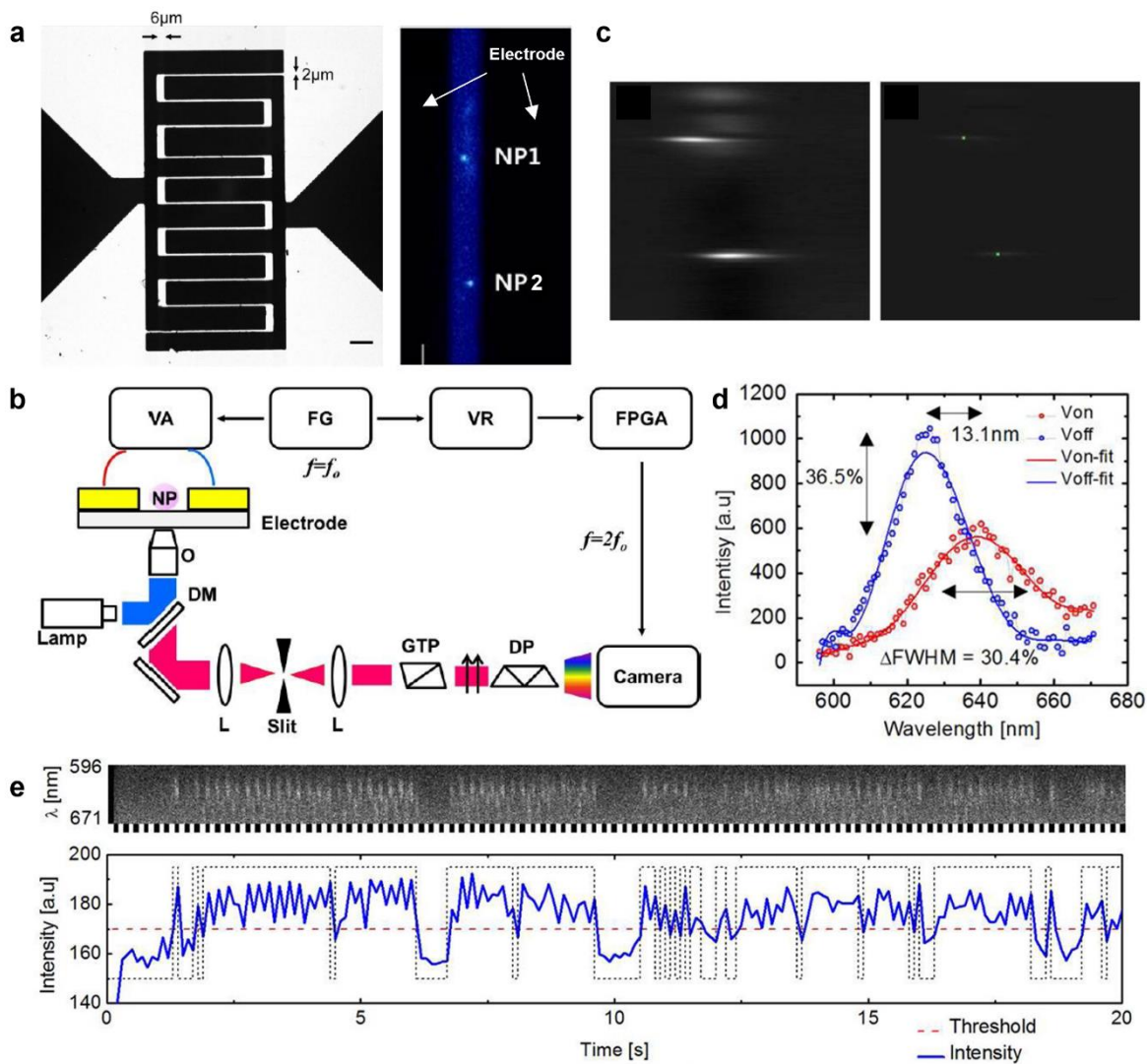


Figure 18 (a) Left: photolithographically patterned interdigitated electrodes. The gap between finger electrodes is $2\ \mu\text{m}$. Right: QDs image (single frame) taken with the slit. (b) Schematics of the setup used to perform single nanoparticle QCSE spectroscopy. (c) Left: average of 200 frames of the image in (a) after background correction. Right: automated spectral peak detection, where green dots represent spectral peak positions of the two particles. (d) Averaged voltage-on frames (red) and voltage-off frames (blue) after filtering for frames in the blinking-on state with corresponding seventh order polynomial fits. (e) Series of 200 successive spectra obtained from QDs at room temperature. Integrated intensity trajectory (over λ for each frame) of the data shown in the upper. The dashed red line is a guide to the eye emphasizing the blinking-on and blinking-off intensity states. Reproduced from reference 22.

field across the nanomaterials that located between them (Figure 18b).²² A Glan-Thompson prism was used to select the NRs that were aligned along the direction of the applied electric field, giving rise to the maximum separation between the charge carriers (Figure 18c).²² Their emission spectra were then dispersed by a dove prism and detected by an electron multiply charge coupled device camera to resolve the changes of peak position and fluorescent intensity, i.e., the magnitude of QCSE (Figure 18d).²² The measurements were conducted at room temperature to mimic the conditions of membrane potential changes occurring in living cells. However, at room temperature, the charge carriers get readily ionized via thermal ejection from the core to the QD surface, resulting in fluorescent intermittency with typical blinking-on and blinking-off noise-like intensity values. Therefore, only frames during blinking-on periods were retained for further analysis using a threshold filter (Figure 18e).²²

Although this horizontally patterned device is able to characterize the fluorescent responses of individual QDs and NRs at high throughput, it presents several issues. First, the electric field is not homogeneous in the area between the two electrodes, which raises the concerns about the reliability of obtained results.¹⁶ Second, there is a dielectric mismatch between the semiconductor nanocrystals (a static dielectric constant ϵ_r close to 10) and air ($\epsilon_r = 1$), and thus most of the applied electric field drops near the electrodes instead of across the particle.^{16, 50, 51} Third, nanomaterials are exposed to the air and thus tend to rapidly photobleach due to oxidation. Finally, the device suffers significantly from catastrophic arc discharge or meltdown events.

- Vertically patterned device

Rowland and coworkers developed a vertically stacked device within a Sawyer-Tower circuit to characterize the fluorescent responses of different types of QDs to electric fields (Figure 19a).²⁰ QDs were coated with hydrophobic ligands and embedded within a poly (methyl methacrylate) (PMMA) thin layer, which mimics their insertion into the plasma membrane bilayer. This reduces the voltage dropping issue arising from the dielectric mismatch between the air and nanocrystals. The PMMA layer was sandwiched between two dielectric layers of SiO₂ to avoid the potential direct contact and charge transfer between the nanocrystals and the ITO and Ti/Au electrodes. This

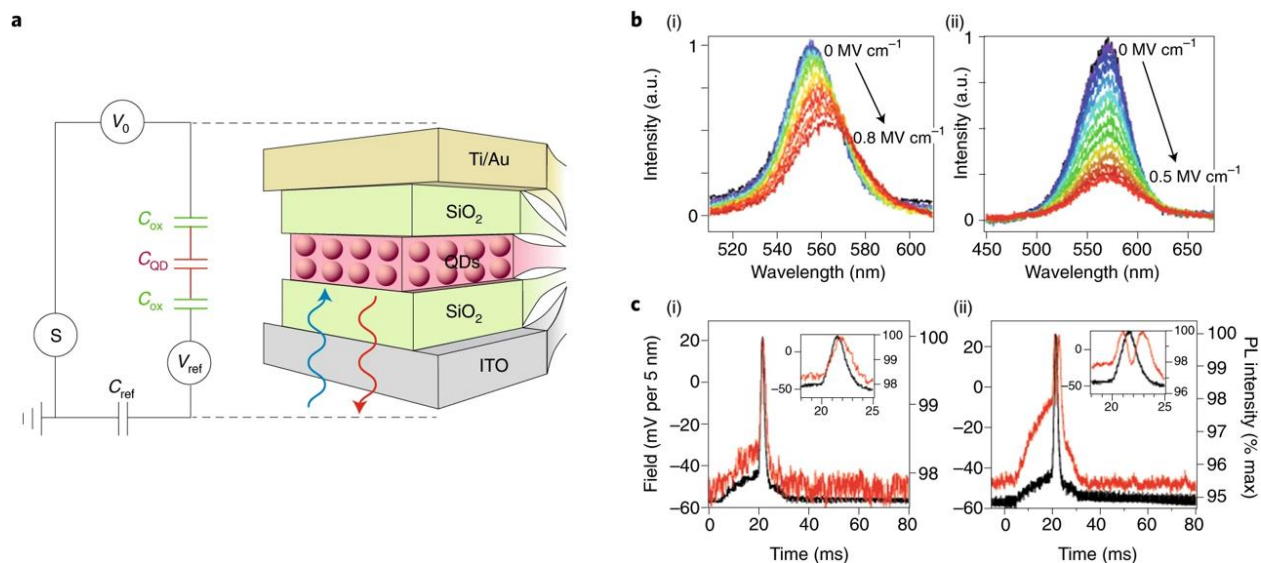


Figure 19 (a) Schematic of the vertically stacked device in a Sawyer-Tower circuit used for measuring QD PL response to an applied electric field. (b) Steady state PL spectra of type I and quasi type II QDs. The increase in electric field decreases the PL intensity and results in a red shift in the maximum emission wavelength, both properties that are consistent with the QCSE. (c) Time-resolved traces of the PL intensity of the QDs (red trace) in response to application of a pulsed electric field with time dependence that mimics the neuronal action potential (black trace). Reproduced from reference 20.

vertically stacked device was able to apply a homogeneous electric field across the QDs within PMMA layer. In addition, the use of the Sawyer-Tower circuit enables the application of electric fields with known magnitude to the QDs, making reliable modulation and measurements (Figure 19b).²⁰ It has been revealed that the PL responses of QD is able to resolve a time-dependent voltage profile that emulates that of an action potential (Figure 19c).²⁰ It has also been demonstrated that the applied electric field not only changes the overlap integral between charge carriers via QCSE, but also increases the ionization probability of the QDs ensembles, resulting in enhanced modulation of their PL intensity.

This vertically stacked device has subsequently been adopted by Kuo and coworkers for the high throughput screening of different types of QDs and NRs (Figure 20a).⁵² They investigated the spectral and emission intensity changes of hundreds of nanocrystals under voltage modulation in one field-of-view using a spectrally-resolved microscope and an automated program for analysis (Figure 20b and c).^{52, 53} It has been demonstrated that the 12 nm long type II NRs exhibit much larger voltage sensitivities, both $\Delta F/F$ and $\Delta\lambda$, compared to the other QDs and NRs studied in their work, including spherical QDs and 40 nm long quasi type I NRs (Figure 20d and e).⁵²

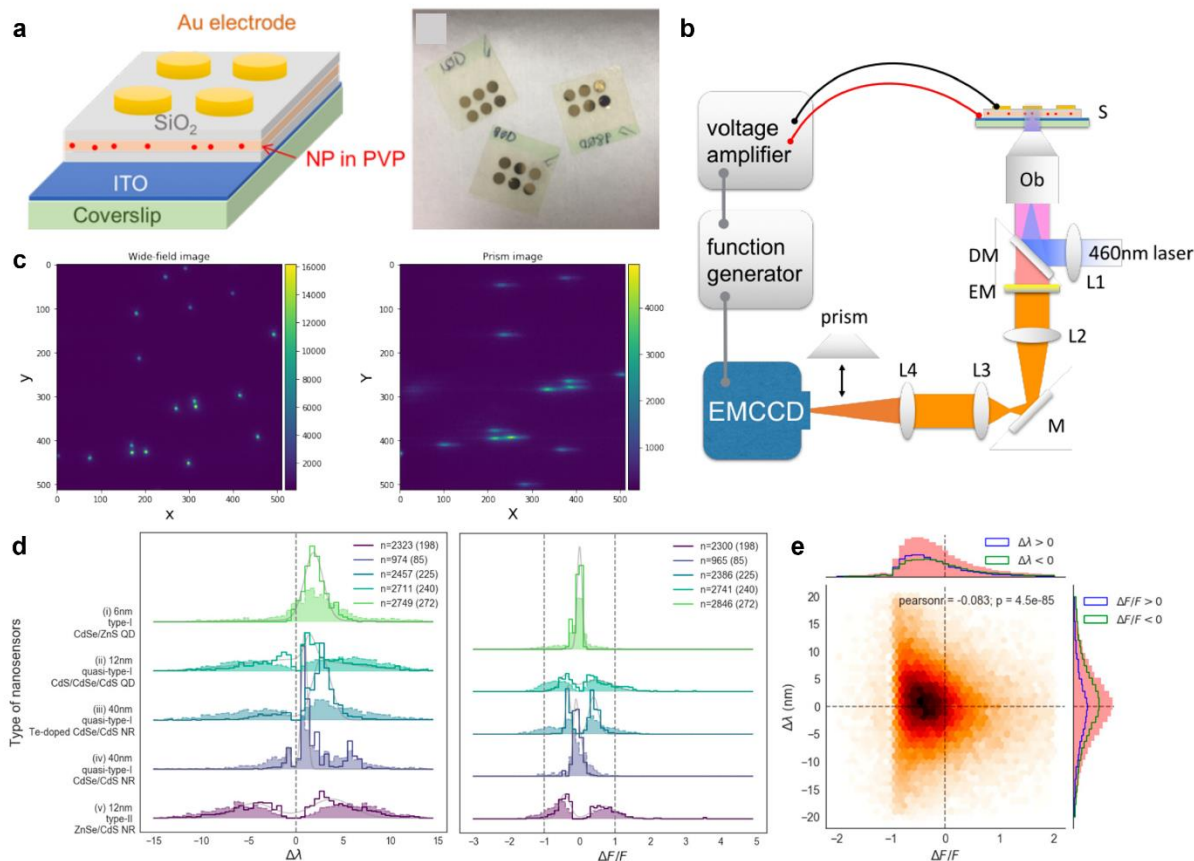


Figure 20 (a) A schematics and a photo of the vertically stacked device. (b) Schematics of the wide-field spectrally resolved microscope. In a QCSE measurement, the prism is inserted to disperse individual point spread functions into spectrally resolved lines. (c) Wide-field image (left) and prism-dispersed image (right) of spin-coated FluoSphere (625/645) (d) Histograms of $\Delta\lambda$ (left) and $\Delta F/F$ extracted from bursts from five types of QDs. (e) 2D histograms of $\Delta F/F$ and $\Delta\lambda$ constructed from individual modulation cycles from 125 type II ZnSe/CdS NRs each contributing ~ 450 modulation cycles on average, including blinking “off” states. The distribution of $\Delta F/F$ and $\Delta\lambda$ are shown on the top and right panel. Reproduced from reference 52.

5.2.2 Nanodiamonds

- Electrochemical cell

Karaveli and coworkers designed an electrochemical cell consisting of an ITO-coated coverslip epoxied with a cylindrical polypropylene tube, which contains 100 μM potassium chloride solution with phosphate buffer (10 mM Na₂PO₄ and 1.8 mM KH₂PO₄, pH = 7.7).^{32, 48} A potentiostat was

used to apply a potential difference between the ITO working electrode and the Ag/AgCl reference electrode immersed in the electrolyte, while a second platinum electrode dipped in the electrolyte solution acts as a reference (Figure 21a).³² This applied potential drops across the electric-double layer formed at the ITO/electrolyte interface, where NDs with different surface termination are located. The device is positioned on an inverted microscope for wide-field or scanning confocal imaging. This method allows the characterization of PL responses of NDs under conditions more closely related to the physiological environments experienced by voltage sensors in living cells. Using this device, it has been demonstrated that the charge state of NV centers in NDs can be controlled by external electric field, and their fluorescence response is sensitive enough to detect 100 mV potential variations (Figure 21b).³² These results show that NDs could be used as direct optical reporters of membrane potential changes.

This device also has several issues. First, this device uses the ion gradient to induce a voltage drop across the electric-double layer at the ITO/electrolyte interface. The electric field experienced by NDs is not homogeneous, which raises the concern about the reliability of obtained results. Second, shorter voltage pulses that are comparable to the time scale of action potential is not achievable due to the large RC time constant (5 - 30 ms) of the large surface area of the electrochemical cell.³² Third, the hydrogenated NDs are hydrophobic and thus they aggregate on the hydrophilic ITO surface, making the investigation of single hydrogenated NDs difficult.³²

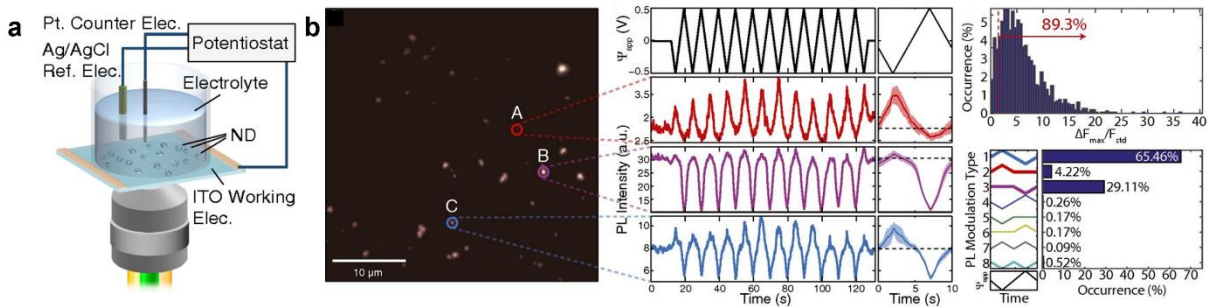


Figure 21 (a) Schematic of the electrochemical cell used to apply voltages while monitoring the ND fluorescence. (b) Left: typical wide-field fluorescence image of hydrogenated NDs on the ITO. Middle: fluorescence time traces of the different clusters of NDs indicated in the left under repetitive triangular voltage sweep Middle: average fluorescence (solid lines) and its SD (shaded region) for the eight voltage cycles. Right: distribution of the maximum PL change normalized to the SD of PL for each measured fluorescent spot. PL modulation is categorized into eight types of voltage responses. Reproduced from reference 32.

5.3 Part II aims and scope

The second part of this thesis aims to investigate the manipulation of NV charge states inside NDs under external electric field using the vertically stacked device, in order to solve the issues encountered by the electrochemical cell. In a broader perspective, the research is aimed at providing a high throughput platform for the screening of NDs with optimal voltage sensitivity. The optical setup, including wide-field spectrally-resolved microscope, and the synchronization between the voltage source and the high-speed camera acquisition system, are so far still under preparation at the time of writing. Therefore, the study focuses on the fabrication of the vertically stacked device with two key objectives:

1. To specify the technical details of fabricating the vertically stacked device for NDs.
2. To achieve monodispersed NDs within the thin polymer layer.
3. To examine the quality of the vertically stacked device, including the surface roughness, thickness, and capacitance.

The following chapters will describe the work on addressing these objectives.

5.4 References

1. Ekinov, A. I.; Efros, A. L.; Shubina, T. V.; Skvortsov, A. P., Quantum-Size Stark Effect in Semiconductor Microcrystals. *Journal of Luminescence* **1990**, *46* (2), 97-100.
2. Norris, D. J., Electronic Structure in Semiconductor Nanocrystals: Optical Experiment. In *Nanocrystal Quantum Dots*, CRC Press: **2017**; pp 63-96.
3. Han, M.; Gao, X.; Su, J. Z.; Nie, S., Quantum-Dot-Tagged Microbeads for Multiplexed Optical Coding of Biomolecules. *Nature Biotechnology* **2001**, *19* (7), 631-635.
4. Weidman, M. C.; Beck, M. E.; Hoffman, R. S.; Prins, F.; Tisdale, W. A., Monodisperse, Air-Stable Pbs Nanocrystals Via Precursor Stoichiometry Control. *ACS Nano* **2014**, *8* (6), 6363-6371.
5. Verma, J.; Islam, S. M.; Verma, A.; Protasenko, V.; Jena, D., 11 - Nitride Leds Based on Quantum Wells and Quantum Dots. In *Nitride Semiconductor Light-Emitting Diodes (Leds) (Second Edition)*, Huang, J.; Kuo, H.-C.; Shen, S.-C., Eds. Woodhead Publishing: **2018**; pp 377-413.
6. Miller, D. A. B.; Chemla, D. S.; Damen, T. C.; Gossard, A. C.; Wiegmann, W.; Wood, T. H.; Burrus, C. A., Band-Edge Electroabsorption in Quantum Well Structures: The Quantum-Confined Stark Effect. *Physical review letters* **1984**, *53* (22), 2173-2176.
7. Efros, A. L.; Rosen, M., Random Telegraph Signal in the Photoluminescence Intensity of a Single Quantum Dot. *Physical Review Letters* **1997**, *78* (6), 1110-1113.
8. Nirmal, M.; Dabbousi, B. O.; Bawendi, M. G.; Macklin, J. J.; Trautman, J. K.; Harris, T. D.; Brus, L. E., Fluorescence Intermittency in Single Cadmium Selenide Nanocrystals. *Nature* **1996**, *383* (6603), 802-804.
9. Krauss, T. D.; Brus, L. E., Electronic Properties of Single Semiconductor Nanocrystals: Optical and Electrostatic Force Microscopy Measurements. *Materials science & engineering. B, Solid-state materials for advanced technology* **2000**, *69*, 289-294.

10. Jankó, B.; Frantsuzov, P.; Kuno, M.; Marcus, R. A., Universal Emission Intermittency in Quantum Dots, Nanorods and Nanowires. *Nature physics* **2008**, *4* (5), 519-522.
11. Efros, A. L., Nanocrystals Almost Always Bright. *Nature materials* **2008**, *7* (8), 612-613.
12. Efros, A. L.; Nesbitt, D. J., Origin and Control of Blinking in Quantum Dots. *Nature Nanotechnology* **2016**, *11* (8), 661-671.
13. Chepic, D. I.; Efros, A. L.; Ekimov, A. I.; Ivanov, M. G.; Kharchenko, V. A.; Kudriavtsev, I. A.; Yazeva, T. V., Auger Ionization of Semiconductor Quantum Drops in a Glass Matrix. *Journal of Luminescence* **1990**, *47* (3), 113-127.
14. Klimov, V. I.; Mikhailovsky, A. A.; McBranch, D. W.; Leatherdale, C. A.; Bawendi, M. G., Quantization of Multiparticle Auger Rates in Semiconductor Quantum Dots. *Science* **2000**, *287* (5455), 1011-1013.
15. Efros, A. L.; Delehanty, J. B.; Huston, A. L.; Medintz, I. L.; Barbic, M.; Harris, T. D., Evaluating the Potential of Using Quantum Dots for Monitoring Electrical Signals in Neurons. *Nature nanotechnology* **2018**, *13* (4), 278-288.
16. Goris, T.; Langley, D. P.; Stoddart, P. R.; del Rosal, B., Nanoscale Optical Voltage Sensing in Biological Systems. *Journal of Luminescence* **2020**, 117719.
17. Zhang, L.; Xiang, W.; Zhang, J., Thick-Shell Core/Shell Quantum Dots. In *Core/Shell Quantum Dots: Synthesis, Properties and Devices*, Tong, X.; M. Wang, Z., Eds. Springer International Publishing: Cham, **2020**; pp 197-218.
18. Ivanov, S. A.; Piryatinski, A.; Nanda, J.; Tretiak, S.; Zavadil, K. R.; Wallace, W. O.; Werder, D.; Klimov, V. I., Type-II Core/Shell CdS/ZnSe Nanocrystals: Synthesis, Electronic Structures, and Spectroscopic Properties. *Journal of the American Chemical Society* **2007**, *129* (38), 11708-11719.
19. Chang, J. H.; Lee, H. J.; Rhee, S.; Hahm, D.; Jeong, B. G.; Nagamine, G.; Padilha, L. A.; Char, K.; Hwang, E.; Bae, W. K., Pushing the Band Gap Envelope of Quasi-Type II

Heterostructured Nanocrystals to Blue: Znse/Znse1-Xtex/Znse Spherical Quantum Wells. *Energy Material Advances* **2021**, 2021, 3245731.

20. Rowland, C. E.; Susumu, K.; Stewart, M. H.; Oh, E.; Mäkinen, A. J.; O'Shaughnessy, T. J.; Kushto, G.; Wolak, M. A.; Erickson, J. S.; L. Efros, A.; Huston, A. L.; Delehanty, J. B., Electric Field Modulation of Semiconductor Quantum Dot Photoluminescence: Insights into the Design of Robust Voltage-Sensitive Cellular Imaging Probes. *Nano Letters* **2015**, 15 (10), 6848-6854.

21. Müller, J.; Lupton, J. M.; Lagoudakis, P. G.; Schindler, F.; Koeppe, R.; Rogach, A. L.; Feldmann, J.; Talapin, D. V.; Weller, H., Wave Function Engineering in Elongated Semiconductor Nanocrystals with Heterogeneous Carrier Confinement. *Nano Letters* **2005**, 5 (10), 2044-2049.

22. Park, K.; Deutsch, Z.; Li, J. J.; Oron, D.; Weiss, S., Single Molecule Quantum-Confined Stark Effect Measurements of Semiconductor Nanoparticles at Room Temperature. *ACS Nano* **2012**, 6 (11), 10013-10023.

23. Kim, S.; Fisher, B.; Eisler, H.-J.; Bawendi, M., Type-Ii Quantum Dots: Cdte/Cdse(Core/Shell) and Cdse/Znte(Core/Shell) Heterostructures. *Journal of the American Chemical Society* **2003**, 125 (38), 11466-11467.

24. Garcia-Etxarri, A.; Yuste, R., Time for Nanoneuro. *Nature Methods* **2021**, 18 (11), 1287-1293.

25. Mochalin, V. N.; Shenderova, O.; Ho, D.; Gogotsi, Y., The Properties and Applications of Nanodiamonds. *Nature Nanotechnology* **2012**, 7 (1), 11-23.

26. Manson, N. B.; Beha, K.; Batalov, A.; Rogers, L. J.; Doherty, M. W.; Bratschitsch, R.; Leitenstorfer, A., Assignment of the Nv0 575 Nm Zero-Phonon Line in Diamond to a 2e-2a2 Transition. **2013**.

27. Ashfold, M. N. R.; Goss, J. P.; Green, B. L.; May, P. W.; Newton, M. E.; Peaker, C. V., Nitrogen in Diamond. *Chemical Reviews* **2020**, 120 (12), 5745-5794.

28. Mzyk, A.; Ong, Y.; Ortiz Moreno, A. R.; Padamati, S. K.; Zhang, Y.; Reyes-San-Martin, C. A.; Schirhagl, R., Diamond Color Centers in Diamonds for Chemical and Biochemical Analysis and Visualization. *Analytical chemistry (Washington)* **2022**, *94* (1), 225-249.
29. Reineck, P.; Francis, A.; Orth, A.; Lau, D. W. M.; Nixon-Luke, R. D. V.; Rastogi, I. D.; Razali, W. A. W.; Cordina, N. M.; Parker, L. M.; Sreenivasan, V. K. A., Brightness and Photostability of Emerging Red and near-Ir Fluorescent Nanomaterials for Bioimaging. *Advanced Optical Materials* **2016**, *4* (10), 1549-1557.
30. Yu, S.-J.; Kang, M.-W.; Chang, H.-C.; Chen, K.-M.; Yu, Y.-C., Bright Fluorescent Nanodiamonds: No Photobleaching and Low Cytotoxicity. *Journal of the American Chemical Society* **2005**, *127* (50), 17604-17605.
31. Doi, Y.; Makino, T.; Kato, H.; Takeuchi, D.; Ogura, M.; Okushi, H.; Morishita, H.; Tashima, T.; Miwa, S.; Yamasaki, S.; Neumann, P.; Wrachtrup, J.; Suzuki, Y.; Mizuochi, N., Deterministic Electrical Charge-State Initialization of Single Nitrogen-Vacancy Center in Diamond. *Physical Review X* **2014**, *4* (1), 011057.
32. Karaveli, S.; Gaathon, O.; Wolcott, A.; Sakakibara, R.; Shemesh, O. A.; Peterka, D. S.; Boyden, E. S.; Owen, J. S.; Yuste, R.; Englund, D., Modulation of Nitrogen Vacancy Charge State and Fluorescence in Nanodiamonds Using Electrochemical Potential. *Proc Natl Acad Sci U S A* **2016**, *113* (15), 3938-43.
33. Hauf, M. V.; Simon, P.; Aslam, N.; Pfender, M.; Neumann, P.; Pezzagna, S.; Meijer, J.; Wrachtrup, J.; Stutzmann, M.; Reinhard, F.; Garrido, J. A., Addressing Single Nitrogen-Vacancy Centers in Diamond with Transparent in-Plane Gate Structures. *Nano Letters* **2014**, *14* (5), 2359-2364.
34. Dolmatov, V. Y.; Veretennikova, M. V.; Marchukov, V. A.; Sushchev, V. G., Currently Available Methods of Industrial Nanodiamond Synthesis. *Physics of the Solid State* **2004**, *46* (4), 611-615.
35. Nunn, N.; Torelli, M.; McGuire, G.; Shenderova, O., Nanodiamond: A High Impact Nanomaterial. *Current Opinion in Solid State and Materials Science* **2017**, *21* (1), 1-9.

36. Chen, L.; Miao, X.; Ma, H.; Guo, L.; Wang, Z.; Yang, Z.; Fang, C.; Jia, X., Synthesis and Characterization of Diamonds with Different Nitrogen Concentrations under High Pressure and High Temperature Conditions. *CrystEngComm* **2018**, *20* (44), 7164-7169.
37. Shenderova, O.; Nunn, N., Chapter 2 - Production and Purification of Nanodiamonds. In *Nanodiamonds*, Arnault, J.-C., Ed. Elsevier: **2017**; pp 25-56.
38. Turner, S., Chapter 3 - Structure, Shape, Defects and Impurities in Nanodiamonds Investigated by HRTEM and STEM-EELS. In *Nanodiamonds*, Arnault, J.-C., Ed. Elsevier: **2017**; pp 57-84.
39. Reineck, P.; Trindade, L. F.; Havlik, J.; Stursa, J.; Heffernan, A.; Elbourne, A.; Orth, A.; Capelli, M.; Cigler, P.; Simpson, D. A.; Gibson, B. C., Not All Fluorescent Nanodiamonds Are Created Equal: A Comparative Study. *Particle & Particle Systems Characterization* **2019**, *36* (3), 1900009.
40. Lühmann, T.; Raatz, N.; John, R.; Lesik, M.; Rödiger, J.; Portail, M.; Wildanger, D.; Kleißler, F.; Nordlund, K.; Zaitsev, A.; Roch, J.-F.; Tallaire, A.; Meijer, J.; Pezzagna, S., Screening and Engineering of Colour Centres in Diamond. *Journal of physics. D, Applied physics* **2018**, *51* (48), 483002.
41. Turcheniuk, K.; Mochalin, V. N., Biomedical Applications of Nanodiamond (Review). *Nanotechnology* **2017**, *28* (25), 252001.
42. Wilson, E. R.; Parker, L. M.; Orth, A.; Nunn, N.; Torelli, M.; Shenderova, O.; Gibson, B. C.; Reineck, P., The Effect of Particle Size on Nanodiamond Fluorescence and Colloidal Properties in Biological Media. *Nanotechnology* **2019**, *30* (38), 385704.
43. Aslam, N.; Waldherr, G.; Neumann, P.; Jelezko, F.; Wrachtrup, J., Photo-Induced Ionization Dynamics of the Nitrogen Vacancy Defect in Diamond Investigated by Single-Shot Charge State Detection. *New J. Phys.* **2013**, *15*.
44. Hauf, M. V.; Grotz, B.; Naydenov, B.; Dankerl, M.; Pezzagna, S.; Meijer, J.; Jelezko, F.; Wrachtrup, J.; Stutzmann, M.; Reinhard, F.; Garrido, J. A., Chemical Control of the Charge State of Nitrogen-Vacancy Centers in Diamond. *Physical Review B* **2011**, *83* (8), 081304.

45. Thalassinos, G.; Stacey, A.; Dontschuk, N.; Murdoch, B. J.; Mayes, E.; Girard, H. A.; Abdullahi, I. M.; Thomsen, L.; Tadich, A.; Arnault, J.-C.; Mochalin, V. N.; Gibson, B. C.; Reineck, P., Fluorescence and Physico-Chemical Properties of Hydrogenated Detonation Nanodiamonds. *C* **2020**, *6* (1).
46. Maier, F.; Riedel, M.; Mantel, B.; Ristein, J.; Ley, L., Origin of Surface Conductivity in Diamond. *Physical review letters* **2000**, *85* (16), 3472-3475.
47. Hauf, M. V.; Others, Chemical Control of the Charge State of Nitrogen-Vacancy Centers in Diamond. *Phys. Rev. B* **2011**, *83*.
48. Karaveli, S.; Gaathon, O.; Wolcott, A.; Sakakibara, R.; Peterka, D.; Owen, J. S.; Yuste, R.; Englund, D. R. In *Electrochemical Potential Control of Charge State and Fluorescence of Nitrogen Vacancy Centers in Nanodiamonds*, CLEO: 2015, San Jose, California, 2015/05/10; Optical Society of America: San Jose, California, **2015**; p FTh3B.6.
49. Karaveli, S.; Gaathon, O.; Wolcott, A.; Sakakibara, R.; Shemesh, O. A.; Peterka, D. S.; Boyden, E. S.; Owen, J. S.; Yuste, R.; Englund, D., Modulation of Nitrogen Vacancy Charge State and Fluorescence in Nanodiamonds Using Electrochemical Potential. *Proceedings of the National Academy of Sciences* **2016**, *113* (15), 3938-3943.
50. Park, K. Imaging Membrane Potential with Semiconductor Nanoparticle. Ph.D., University of California, Los Angeles, Ann Arbor, **2014**.
51. Royo, M.; Climente, J. I.; Movilla, J. L.; Planelles, J., Dielectric Confinement of Excitons in Type-I and Type-II Semiconductor Nanorods. *Journal of Physics: Condensed Matter* **2010**, *23* (1), 015301.
52. Kuo, Y.; Li, J.; Michalet, X.; Chizhik, A.; Meir, N.; Bar-Elli, O.; Chan, E.; Oron, D.; Enderlein, J.; Weiss, S., Characterizing the Quantum-Confined Stark Effect in Semiconductor Quantum Dots and Nanorods for Single-Molecule Electrophysiology. *ACS Photonics* **2018**, *5* (12), 4788-4800.

53. Zhang, Z.; Kenny, S. J.; Hauser, M.; Li, W.; Xu, K., Ultrahigh-Throughput Single-Molecule Spectroscopy and Spectrally Resolved Super-Resolution Microscopy. *Nature Methods* **2015**, *12* (10), 935-938.

CHAPTER 6 METHODS

CONTENTS

6.1	SiO ₂ deposition.....	122
6.2	Nanodiamonds suspension preparation.....	122
6.3	PVP layer deposition.....	122
6.4	Shadow mask and electrode deposition	123
6.5	References	124

This chapter describes the technical details for each step during the fabrication of the vertically stacked device.

6.1 SiO₂ deposition

An ITO-coated coverslip (#1.5, 18 mm × 18 mm, 30 – 60 ohms per square resistivity, from SPI Supplies) was used as the starting substrate. The transparent ITO layer allows for the continuous excitation and the collection of the NV centers fluorescence. A 3 mm wide area on one side of the ITO layer was protected by Kapton tape throughout the whole fabrication process as electrical contact point. Then, a 500 nm thick layer of SiO₂ was deposited using e-beam evaporation (4 kW, 2.3e⁻³ mbar) at a rate of 8.5 nm/min. Argon plasma cleaning of the ITO surface was performed before depositing SiO₂. The resistance of the SiO₂ layer was confirmed to be infinite using a multimeter and the thickness of SiO₂ layer was checked by profilometer.

6.2 Nanodiamonds suspension preparation

HPHT nanodiamonds (120 nm nominal size, from Nabond, China) were irradiated with 2 MeV electrons to a fluence of $1 \times 10^{18} \text{ cm}^{-2}$, annealed in vacuum (800 °C, 2h), oxidized in air (520 °C, 4h). These NDs are estimated to contain ~ 1 ppm of NV centers based on the measurements on bulk diamond samples, which were irradiated and annealed under identical conditions.¹

These NDs were used as an example for the device fabrication. To avoid the aggregation of NDs in the poly (vinylpyrrolidone) (PVP, 40k from Sigma-Aldrich) solution over time, the NDs suspension and PVP solution were prepared separately and mixed just before the deposition of PVP layer. First, PVP (10 wt%) was dissolved in a mixture of 500 μL methanol and H₂O (1:1). Then, NDs (10 mg/mL) were suspended in 100 μL H₂O. Finally, the mixture of methanol and H₂O with a volume of 400 μL (1:1) was prepared.

6.3 PVP layer deposition

A SPIN 150 wafer spinner was used to deposit the PVP layer containing NDs. To make sure that the NDs disperse as single particles within the PVP layer, the suspension of 10 mg/mL NDs in H₂O was bath-sonicated for 10 min. Then, all separated solutions were mixed to result in a PVP concentration of 50 mg/mL and a NDs concentration of 1 mg/mL. The final suspension was also vortexed and bath-sonicated for 10 mins before the spin coating (2000 or 3000 rpm for 120 s, with the acceleration rate of 500 rpm/s). The final suspension (25 μ L – 35 μ L) was dropped from the top of the spinner onto the substrate when the speed was stable. After the PVP deposition, another 500 nm thick layer of SiO₂ was deposited using e-beam evaporation.

6.4 Shadow mask and electrode deposition

A 30 mm \times 30 mm plastic shadow mask was 3D printed with six circle holes (3 mm diameter) in the middle, where the distance between each hole was 2 mm (Figure 22a). The shadow mask was placed onto the substrate near the center area to avoid the edge bead caused by the spin coating of PVP layer, i.e., the flattest area, and thus its location is different from sample to sample. A layer of chromium (5 nm thick for better adhesion) and then platinum (100 nm) were deposited onto the substrate through the shadow mask via vacuum sputtering (Figure 22b). Gold electrode was also

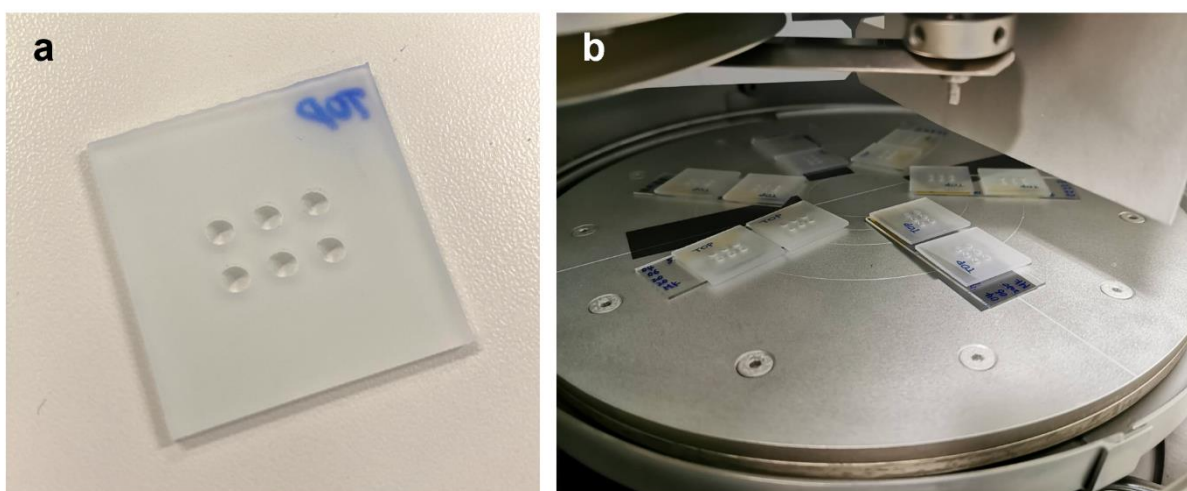


Figure 22 (a) 3D-printed plastic shadow mask for the deposition of Pt/Cr electrode. (b) The positioning of shadow masks and the substrates in the chamber of vacuum sputtering for electrode deposition.

tested but they were not stable and easily peeled off by copper tape. One side of the shadow mask facing the substrate was finely polished to ensure close contact. The Pt and ITO electrodes on two sides of the device provided electrical contact points for the application of an electric field to be experienced by the insulated NDs.

6.5 References

1. Reineck, P.; Abraham, A. N.; Poddar, A.; Shukla, R.; Abe, H.; Ohshima, T.; Gibson, B. C.; Dekiwadia, C.; Conesa, J. J.; Pereiro, E.; Gelmi, A.; Bryant, G., Multimodal Imaging and Soft X-Ray Tomography of Fluorescent Nanodiamonds in Cancer Cells. *Biotechnol J* **2021**, *16* (3), e2000289.

CHAPTER 7 SANDWICH DEVICE CHARACTERIZATION

CONTENTS

7.1	Nanodiamonds shape and spectra	126
7.2	Dispersity of NDs within PVP layer	126
7.3	PVP layer thickness and surface roughness	127
7.4	Sandwich device layer thickness.....	128

This chapter provides the characterization results of the vertically stacked device using TEM, laser scanning confocal microscope, atomic force microscope (AFM), and SEM techniques.

7.1 Nanodiamonds shape and spectra

Under TEM, significant variations in the shape and size of HPHT NDs were observed as expected (Figure 23a). The facets of these NDs were irregular with sharp edges. The spectra of several NDs particles within the PVP layer was collected and resolved via laser scanning confocal microscope (FV3000, Olympus), showing the featured ZPL of NV^0 at 575 nm and NV^- at 637 nm.

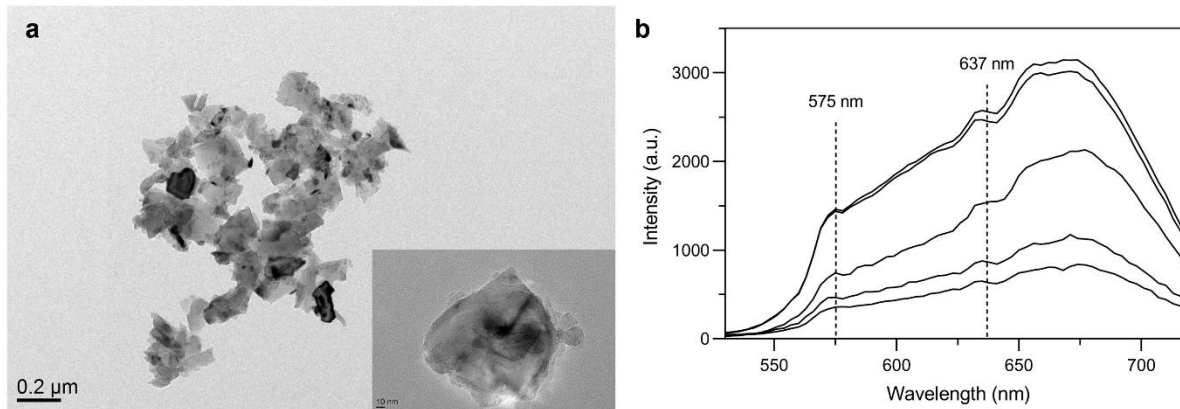


Figure 23 (a) TEM image of fluorescent NDs with nominal diameter of 120 nm. Scale bar, 0.2 μm. Inset shows an individual ND having irregular shape and sharp edges. (b) The fluorescence spectra of several NDs particles measured by scanning confocal microscopy, showing evident zero phonon lines at 575 and 637 nm.

7.2 Dispersity of NDs within PVP layer

The dispersity of NDs within the PVP thin layer was examined under laser scanning confocal microscopy (Figure 24). Facilitated by the sonication, NDs were able to disperse as single particles and homogeneously distributed throughout the PVP layer. In contrast, without sonication, NDs were aggregated into large clusters. Their aggregation would affect the interpretation of the voltage sensitivity test results, where the charge transfer and unexpected interaction between NDs could

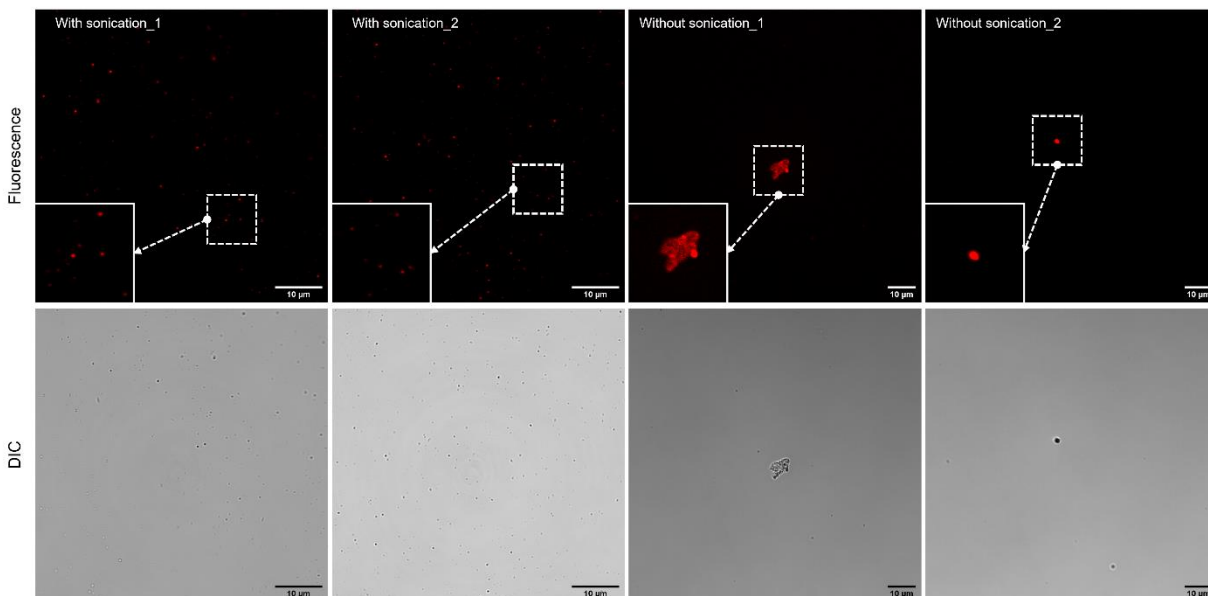


Figure 24 Representative fluorescence and DIC images of NDs within the PVP layer obtained by laser scanning confocal microscope. Left two columns show the monodispersed NDs within the PVP layer, where the NDs in H₂O suspension and the final mixture solution were sonicated for 10 mins before spin coating. Right two columns show the aggregated NDs within the PVP layer, where the NDs in H₂O suspension and the final mixture solution were not sonicated before spin coating. Scale bar, 10 μm. Magnified insets (left bottom on fluorescence images) show the dispersity details of NDs in the areas outlined by white dash lines.

occur. The overlap of fluorescent signals between NDs would prevent the accurate detection of the charge state conversion. Our findings suggest that sonication can effectively distribute NDs evenly within the PVP solution, making the investigation of voltage-dependent charge state manipulation of single NDs possible.

7.3 PVP layer thickness and surface roughness

The thickness of a spin coated film is proportional to the inverse of the spin speed squared. Two spin speeds of 2000 rpm and 3000 rpm were tested for the spin coating of PVP thin layer on the coverslips (Figure 25a). The PVP deposited coverslips were cut by ceramic knife and the thickness of the PVP layer was measured from the cross section using SEM (Figure 25b). The PVP thickness sits within the range of 350 to 400 nm using 2000 rpm and the spin speed of 3000 rpm results in the PVP thickness close to 200 nm (Figure 25c). To fully embed the NDs with nominal diameter of 120 nm within the PVP layer, the spin speed of 2000 rpm was chosen for the PVP deposition.

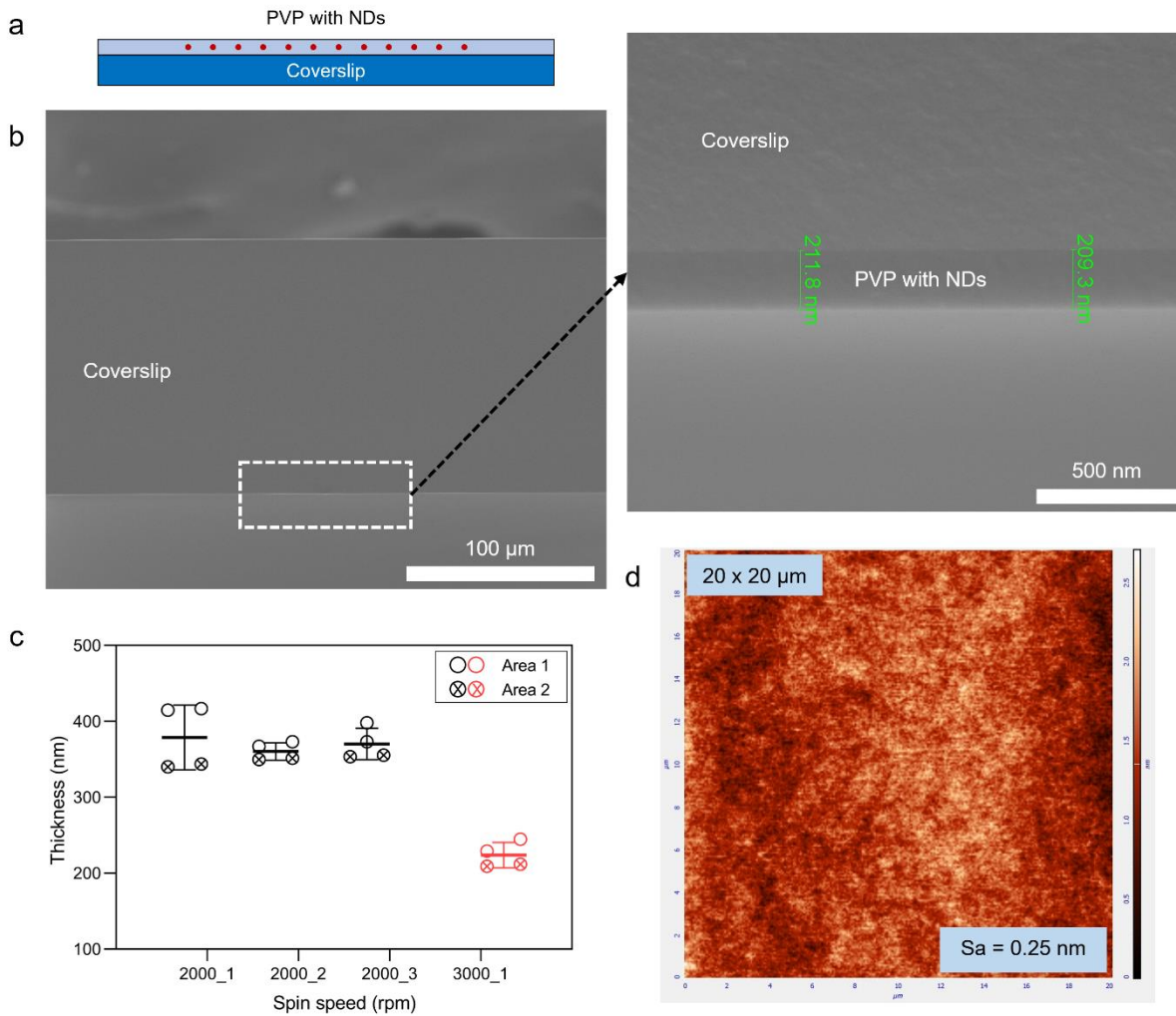


Figure 25 (a) Schematic of NDs embeded within the PVP layer. (b) SEM images of the cross-section of PVP layers showing the thickness. (c) Spin speed dependent PVP layer thickness. For each sample, the thickness was measured at two different position in two distinct areas. (d) Surface roughness of spin-coated PVP layer. The size of field-of-view is $20 \times 20 \mu\text{m}$.

The surface roughness of PVP layer was in high quality with an average S_a of 0.25 nm, which was examined using AFM.

7.4 Sandwich device layer thickness

The schematic structures of the vertically stacked device from the side and top views are shown in Figure 26a and b. The final assembled device was fragile and was fixed onto and supported by

a glass slide. The integrity of different layers in the final assembled device was examined by SEM imaging of the cross section (Figure 26d and e), which demonstrated correct layer assignments and expected thickness of each layer. The capacitance between each Pt electrode and the ITO layer was measured to be 1 nF and should be tested before the voltage sensitivity test to ensure the functionality of the device.

The design of six separated Pt electrical contact points rather than deposit the Pt electrode over the entire device is to avoid the leakage of electrical current and the burning of the device during the high-voltage measurement. Depositing six Pt electrodes increases the imaging area. In addition, occasional glitches in the conductivity through the device would occur during the fabrication. This multi-electrode design ensured that the measurements could be repeated multiple times in the same device. When all six Pt electrodes are functioning properly, they are redundant. However, if one or

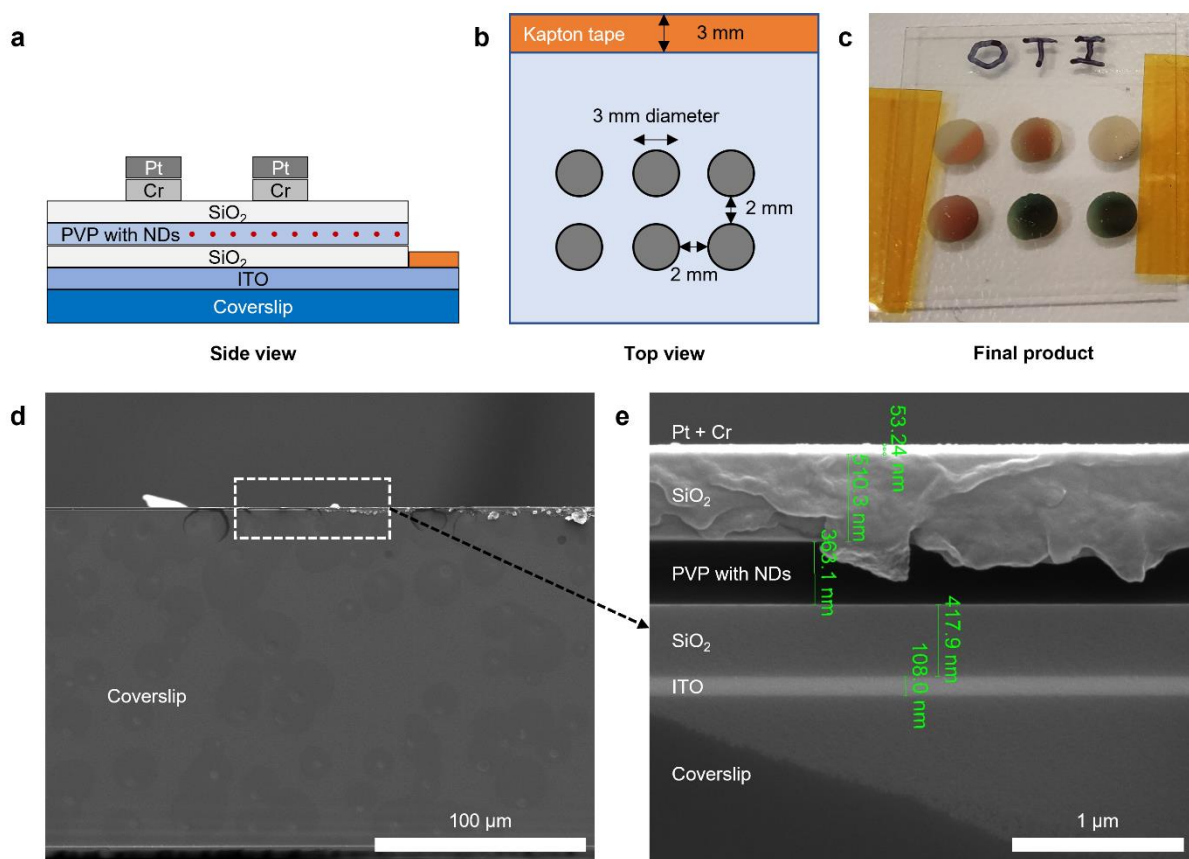


Figure 26 (a) Schematic structure of the vertically stacked device from side view. (b) Schematic structure of the vertically stacked device from top view. (c) A photo of the vertically stacked device. (d) SEM images of the cross-section of the device. Scale bar, 100 μm . (e) Zoom-in view of the cross-section of the device showing the thickness of different layers. Scale bar, 1 μm .

a few of the Pt electrodes fails, the others are spare to save the time for the fabrication of new batches. The electrical contact to voltage source can be easily achieved by several methods, such as silver paste, carbon tape, copper tape, and metal spring contact.

Overall, these characterization results of the vertically stacked device demonstrate its utility for the investigation of the charge state conversion of NV centers in single ND particles.

CHAPTER 8 CONCLUSIONS

It is of utmost importance to understand the voltage sensing mechanisms of nanomaterials so that they can be reliably deployed for the optical imaging of membrane potential changes. The fabrication of the vertically stacked device is the core and the first step for investigating the charge state conversion of NV centers under external electric field. This structure eliminates the charge state manipulation of NV centers as a result of charging or the introduction of exogenous electrons, where any fluorescent change observed is directly attributable to the applied electric field. Here, the use of sonication effectively distributes the NDs homogeneously as single particles throughout the PVP layer, which is beneficial for the study of the voltage sensitivity of single NDs and can be employed to other types of nanomaterials. Currently, there is growing interest in developing other semiconductor nanocrystals and other color centers (e.g., SiC and SiV) in diamond that present potential voltage sensitivity.¹ For example, the SiC center has shown a stronger response to electric fields than those of NV center.² The SiV center has been found in NDs as small as 1.6 nm in diameter, and they are likely to present charge state conversion and fluorescent changes under voltage modulations.³ In addition, most of the commercially available QDs have type I band structure, e.g., CdSe/ZnS (core/shell), which is designed to achieve optimal quantum yield and photostability for long-term fluorescent bioimaging, as has been demonstrated for intracellular delivery in Part I. Type II QDs and NRs that possess higher voltage sensitivity require de novo synthesis, which will be the focus of future work. With the optical set up and synchronization system to be established shortly, a high throughput screening platform will be available for the thorough study of the voltage sensitivity of various nanomaterials.

Besides the voltage sensing mechanism, there are the critical issues that need to be solved before the implementation of NDs for in vivo real-time membrane potential sensing. A tight control over the shape, size, and crystallographic orientation of HPHT NDs continuous to be an area of focus. Unlike the narrow size distribution of QDs, the large variations in the morphology of HPHT NDs highly impede their microelectrophoretic-mediated intracellular delivery, where tip blockage might occur. In addition, the effective delivery and proper surface functionalization for their stable insertion into the plasma membrane bilayer have not been explored. However, initial successes,

such as the intracellular delivery of QDs via microelectrophoresis technique demonstrated in the first part of this thesis, and the recently reported peptide-like coating of NRs for their membrane insertion,^{4, 5} have shown exciting promise on this front.

8.1 References

1. Karaveli, S.; Gaathon, O.; Wolcott, A.; Sakakibara, R.; Shemesh, O. A.; Peterka, D. S.; Boyden, E. S.; Owen, J. S.; Yuste, R.; Englund, D., Modulation of Nitrogen Vacancy Charge State and Fluorescence in Nanodiamonds Using Electrochemical Potential. *Proceedings of the National Academy of Sciences* **2016**, *113* (15), 3938-3943.
2. Falk, A. L.; Klimov, P. V.; Buckley, B. B.; Ivády, V.; Abrikosov, I. A.; Calusine, G.; Koehl, W. F.; Gali, A.; Awschalom, D. D., Electrically and Mechanically Tunable Electron Spins in Silicon Carbide Color Centers. *Phys Rev Lett* **2014**, *112* (18), 187601.
3. Vlasov, I. I.; Shiryaev, A. A.; Rendler, T.; Steinert, S.; Lee, S.-Y.; Antonov, D.; Vörös, M.; Jelezko, F.; Fisenko, A. V.; Semjonova, L. F.; Biskupek, J.; Kaiser, U.; Lebedev, O. I.; Sildos, I.; Hemmer, P. R.; Konov, V. I.; Gali, A.; Wrachtrup, J., Molecular-Sized Fluorescent Nanodiamonds. *Nature Nanotechnology* **2014**, *9* (1), 54-58.
4. Park, K.; Kuo, Y.; Shvadchak, V.; Ingargiola, A.; Dai, X.; Hsiung, L.; Kim, W.; Zhou, Z. H.; Zou, P.; Levine Alex, J.; Li, J.; Weiss, S., Membrane Insertion of—and Membrane Potential Sensing by—Semiconductor Voltage Nanosensors: Feasibility Demonstration. *Science Advances* **2018**, *4* (1), e1601453.
5. Park, J.; Kuo, Y.; Li, J.; Huang, Y.-L.; Miller, E. W.; Weiss, S., Improved Surface Functionalization and Characterization of Membrane-Targeted Semiconductor Voltage Nanosensors. *The Journal of Physical Chemistry Letters* **2019**, *10* (14), 3906-3913.